Quantitative MRI for measuring cardiac-induced brain tissue pulsations in humans

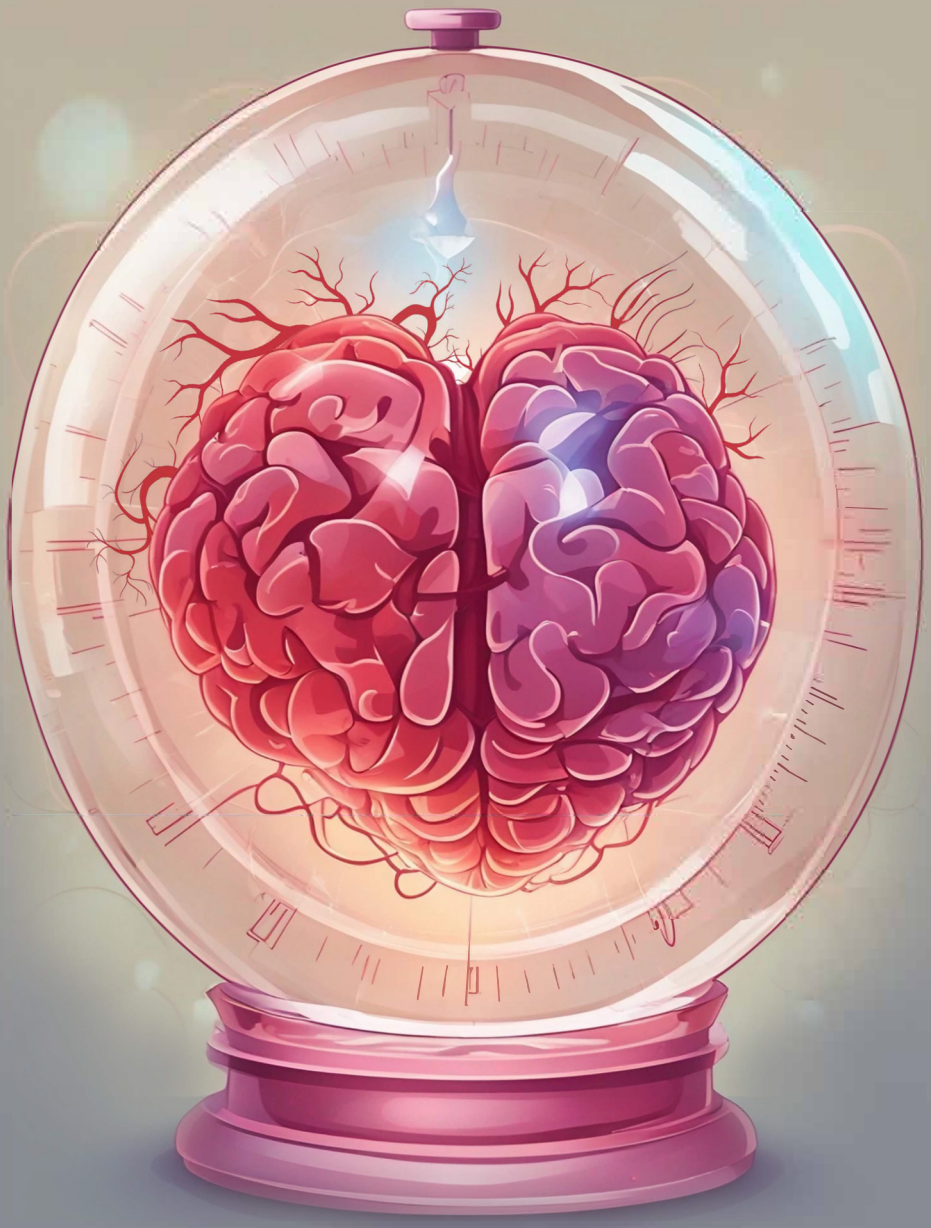

Ayodeji L. Adams

Quantitative MRI for measuring cardiac-induced brain tissue pulsations in humans

Ayodeji L. Adams

Quantitative MRI for measuring cardiac-induced brain tissue pulsations in humans.
PhD Thesis, Utrecht University, The Netherlands

Cover & chapter art	Ayodeji Adams & Stability AI LTD - www.clipdrop.co
Layout design	Ayodeji Adams
Printing	ProefschriftMaken - www.proefschriftmaken.nl

ISBN 978-94-6469-579-3

The cover and chapter artwork used in this book were generated using Stable Diffusion XL 1.0, a text-to-image generation model developed by Stability AI and released under the CreativeML OpenRAIL++±M License. The images were generated using prompts engineered by Ayodeji Adams.

Quantitative MRI for measuring cardiac-induced brain tissue pulsations in humans

Kwantitatieve MRI voor het meten van door het hart geïnduceerde pulsaties van hersenweefsel bij mensen
(met een samenvatting in het Nederlands)

Proefschrift

ter verkrijging van de graad van doctor aan de
Universiteit Utrecht
op gezag van de
rector magnificus, prof.dr. H.R.B.M. Kummeling,
ingevolge het besluit van het college voor promoties
in het openbaar te verdedigen op

dinsdag 17 oktober 2023 des ochtends te 10.15 uur

door

Ayodeji Leigh Adams

geboren op 25 januari 1990
te Liverpool, Verenigd Koninkrijk

Promotoren:
Prof. dr. P.R. Luijten
Prof. dr. M.A. Viergever

Copromotor:
Dr. J.J.M. Zwanenburg

Beoordelingscommissie:
Prof. dr. G.J. Biessels (voorzitter)
Prof. dr. R.M. Dijkhuizen
Prof. dr. J. Hendrikse
Prof. dr. ir. D.W.J. Klomp
Prof. dr. ir. M.J.P. van Osch

The research leading to these results has received funding from the European Research Council under the European Union's Seventh Framework Programme (FP7/2007-2013) / ERC grant agreement n°337333, and under the H2020 program / ERC Grant Agreement n° 841865

Never give up on a dream just because of the time it will take to accomplish it.
The time will pass anyway.

— Earl Nightingale

Table of Contents

List of abbreviations **8**

Chapter 1 **9**

Introduction

Chapter 2 (Part I) **19**

Quantifying cardiac-induced brain tissue expansion using DENSE

Chapter 2 (Part II) **41**

Verification of DENSE brain tissue measurements using PC-MRI

Chapter 2 (Part III) **47**

A theoretical analysis of noise propagation in the quantification of brain tissue expansion

Chapter 3 **51**

Validating faster DENSE measurements of cardiac-induced brain tissue expansion as a potential tool for investigating cerebral microvascular pulsations

Chapter 4 (Part I) **75**

Measurements of cardiac-induced brain tissue pulsations in patients with white matter lesions

Chapter 4 (Part II) **95**

Investigating the high strain energies present in measurements of cardiac-induced brain tissue pulsations in patients with white matter lesions

Chapter 5 **107**

Quantitative comparison between aMRI and DENSE for the assessment of brain tissue motion

Chapter 6 **133**

Summary and General Discussion

Appendices **149**

Nederlandse Samenvatting (Dutch Summary)
Acknowledgements (Dankwoord)
Biography
List of publications and presentations

List of abbreviations

aMRI - Amplified magnetic resonance imaging
AP - Anterior to posterior
bSSFP - Balanced steady state free precession
CoV - Coefficient of variation
CSF - Cerebrospinal fluid
cSVD - Cerebral small vessel disease
Damp-MRI - DENSE amplified magnetic resonance imaging
Dani-aMRI - DENSE animated amplified magnetic resonance imaging
Dani-MRI - DENSE animated magnetic resonance imaging
DENSE - Displacement encoding with stimulated echoes
EA - Estimated amplification (slope of regression)
ERB - Ethical Review Board
FH - Feet to head
FLAIR - Fluid attenuated inversion recovery
GM - Grey matter
GTD - Ground truth displacements
ICVC - Intracranial volume change
IQR - Inter quartile range
NAWM - Normal appearing white matter
PCMRI - Phase-contrast magnetic resonance imaging
POx - Pulse oximeter
PVS - Perivascular space
PWE - Pulse wave encephalopathy
RL - Right to left
ROI - Region of interest
SENSE - Sensitivity encoding
SNR - Signal to noise ratio
T1w - T1-weighted
VCG - Vectorcardiogram
WB - Whole brain
WET - Water suppression enhanced through T1 effects
WM - White matter
WMH - White matter hyper-intensity
WMH_R - White matter hyper-intensity risk

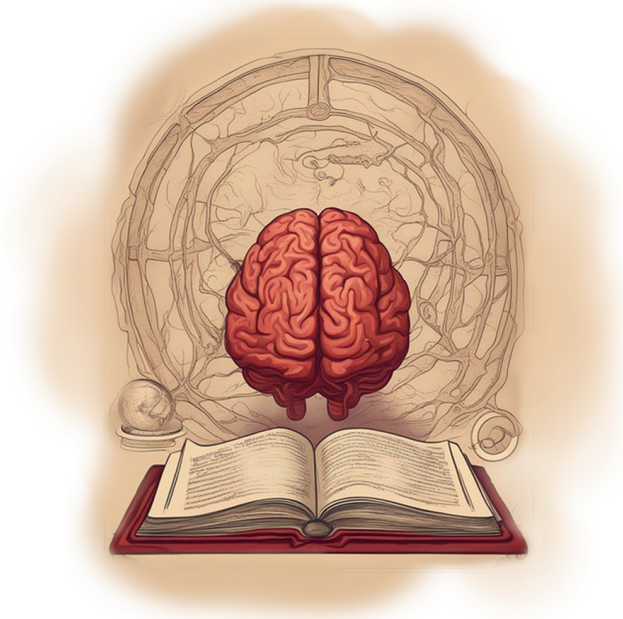

Chapter 1

Introduction

Cerebral microvasculature

The cerebral microvasculature refers to an intricate network comprised of the smallest vessels in the vascular tree which transport blood to and from the brain parenchyma. As one travels deeper into the arterial tree, oxygen-rich blood is transmitted through progressively smaller arteries which gradually branch to form arterioles and then capillaries. The capillaries act as a selective barrier to protect the brain from foreign substances, and assist in the regulation of blood pressure, angiogenesis and inflammation[1]. It is at the capillary level that oxygen, nutrients and waste products are exchanged between the blood and brain tissue. Subsequently, deoxygenated blood is transferred to venules and then veins leading back to the heart. Figure 1 shows the centripetal organization of the cerebral microvasculature, including the larger feeding and draining pial vessels that reside on the surface of the brain. Surrounding the arterioles, capillaries and venules is the perivascular space, a fluid filled region that is composed of interstitial and cerebrospinal fluids. It assists in the clearance of metabolic waste products, forming a part of the brain's glymphatic system, and supporting the health and proper functioning of the brain[2,3].

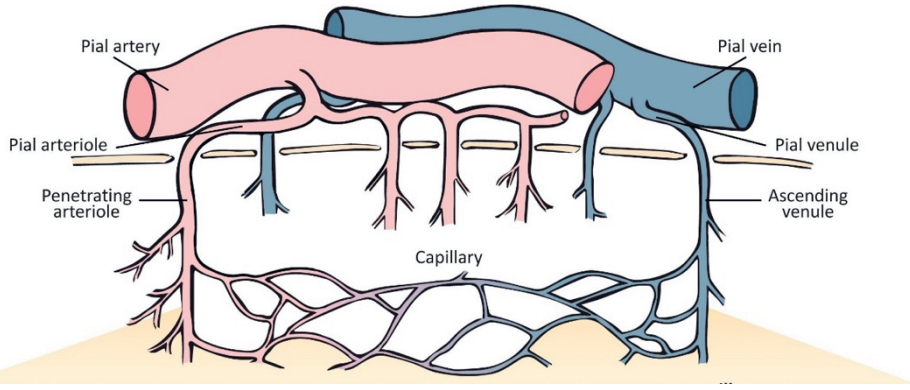

Figure 1. Components of the cerebral microvasculature, adapted from Uemura et al. (4)

Cerebral small vessel disease

Dysfunction of the cerebral microvasculature can lead to cerebral Small Vessel Disease (cSVD), an umbrella term that encompasses several pathological conditions that reflect damage to the cerebral small vessels, including white matter lesions (areas of white matter damage which manifest as hyperintense regions on some MR sequences), lacunar infracts (localized regions of dead tissue formed from the blockage of small arteries), cerebral microbleeds (hemorrhages of the fragile small vessels in the brain) and enlarged perivascular spaces[4]. These neuroimaging markers of the disease are often correlated and are thought to share some common mechanisms such as endothelial dysfunction, compromised blood-brain barrier and inflammation. Symptoms of cSVD varies depending on the severity of the disease, but can include gait instability, cognitive decline, dementia, and mood disorders. Diagnosis of the cSVD is typically performed using magnetic resonance imaging (MRI).

Hypertension and age are risk-factors for developing cSVD. Hypertension is on the rise world-wide[5]. Additionally, the general improvements in nutrition, health care and living standards are predicted to increase life expectancy, thereby driving a rise in the ageing population. Thus, there is urgent need to further our understanding of the cerebral microvasculature and its disturbances, as this is essential for improving the diagnosis and treatment of cSVD. MR-based imaging tools may yet fulfill that need by leveraging its capacity to indirectly assess microvascular function in health, and the deterioration with disease, before patient end-of-life.

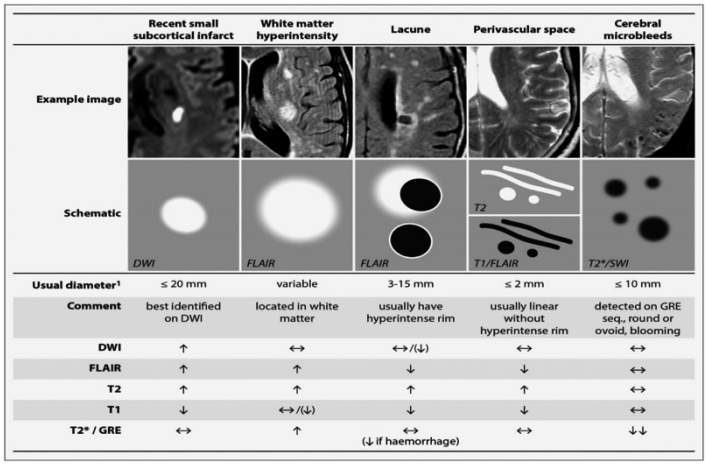

	Recent small subcortical infarct	White matter hyperintensity	Lacune	Perivascular space	Cerebral microbleeds
Usual diameter[1]	≤ 20 mm	variable	3-15 mm	≤ 2 mm	≤ 10 mm
Comment	best identified on DWI	located in white matter	usually have hyperintense rim	usually linear without hyperintense rim	detected on GRE seq., round or ovoid, blooming
DWI	↑	↔	↔/(↓)	↔	↔
FLAIR	↑	↑	↓	↓	↔
T2	↑	↑	↑	↑	↔
T1	↓	↔/(↓)	↓	↓	↔
T2* / GRE	↔	↑	↔ (↓ if haemorrhage)	↔	↓↓

Figure 2. Neuroimaging markers of cSVD on MRI, reproduced from Shi & Wardlaw[6].

A primary challenge in the study of cSVD is that the size of the small vessels which cause the disease have diameters ranging between 5 and approx. 500 μm[7]. This hinders us from directly viewing in-vivo the anatomical damage associated with the compromised microvasculature. Consequently, indirect methods are needed to visualize in-vivo the damage to the small vessels leading to cSVD. The current imaging markers of cSVD (Figure 2), are a clear illustration of this indirect approach, as these lesions reflect tissue damage secondary to the vascular dysfunction. As these lesions mostly reflect end-stage, irreversible tissue damage, it has only limited value for studying the disease processes underlying cSVD, which limits the understanding of how this disease leads to brain tissue damage and, subsequently, cognitive impairment. In this thesis, I want to move towards (still indirect) markers that more closely reflect the physiology of the small vessels instead. Brain tissue pulsations could provide such a marker (as will be explained below).

Brain tissue pulsations as window into microvascular function

The pulsation of the brain that occurs with each cardiac cycle is a well-established phenomenon[8–11]. The small vessels pulsate under normal physiological function to deliver

fresh blood from the heart and remove waste products. The highly vascularized anatomy of brain tissue allows the microvasculature to have a direct influence on the brain tissue volume as the heart pumps blood through the vascular system. A minute increase in blood volume occurs within the microvasculature with every heartbeat, which induces a cyclic, local displacement to the surrounding brain tissue[12]. Some of the pulse energy is dissipated into the local tissue as the underlying microvasculature expands and contracts to accommodate changes in the vascular blood volume. The cyclic expansion and contraction of the tissue is a measure of its pulsation, quantified by the volume change or equivalently volumetric strain.

Insights into the microvasculature function in health - or its dysfunction with natural aging or disease - might be obtained from measurements of brain tissue motion. This is valuable, because one of the proposed mechanisms by which cSVD develops is pulse wave encephalopathy (PWE), where it is suggested that damage to the microvasculature occurs from an increase in pulse energy delivered from upstream, stiffer vessels[13]. In a healthy state, the larger compliant vessels assist in the damping of the cardiac pulse energy, reducing its intensity before it arrives at the microvasculature. The intensity must be reduced since high mechanical stress can damage endothelial function and disrupt the blood-brain barrier[14]. Therefore, examining how the surrounding tissue bed pulsates as a response to the cardiac cycle might provide further insights into the development of cSVD.

Measuring brain tissue pulsations with DENSE MRI

Displacement Encoding with Stimulated Echoes (DENSE) is an MRI technique that has been proposed as a promising method for measuring brain tissue displacement, thanks to the technique's ability to track small displacements at high spatial and temporal resolution[15]. As such, it has the potential to provide important information about the physiology of the brain and the vascular function of the microvasculature.

DENSE was initially developed for cardiac applications[16]. The method utilizes a specific sequence of RF pulses to create a displacement encoded image, which can be used to quantify tissue displacement and strain. DENSE evolved from the Tagging/SPAMM (Spatial Modulation of Magnetization) MRI techniques which are well-established for assessing cardiac tissue displacements and function[17]. SPAMM MRI utilizes spatially selective RF pulses to create a unique tag pattern in the tissue, which can be tracked over time as the tissue moves. DENSE extends this method by using a stimulated echo to encode the tissue displacement into the phase of the MR signal. This allows for a higher signal-to-noise ratio and higher spatial resolution than traditional SPAMM MRI techniques.

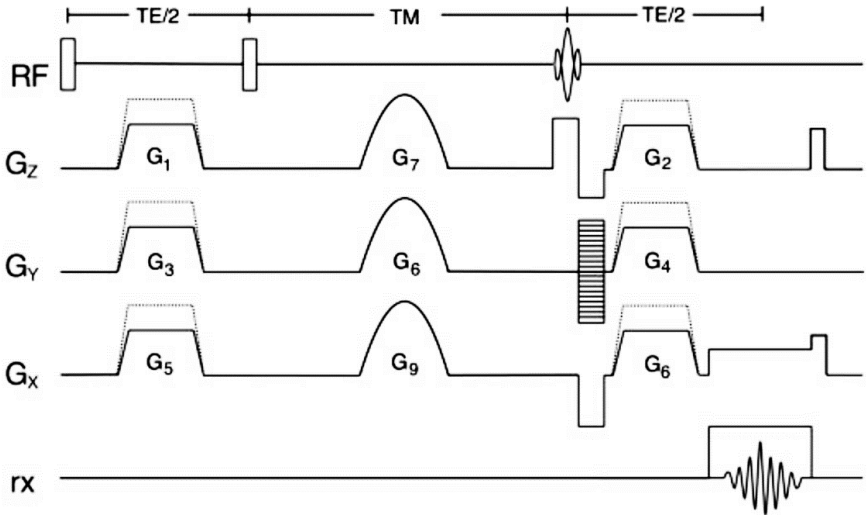

Figure 3. The basic DENSE pulse sequence, reproduced from Aletras et al.[16]

The basic pulse sequence of DENSE (Figure 3) begins with using two RF pulses which sandwich a gradient lobe. The first RF pulse provides an initial excitation which tips the magnetization into the transverse plane, the gradient pulse induces a linear phase roll in the direction of the gradient, which results in a sinusoidal longitudinal magnetization after the second RF pulse. In this way the initial state of the tissue is captured.

After a period described as the mixing time (TM), a third RF pulse returns the magnetization to the transverse plane, after which application of a second gradient lobe (equal in magnitude to the first) produces a 'stimulated' echo. Tissue motion that occurred during the TM can be regarded as a (phase) shift in the sinusoidal longitudinal magnetization. This phase shift propagates into the phase of the stimulated echo. Consequently, tissue which has not moved between application of the gradients possesses zero additional phase, whilst tissue which has moved has accrued phase that is directly related to the tissue displacement, which is sustained in the MR signal as the image is recorded. A displacement encoded image can thus then be acquired by applying a readout gradient and detecting the MR signal.

Quantifying brain tissue pulsations

If accurate measurements of brain tissue motion can be obtained, volumetric strain (reflecting microvascular swelling) can in principle be obtained from these measurements using strain analysis. Strain is the term used to describe an overall change in the shape or size of a material when a point on the material is displaced. For a material of initial length L1, which after displacement has a new length L2, the relationship between displacement and strain is expressed through the formula: strain = $\frac{L2-L1}{L1}$, which is unitless. Volumetric strain is the extension of this concept to three-dimensional space. This corresponds spatially to regions undergoing expansion or compression. Summing the gradients of the orthogonal components

of the displacement field U yields the volumetric strain as expressed in the following equation.

$$\text{Volumetric Strain} \equiv \frac{\Delta V}{V} = \frac{\partial u_1}{\partial x_1} + \frac{\partial u_2}{\partial x_2} + \frac{\partial u_3}{\partial x_3} \qquad \text{Eqn 1.}$$

Eqn 1. Volumetric strain, defined as the ratio of change in volume to original volume, is the sum of the partial derivatives of a displacement field along orthogonal directions.

The quantification of volumetric strain in brain tissue can be achieved through displacement field measurements obtained from DENSE. To obtain reliable brain tissue pulsation measurements one must however employ a technique that can resolve displacements with high spatial and temporal resolution, and sensitivity. The latter is of particular importance because of the small displacements that are associated with brain tissue pulsations, which are in the order of micrometers. The resulting displacement data can then be used to calculate volumetric strain, thereby providing a metric for brain tissue pulsations (i.e., the amount of expansion and compression undergone by the tissue).

Challenges and opportunities for obtaining volumetric strain from DENSE measurements

DENSE has several strengths supporting its suitability for measuring brain tissue motion in the context of better understanding cSVD. First, as an MR-based technique, DENSE does not cause significant subject discomfort, making it a useful tool for investigating the disease in patients before their end of life. Secondly, DENSE has been extensively employed in the quantification of cardiac motion and thus can be considered a mature technology/methodology. The studies by Soellinger et al.[15] have substantiated the applicability of DENSE for determining cardiac-induced brain tissue pulsations. In principle, DENSE should allow for the acquisition of pulsatile data covering the whole brain tissue and entire cardiac cycle at sufficient spatial and temporal resolutions, which would enable comprehensive analyses of brain tissue motion. Furthermore, the mathematical relation of measured tissue displacements to volumetric strain, a metric of the relative change in volume, has been established, thus providing an indirect marker of microvascular functionality.

However, despite the capability of DENSE to obtain displacement fields reflecting brain tissue pulsations, volumetric strain measurements covering the whole brain and the whole cardiac cycle have not yet been performed, but it appears feasible with current technology. One remaining concern pertaining to the use of DENSE for the assessment of brain tissue motion is the inherent limited Signal-to-Noise Ratio (SNR) of the method. This could lead to difficulty in accurately measuring small tissue displacements, a problem further compounded as other physiological or subject motion must be excluded. The SNR challenges of DENSE might also explain the scarcity of the literature available investigating its potential

use as a research tool for cSVD, and the push by Soellinger et. al to develop towards higher field strength systems (she did her study at 3T), which have intrinsically higher SNR. Further research is necessary to explore its capabilities at even higher field strengths (7T MRI), which might enable us to fully harness the potential of volumetric strain as a marker for microvascular dysfunction in cSVD.

Aim and Outline

The aim of the work is the development, implementation, and evaluation of DENSE/volumetric strain as an MRI tool to investigate brain tissue microvasculature performance.

To this end, the following studies were performed:

Chapter 2 describes the implementation and preliminary validation of the DENSE technique at 3T and 7T magnetic field strengths. This study begins where the work of Soellinger et al. ends i.e., with the procurement of prospectively-triggered measurements of cardiac-induced brain tissue displacements fields covering the whole brain and cardiac cycle at 3T. As an extension of their work, volumetric strain measurements were further computed to infer microvascular function in healthy subjects, both at 3T and 7T. It establishes the feasibility and utility of DENSE to measure tissue pulsations at high field strengths, and further affirms the need for high SNR to faithfully represent the brain tissue volumetric strain energy.

Chapter 3 describes an improvement and further validation of DENSE as MR tool for investigating the microvasculature. Retrospectively-gated DENSE was developed as an approach to obtain two times faster acquisition and further improvement of the signal-to-noise ratio. The repeatability of the measurements was also assessed in separate sessions. Due to the fixed intracranial vault volume, the Monro-Kellie doctrine dictates that an increase in brain tissue volume must be compensated by a similar decrease in the intracranial fluid compartment volumes. Therefore, additional validation was performed by taking paired measurements of CSF flow at the C2-C3 cervical level.

The work performed in **Chapters 2** and **3** provided a framework and experience of systematically obtaining and quantifying brain tissue pulsations in healthy subjects. The next major step towards an MR tool that is useful for clinical research is to determine whether the method can ascertain differences in the diseased case. The work detailed in **Chapter 4** is an exploration of volumetric strain in a patient cohort with carotid artery stenosis and neuroimaging markers associated with cSVD. The patients' brain tissue volumetric strain measurements were compared to healthy controls. This exploratory study provides preliminary evidence that volumetric strain may be a useful tool in identifying and monitoring microvascular dysfunction in cSVD patients.

Despite the utility of DENSE for assessing microvascular pulsations, the implementation, testing and validation of a new technique is an extensive clinical endeavour, and the challenges thereof may limit clinical utility. As such, **Chapter 5** describes the exploration of Amplified Magnetic Resonance Imaging (aMRI) to investigate the microvasculature, and a comparison to the measurements provided with DENSE. aMRI is post-processing technique to amplify small motion present in videos, and thus can be performed on cine-images obtained from a clinically available MR sequence. Although the aMRI method is not yet clinically available, it is primarily a software-based tool that can be applied on standard clinical MRI acquisitions, which makes it potentially simpler to gain use in clinical research then DENSE. The resulting amplified displacements were quantified using image registration and compared to DENSE tissue measurements.

Finally, a general discussion is provided in **Chapter 6,** where the performance of DENSE to investigate the microvasculature is discussed. Although DENSE is a mature technology for cardiac applications, its use for the exploration of brain tissue microvasculature is still in its infancy. Thus, **Chapter 6** is concluded with a future outlook on the potential of this technique as an indirect window to the small vessels, through which a better understanding of microvascular function in health, age and disease may be obtained.

References

1. Dalkara T. Cerebral Microcirculation: An Introduction. In: *PanVascular Medicine*. Springer Berlin Heidelberg; 2015:655-680. doi:10.1007/978-3-642-37078-6_29
2. Cipolla MJ. The Cerebral Circulation. *Colloquium Series on Integrated Systems Physiology: From Molecule to Function*. 2009;1(1):1-59. doi:10.4199/C00005ED1V01Y200912ISP002
3. Iliff JJ, Thrane AS, Nedergaard M. The Glymphatic System and Brain Interstitial Fluid Homeostasis. In: *Primer on Cerebrovascular Diseases*. Second Edi. Elsevier; 2017:17-25. doi:10.1016/B978-0-12-803058-5.00003-5
4. Wardlaw JM, Smith C, Dichgans M. Small vessel disease: mechanisms and clinical implications. *Lancet Neurol*. 2019;18(7):684-696. doi:10.1016/S1474-4422(19)30079-1
5. Zhou B, Carrillo-Larco RM, Danaei G, et al. Worldwide trends in hypertension prevalence and progress in treatment and control from 1990 to 2019: a pooled analysis of 1201 population-representative studies with 104 million participants. *The Lancet*. 2021;398(10304):957-980. doi:10.1016/S0140-6736(21)01330-1
6. Shi Y, Wardlaw JM. Update on cerebral small vessel disease: a dynamic whole-brain disease. *Bmj*. 2016;1(3):83-92. doi:10.1136/svn-2016-000035
7. Chojdak-Łukasiewicz J, Dziadkowiak E, Zimny A, Paradowski B. Cerebral small vessel disease: A review. *Advances in Clinical and Experimental Medicine*. 2021;30(3):349-356. doi:10.17219/ACEM/131216
8. Enzmann DR, Pelc NJ. Brain motion: measurement with phase-contrast MR imaging. *Radiology*. 1992;185(3):653-660. doi:10.1148/radiology.185.3.1438741
9. Greitz D, Wirestam R, Franck A, Nordell B, Thomsen C, Stahlberg F. Pulsatile brain movement and associated hydrodynamics studied by magnetic resonance phase imaging. *Neuroradiology*. 1992;34(5):370-380. doi:10.1007/BF00596493
10. Poncelet BP, Wedeen VJ, Weisskoff RM, Cohen MS. Brain parenchyma motion: measurement with cine echo-planar MR imaging. *Radiology*. 1992;185(3):645-651. doi:10.1148/radiology.185.3.1438740
11. Maier S, Hardy C, Jolesz F. Brain and cerebrospinal fluid motion: real-time quantification with M-mode MR imaging. *Radiology*. 1994;193:477-483. doi:10.1148/radiology.193.2.7972766
12. Causemann M, Vinje V, Rognes ME. Human intracranial pulsatility during the cardiac cycle: a computational modelling framework. *Fluids Barriers CNS*. 2022;19(1). doi:10.1186/s12987-022-00376-2
13. Bateman GA. Pulse wave encephalopathy: A spectrum hypothesis incorporating Alzheimer's disease, vascular dementia and normal pressure hydrocephalus. *Med Hypotheses*. 2004;62(2):182-187. doi:10.1016/S0306-9877(03)00330-X
14. Thorin-Trescases N, De Montgolfier O, Pinçon A, et al. Impact of pulse pressure on cerebrovascular events leading to age-related cognitive decline. *Am J Physiol Heart Circ Physiol*. 2018;314:1214-1224. doi:10.1152/ajpheart.00637.2017.-Aging
15. Soellinger M, Rutz AK, Kozerke S, Boesiger P. 3D cine displacement-encoded MRI of pulsatile brain motion. *Magn Reson Med*. 2009;61(1):153-162. doi:10.1002/mrm.21802
16. Aletras AH, Ding S, Balaban RS, Wen H. DENSE: Displacement Encoding with Stimulated Echoes in Cardiac Functional MRI. *Journal of Magnetic Resonance*. 1999;137(1):247-252. doi:10.1006/jmre.1998.1676
17. Ibrahim ESH. Myocardial tagging by Cardiovascular Magnetic Resonance: evolution of techniques--pulse sequences, analysis algorithms, and applications. *Journal of Cardiovascular Magnetic Resonance*. 2011;13(1):36. doi:10.1186/1532-429X-13-36

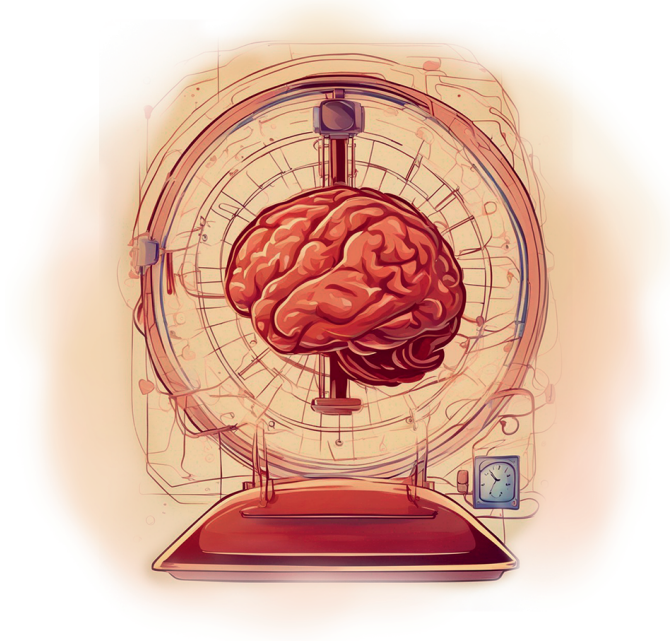

Chapter 2 (Part I)

Quantifying cardiac-induced brain tissue expansion using DENSE

This chapter is based on the research article published as: Adams, A. L., Kuijf, H. J., Viergever, M. A., Luijten, P. R., & Zwanenburg, J. J. M. (*2019*). *Quantifying cardiac-induced brain tissue expansion using DENSE*. NMR Biomed, *32*, e4050.

Abstract

Background

Brain tissue undergoes viscoelastic deformation and volumetric strain as it expands over the cardiac cycle due to blood volume changes within the underlying microvasculature. Volumetric strain measurements may therefore provide insights to small vessel function and tissue viscoelastic properties. Displacement Encoding via Stimulated Echoes (DENSE) is an MRI technique that can quantify the submillimetre displacements associated with brain tissue motion. Despite previous studies reporting brain tissue displacements using DENSE and other MRI techniques, a complete picture of brain tissue volumetric strain over the cardiac cycle has not yet been assessed.

Method

To address this need we implemented a 3D cine-DENSE at 7T and 3T to investigate the feasibility of measuring cardiac-induced volumetric strain as a marker for small vessel blood volume changes. Volumetric strain over the entire cardiac cycle was computed for the whole brain and for grey and white matter tissue separately in six healthy human subjects. Signal-to-noise (SNR) measurements were used to determine the voxel-wise volumetric strain noise.

Results

Mean peak whole brain volumetric strain at 7T was (mean±SD) $(4.5\pm1.0)*10^{-4}$ (corresponding to a volume expansion of 0.48±0.1 ml), which is in agreement with literature values of cerebrospinal fluid that is displaced into the spinal canal to maintain a stable intracranial pressure. The peak volumetric strain ratio of grey to white matter was 4.4±2.8, reflecting blood volume and tissue stiffness differences between these tissue types. The mean peak volumetric strain of grey and white matter tissue was found to be significantly different ($p<0.001$). The mean SNR at 7T and 3T of the DENSE measurements was 22.0±7.3 and 7.0±2.8 respectively, which currently limits a voxel-wise strain analysis at both field strengths.

Conclusion

We demonstrated that tissue specific quantification of volumetric strain is feasible with DENSE. This metric holds potential for studying blood volume pulsations in the ageing brain in healthy and diseased states.

1. Introduction

The brain is mechanically coupled to the heart, which results in pulsatile viscoelastic deformation and volumetric strain of the brain tissue over the cardiac cycle. In a healthy brain, the small vessels embedded within the brain tissue temporarily swell to accommodate the increased intracranial blood volume during systole, thereby causing brain expansion. These cardiac-induced changes in brain tissue volume (i.e. volumetric strain) should therefore reflect transient changes in the blood volume of the small vessels (small arteries/veins, arterioles/venules and capillaries), as well as the material properties of the tissue surrounding the small vessels. Non-invasive assessments of brain tissue motion may thus provide valuable information on small vessel function or allow the derivation of the viscoelastic properties of brain tissue[1]. Brain tissue and vessel stiffness naturally change with age[2,3], which suggests that brain tissue motion particularly holds potential as a means to study the small vessels and/or the viscoelastic properties of the brain as a function of age. Conceivably, it may permit the study of the brain in the transition from healthy to diseased states, such as that which occurs in the development of cerebral small vessel disease (cSVD) where damage to the small vessels causes damage to the tissue. Unlike the larger arteries of the brain or the macroscopic tissue damage that arises from cSVD, the small vessels themselves are difficult to study in vivo with current neuroimaging techniques. Brain tissue motion may provide a valuable biomarker for the disease with the potential to provide an indirect window to the small vessels that are involved in cSVD, and to the microscopic tissue changes subsequent to cSVD as reflected in tissue stiffness.

The overall phenomenon of brain tissue motion is subtle, involving submillimetre displacements[4] and very small amounts of flow changes in the microvasculature[5]. General improvements in available hardware, software and imaging techniques since the early exploration of brain tissue motion using MRI[6–9] has allowed renewed interest in the phenomenon of brain tissue motion in healthy subjects as well as patients[10,11]. Displacement Encoding via Stimulated Echoes (DENSE), a non-invasive MRI technique, was shown to be a feasible method for capturing the displacement vector fields that characterise brain tissue pulsatility[4,12,13], thereby allowing the derivation of brain tissue volumetric strain. However, despite the important potential of brain tissue volumetric strain in evaluating small vessel function, a complete picture of its variation over the cardiac cycle has not yet been assessed. Previous investigations of brain tissue motion did not assess brain tissue volumetric strain[4], or reported it only in relatively small regions of interest (ROI) within at most a few slices[14,15], or measured only 2D strain[13]. These measurements (even those done at 3T) also likely suffered considerably from noise since utilising DENSE to encode brain tissue motion results in an inherent 50% signal loss due to the use of a single stimulated echo in the acquisition window[16]. Additionally, the derivation of volumetric strain requires the computation of spatial derivatives, which amplifies the noise present in the displacement maps. Therefore, the relationship between the signal-to-noise ratio (SNR) of DENSE measurements and the

calculated brain tissue volumetric strain needs to be assessed in order to identify the uncertainty in the computed volumetric strain maps.

In this study, we implemented a high-resolution 3D cine-DENSE at 7T, and also at 3T for reference. The goal was threefold. Firstly, to obtain (in healthy subjects) whole brain volumetric strain measurements covering the entire cardiac cycle, which we propose as an important metric reflecting small vessel blood volume pulsations. Secondly, to demonstrate the potential of DENSE in practice by assessing the physiological pulsatile differences between grey and white matter tissue. The obtained volumetric strain values in this study were evaluated against literature values of cerebrospinal fluid (CSF) stroke volumes and against literature values of the relative blood volume difference between grey and white matter. Thirdly, to investigate the SNR performance of DENSE when applied to the measurement of cardiac-induced whole brain tissue motion. Specifically, the gain in SNR at 7T compared with 3T was determined, from which a voxel-wise uncertainty in the computed volumetric strain map was calculated.

2. Materials and Methods

DENSE Implementation:
A cardiac gated cine-DENSE protocol comparable to that described by Soellinger et al.[4] was implemented in the MR scanner software to measure displacements in the Right-to-Left (RL), Anterior-to-Posterior (AP), and Feet-to-Head (FH) directions (see Figure 1 for the sequence schematic). In our study, the signal from fat tissue was suppressed through the use of a low bandwidth (500 Hz) for the two 90° RF pulses to avoid SENSE artefacts from high fat signal close to the receiver elements of the head coil. To suppress the effect of possible eddy currents, all spoiler gradients were inverted in strength relative to the motion encoding gradient. The residual longitudinal magnetisation at the end of the last excitation in the cardiac cycle was suppressed through the use of water suppression enhanced through T1 effects (WET) pulses[17] using the following four flip angles: 156°, 71.14°, 109.15°, and 90°. (This suppression was initially implemented to prevent potential higher order stimulated echoes from multiple successive motion encodings. However, it was later determined that the suppression is not necessary in practice for this application.)

The excitation flip angles were varied over time as described by Fischer et al.[18] To calculate the flip angles, a T1 value of 1100 ms was used at 7T, and 800 ms at 3T. Preliminary results showed signal instability near the end of the cardiac cycle, so extra TRs were included in the calculation to shift this instability outside of the desired range. We empirically determined that four extra TRs were sufficient for this purpose and consequently used flip angle sweeps with a maximum flip angle of 24.2°. The minimum angle (starting flip angle) depends on the number of cardiac phases which differed between volunteers based on their heart rates. Table 1 contains further protocol parameters.

Parameter	3T DENSE	7T DENSE	7T T1-weighted TFE
D_{enc} (mm) (FH/AP/RL)	0.175 / 0.0875 / 0.0875	0.175 / 0.0875 / 0.0875	--
Resolution (mm)	2.2 isotropic	2.2 isotropic	1.0 isotropic
FOV (mm) (FHxAPxRL)	250 x 250 x 190	250 x 250 x 190	300 x 250 x 190
TR (ms) (FH/AP/RL)	36.8 / 38.3 / 38.3	36.4 / 37.3 / 37.3	4.2
TE (ms)	10.2[a]	8.0	2.0
EPI Phase Encoding BW (Hz/pixel)	92.0	102.6	--
EPI factor	15	15	--
TFE factor	2	2	600
Readout BW (Hz/pixel)	2038.1	2796.0	505.1
Inversion delay (ms)	--	--	1280
Gradient strength (mT/m)	22.5	30	40
Gradient slew rate (T/m/s)	150	150	150
SENSE (AP x RL)	1.9 x 2	2 x 2.5	2 x 2.5
Flip angle (deg)	Variable	Variable[b]	7
T1 (ms)	800	1100	--
Triggering	ECG	ECG/POx(n=1)[c]	--
Coverage of cardiac cycle	11-20 cardiac phases	12-20 cardiac phases[d]	--
Scan duration	3 x 5.5 mins	3 x 4.5 mins[e]	2 mins

Table 1. Imaging parameters used in the study.

[a] A slightly longer TE was used at 3T because of a different gradient performance at that MR system.

[b] The flip angles of the excitation RF pulse were increased over the cardiac cycle, using the field strength dependent T1[18].

[c] POx: a pulse oximeter unit was used because of artefacts in the VCG signal in one subject at 7T.

[d] The number of cardiac phases depended on the heart rate, and covered approximately 110% of the cardiac cycle.

[e] The reported scan duration was for a heart rate of 60 bpm.

Pilot data on human volunteers were used to compare the DENSE implementation with the vendor provided phase contrast velocity mapping, as described in reference[4], to validate the correctness of the motion encoding directions (including signs) and sensitivities for both the sequence implementation and processing software (see Chapter 2 (part II) for further details).

Measurements:

Tissue Motion

The Ethical Review Board (ERB) of the University Medical Center Utrecht, approved the use of healthy volunteers for MRI protocol development. Eight healthy subjects (age 24 ± 5 years, 5 females) were included, after obtaining written informed consent, in accordance with the ERB approval. All subjects were scanned on both a 7T and a 3T scanner (Philips Healthcare, Best, The Netherlands) using a 32-channel head coil at 7T (Nova Medical, Wilmington, Massachusetts) and a 16-channel head coil at 3T (Philips Healthcare), within a 2-hour period per subject. Additionally, a slightly higher gradient strength of 30 mT/m was used at 7T compared to 3T (22.5 mT/m). Cardiac-triggered DENSE was used to acquire

whole brain volume displacement fields using a displacement sensitivity of 0.35 mm/π in the feet-head direction (direction with largest motion[4]) and 0.175 mm/π for the right-left and anterior-posterior directions. Seeking a parameter similar to V_{enc} which is used in phase-contrast MRI, we designed D_{enc} to be the maximum displacement value in units of meters which produces a phase wrap in the final displacement map. Each encoding direction was acquired in two dynamics with opposing encoding gradients for phase error correction, yielding D_{enc} = 0.175 mm in the feet-head direction and D_{enc}= 0.0875 mm for the other two directions.

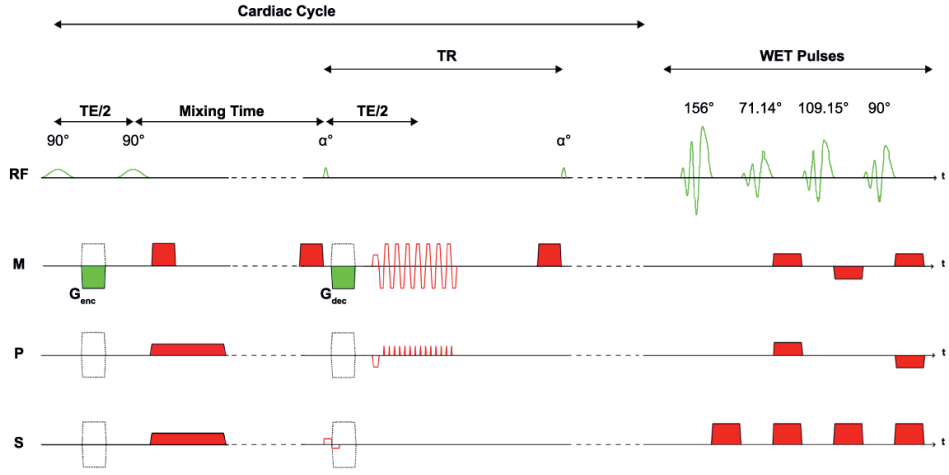

Figure 1. DENSE pulse sequence implemented in this study. The encoding gradients (G_{enc}) and decoding gradients (G_{dec}) were sequentially placed on each axis to encode motion along the right-left, anterior-posterior, and feet-head directions, and were inverted in strength during acquisition of the second dynamic for phase subtraction (solid green areas and related dashed gradients). The spoiler gradients (red gradient areas) performed during the mixing time on the axis hosting the encoding gradient were implemented with the same gradient moment as G_{enc} but with reversed strength, to avoid potential eddy current effects. T1- and B1- insensitive suppression of any residual signal at the end of the cardiac cycle was achieved through the use of the WET RF pulses and dephasing gradients (red areas). It is meant to remove remaining tagged longitudinal magnetisation prior to the next motion encoding block.

Each DENSE acquisition at both 7T and 3T was triggered prospectively using a vectorcardiogram (VCG), which was performed every other heart cycle to allow magnetisation recovery after the WET saturation pulses. A pulse oximeter (POx) was also connected as a backup triggering device in case the VCG triggering failed owing to magneto-hemodynamic effects, which were more severe at 7T.

The number of acquired cardiac phases was adjusted between subjects to cover 110% of the average heart cycle, depending on the individual heart rate. Arrhythmia rejection was used to minimise incorrect triggering from the VCG signal distortions and heart rate variability.

The physiology traces from the VCG and pulse oximeter devices were stored as text files by the scanner, and were saved after the exam for further analysis.

SNR

For SNR analysis, noise images were acquired for the whole volume by repeating an entire Right-Left DENSE acquisition without RFs and gradients present. Additionally, a T1-weighted 3D FFE scan was performed at 7T to enable registration of the DENSE datasets and segmentation of white and grey matter tissues.

Analysis:

Tissue Motion

The VCG and POx traces contained the trigger moments as recognised by the scanner software. In the case of severe magneto-hemodynamic artefacts, triggering could be inconsistent, varying between triggers at the VCG R-wave, and triggers at the slope of the artefact. All traces were visually analysed by comparing the trigger moments of the VCG relative to those of the POx. In case of consistent triggering upon detection of the QRS complex, the VCG trigger was consistently before the POx trigger by about 0.2 to 0.3 seconds. Subjects with inconsistent triggering were excluded from the strain analysis.

Analysis of the acquired datasets was performed offline with custom MATLAB (The MathWorks, Inc., Natick, MA, USA) software. Complex image pairs were generated from the phase images of the two dynamics with opposing gradients and the corresponding mean magnitude image. Through complex division, which yields phase subtraction, the motion-sensitive phase information was obtained, with simultaneous cancellation of background phase errors (including any phase offsets induced from magnetic susceptibility changes which may occur due to the magneto-hemodynamic effect or due to fluctuations in the relative oxyhaemoglobin and deoxyhaemoglobin contents of the tissue). All phase images were unwrapped over time. Displacement was subsequently calculated from the unwrapped phase images using Eq. [2] (see Chapter 2 (part III)). Residual offsets in the displacement maps were corrected by subtracting the first acquired frame of the cardiac cycle from all other acquired frames.

All DENSE magnitude images for each subject were registered with a rigid transformation using Elastix[19] to the subject's respective T1-weighted image space. The resulting transformation from the registration step was then applied to the corresponding displacement maps, yielding interpolated images having 1mm isotropic voxel size.

A whole brain tissue mask free of skull or fat tissue was obtained for each subject from their respective T1-weighted image as follows. First, the Computational Anatomy Toolbox (Jena University Hospital, Departments of Psychiatry and Neurology) for SPM12 (Wellcome Trust Centre for Neuroimaging, University College London) was used to segment the T1-weighted image into CSF, grey and white matter probability maps. However, the DENSE images

exhibited EPI distortions relative to the true anatomy reflected in the T1-weighted images. Therefore as a second step, the T1-weighted images were registered non-rigidly to the transformed DENSE magnitude images, and the resulting transformation from this registration step was then applied to the segmented probability masks. Finally, the grey and white matter 3D probability maps were summed to create a whole brain tissue mask, after which voxels in the summed tissue map with a probability less than 0.95 were removed from the mask.

Since a region with artefacts or CSF in any of the displacement maps could compromise the analysis of tissue volumetric strain, the 3D whole brain tissue mask was further modified to prevent these areas from being used in the analysis. Voxels with a non-zero value in the CSF probability map were removed from the mask, thereby limiting potential partial volume effects. Artefacts were assumed to result in a non-zero net displacement over the cardiac cycle. These areas were therefore estimated and removed from the whole brain tissue mask as follows. Two difference maps were generated for all encoding directions by subtracting displacements at the beginning and end of the cardiac cycle (D_{net}) and by subtracting displacements from the first two acquired phases of the cardiac cycle ($D_{\Delta 1}$). For each encoding direction, the voxels in D_{net} whose absolute displacement exceeded three standard deviations of $D_{\Delta 1}$ were removed from the whole brain tissue mask. Subjects who had over 90% of their voxels removed due to the presence of artefacts were eliminated from the final analysis.

A 4D volumetric strain map was then created for each subject at each field strength by computing the divergence of their respective registered tissue displacement maps within the artefact-free tissue mask. It should be noted that the divergence operation additionally eroded the masks, further ensuring that only tissue volumetric strain was evaluated. The mean of the volumetric strain map within the modified whole brain tissue mask was computed for each cardiac phase, allowing the creation of a volumetric strain curve for all subjects. As the POx trace is delayed with respect to the R-wave peak of the VCG waveform, data from the subject triggered with the POx was shifted by 370 ms to correct for this delay during the normalisation step. Each strain curve was resampled to 20 cardiac phases in the interval from 0-95% of the cardiac cycle of the respective subject.
To evaluate white and grey matter tissue volumetric strain differences, volumetric strain curves were obtained as described above but instead using grey and white matter masks separately. These were obtained by thresholding the respective probability maps at 0.95 and also modified to remove CSF and artefacts.

SNR
4D SNR maps were created for each subject by dividing the magnitude image by the standard deviation of the noise, which was obtained by applying a moving standard deviation filter (15x15x15 pixels) to the real and imaginary noise images, and then taking the root sum of

squares of the real and imaginary standard deviations[20]. All SNR maps were transformed to each subject's respective T1-weighted image space, in similarity with the displacement maps.

The SNR for each subject was evaluated by averaging the values contained in the registered SNR map, which was masked by the aforementioned whole brain tissue mask, which was not modified to remove artefacts (as artefacts were limited in the RL acquisitions), or CSF. The SNR of the first heart phase was used to determine the 7T to 3T SNR ratio. The SNR coefficient of variation (CoV) over the cardiac phases was calculated to assess the effectiveness of the variable flip angle approach. The mean SNR for all subjects was used to calculate the expected voxel-wise uncertainty in the computed volumetric strain map (see Eq. [7] in Chapter 2 (part III)).

3. Results

Tissue Motion

The DENSE acquisitions in all directions for all subjects were successfully acquired at both 7T and 3T. However, analysis of the physiology data for two subjects at 7T showed inconsistent VCG triggering between the three DENSE datasets for the three motion directions. Therefore, those two subjects were removed from the displacement and volumetric strain analyses at 7T (no subjects at 3T were found to have inconsistent VCG triggering). Additionally, one subject at 7T and two subjects at 3T were not included in the analysis because over 90% of their voxels (relative to the whole brain tissue mask) were removed by the artefact removal algorithm. Analysed subjects had mean 72.3±5.3 % (7T) and 59.9±16.6 % (3T) voxels remaining in the volumetric strain map. Thus, five subjects were analysed at 7T and six at 3T. Figure 2 shows example magnitude, displacement and volumetric strain images at both field strengths. The general observed brain tissue motion was towards the centre of the brain and down towards the spinal canal.

The overall shape of the whole brain tissue volumetric strain curves was similar at both field strengths, with both attaining their peak value at approximately 32% of the cardiac cycle (Figure 3). Mean whole brain peak volumetric strains were (mean ± SD): $(4.5 \pm 1.0)*10^{-4}$ and $(5.1 \pm 1.2)*10^{-4}$ for 7T and 3T respectively. The peak grey and white matter volumetric strain was defined as their respective values at the time of peak for the whole brain tissue. At 7T, the peak volumetric strain of grey matter was $(7.2 \pm 0.6)*10^{-4}$ while for white matter the peak value was $(2.3 \pm 1.3)*10^{-4}$ (Figure 4). The mean peak grey matter to white matter volumetric strain ratio was 4.4 ± 2.8 (median: 3.2, IQR: 4.1, see Figure 4b). A two-sample t-test for the difference in the means of the peak grey and white matter values (assuming unequal variances) was significant ($p< 0.001$). Similar values for peak grey and white matter volumetric strain were found at 3T. At 3T, the peak grey matter volumetric strain was $(8.3 \pm 2.4)*10^{-4}$ and the peak white matter value was $(2.1 \pm 0.5)*10^{-4}$, resulting in a mean peak grey matter to white matter volumetric strain ratio of 4.0 ± 1.2 (median: 3.2, IQR: 1.7). Differences

between the means of grey and white matter peak volumetric strains (similarly assessed by a two-sample t-test) was also significant ($p<0.002$).

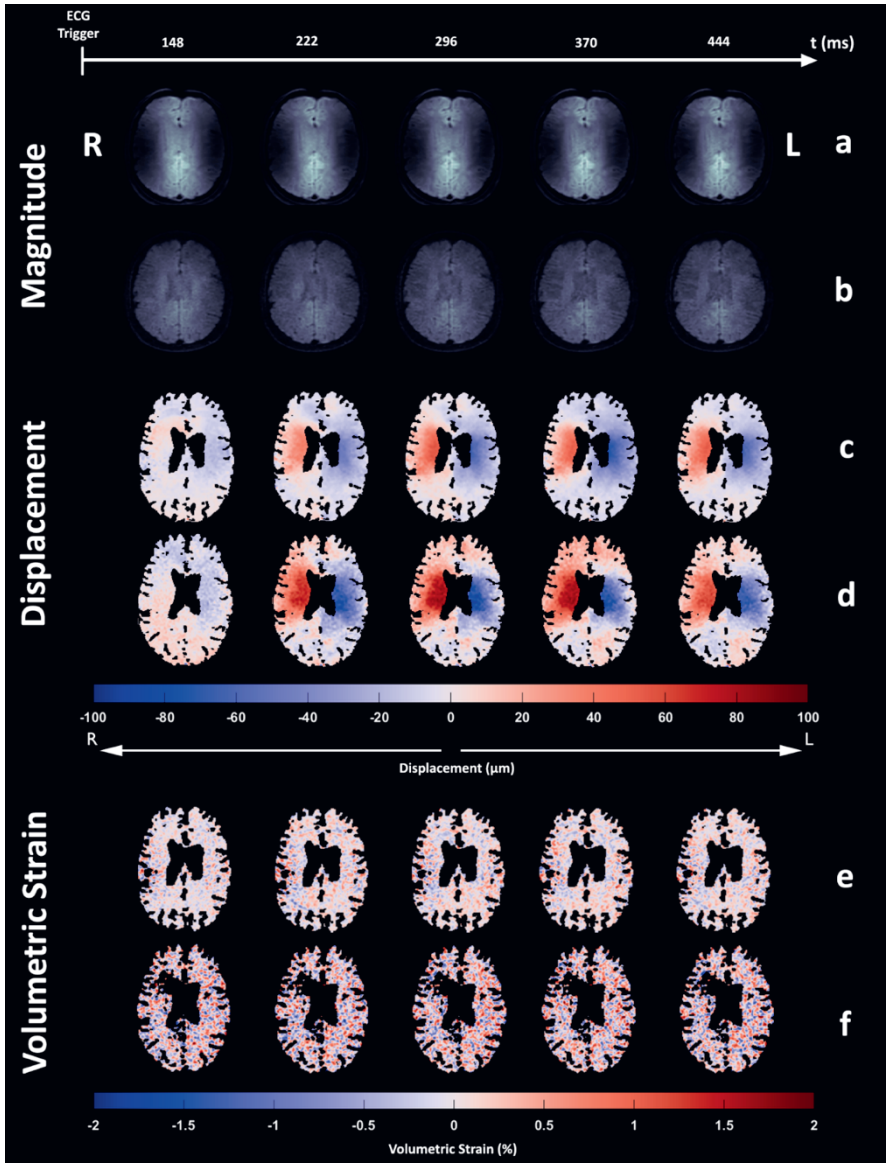

Figure 2. DENSE RL magnitude (a, b) and displacement (c, d) images for the 2nd through 6th acquired frames of the cardiac cycle of one subject at 7T and 3T, respectively. The corresponding volumetric strain maps are shown for 7T (e) and 3T (f). While the displacement maps show the tissue mask free of CSF voxels, the volumetric strain maps shown here additionally reflect mask erosion due to the computation of spatial derivatives as well as the removal of noise/artefacts. The higher SNR at 7T is apparent from the smoothness of the displacement maps. Anatomical left and right are indicated by R and L, hence the hemispheres are captured moving towards each other shortly after the ECG trigger.

SNR

The mean SNR for all subjects at 7T and 3T was (mean ± SD) 22.0 ± 7.3 and 7.0 ± 2.8 respectively. The mean 7T to 3T SNR ratio was 3.2 ± 0.7. Intensity changes over the cardiac cycle were limited, reflected by a low CoV, which was well below 10% for all subjects. The SNR at both field strengths was found to be higher at the edges of the brain closest to the receive coil (Figure 5). From Eq. [7] (see Chapter 2 (part III)) the expected voxel-wise uncertainty in the computed volumetric strain was found to be $1.4*10^{-3}$ and $4.4*10^{-3}$ for 7T and 3T, respectively. The uncertainty in the mean whole brain volumetric strain curves was smaller due to averaging over all subjects and over the number of voxels contained in the brain tissue masks, having values of $1.5*10^{-6}$ and $5.2*10^{-6}$ (mean ROI size: $0.9*10^{6}$ and $0.7*10^{6}$ voxels) for 7T and 3T, respectively. Figure 6 shows the reduction in uncertainty of the displacement and volumetric strain maps when a 15x15x15 moving average filter is applied to the displacement and volumetric strain data within the grey and white matter masks separately.

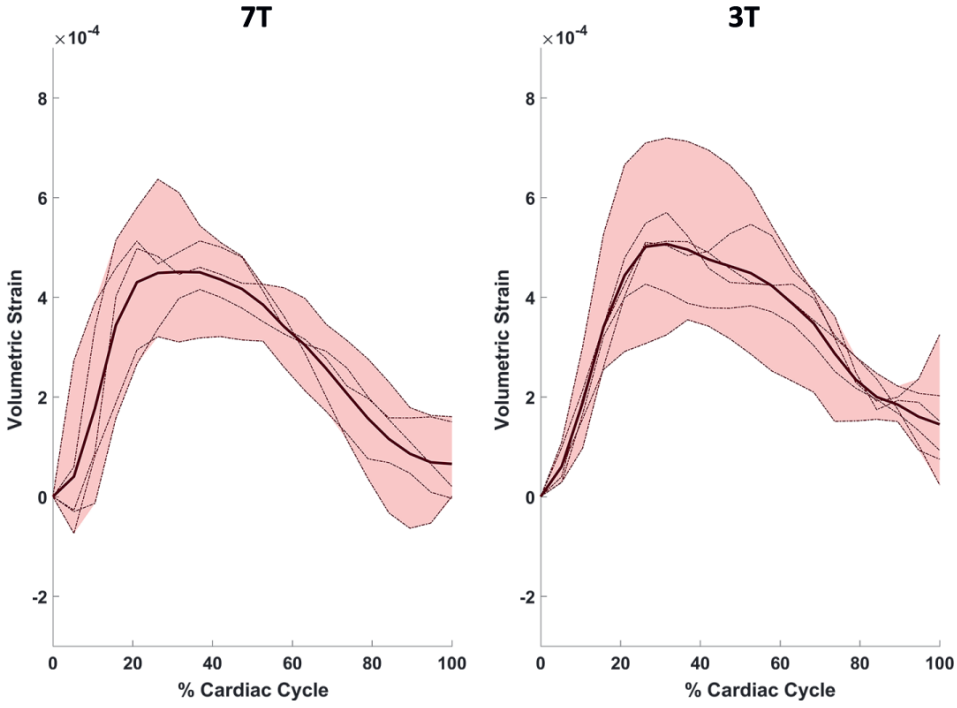

Figure 3 The mean whole brain tissue volumetric strain (bold lines) for all subjects over the cardiac cycle at 7T and 3T. The shaded region around the mean strain curve indicates the range between maximum and minimum variation among subjects. The dotted lines represent the individual strain curves for the subjects included in the strain analysis at either field strength (n=5 at 7T and n=6 at 3T).

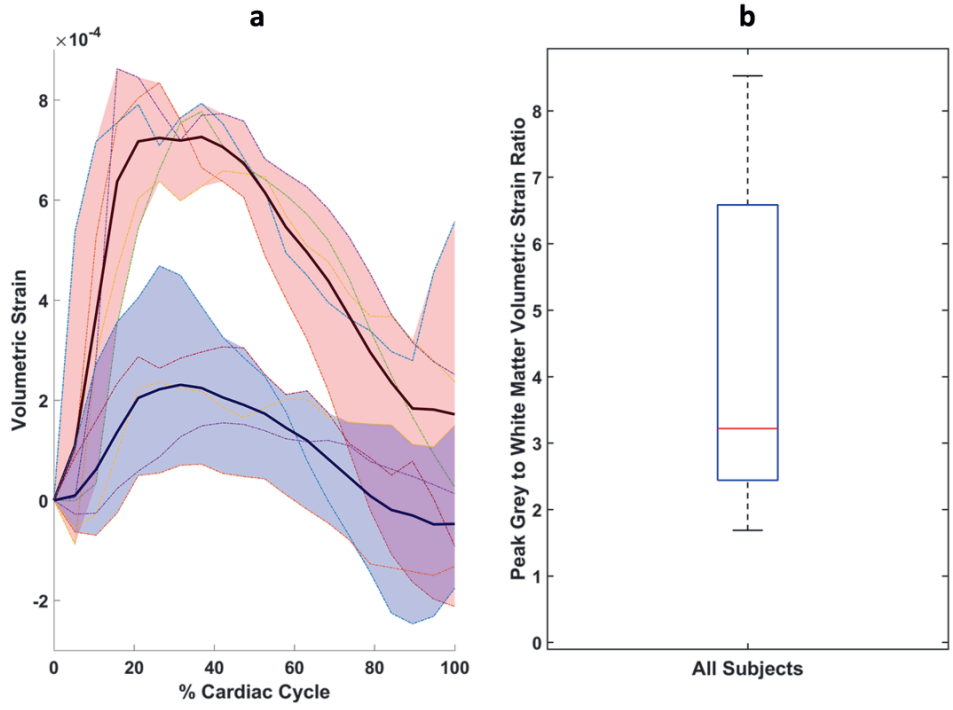

Figure 4. a) Grey and white matter mean volumetric strain curves (bold lines in red and blue shaded areas, respectively) for 7T. The shaded region around the mean strain curves indicates the range between maximum and minimum variation among subjects for grey (red) and white (blue) matter. The coloured lines within the shaded regions represent the volumetric strain curve for the same individual subjects for the respective tissue types. b) Box plot of the peak grey to white matter volumetric strain ratio, defined as the ratio of their respective values at the time of peak for the mean whole brain tissue curve (approximately 32% of the cardiac cycle). The whisker length of the box plot is set to display values exceeding ±2.7σ as outliers.

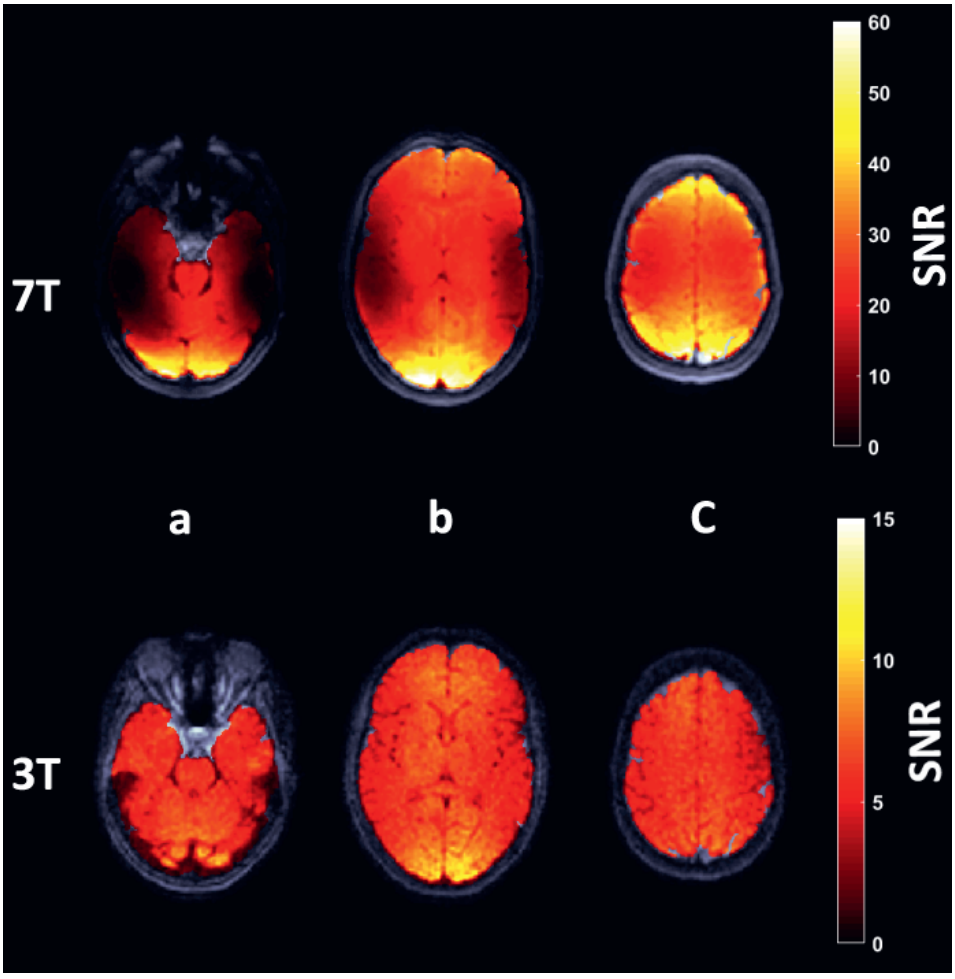

Figure 5. The masked SNR map overlaid on magnitude images for the same subject at 7T and 3T, here visualised at (a) low, (b) mid and (c) high transverse slices of the brain. Note the larger SNR colour range used in the 7T images due to the more than 3x larger SNR present at 7T. Greater SNR values were in general observed at the edge of the brain, corresponding to areas closer to the receive coils.

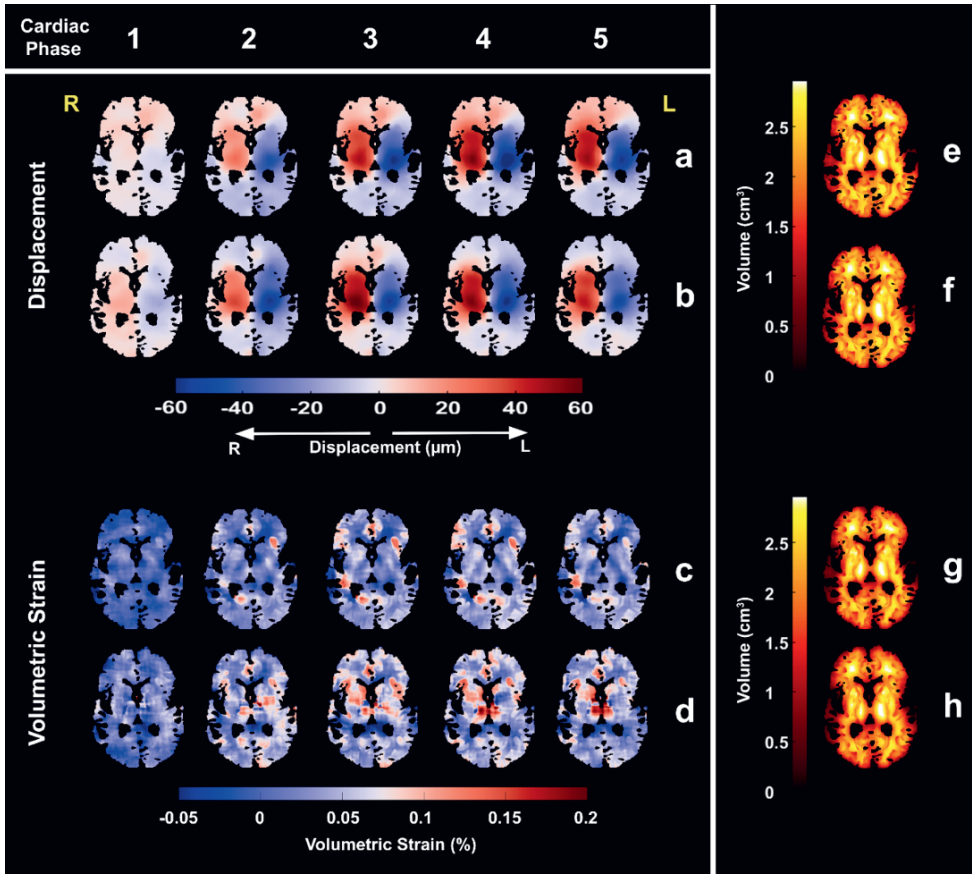

Figure 6. Example smoothed displacement and strain maps of the first 5 acquired cardiac phases for one subject at 7T (a,c) and 3T (b,d). Smoothed displacement and strain maps were obtained by applying a 15x15x15 moving average filter to the separate grey and white matter masked maps (GM or WM probability >= 0%, CSF 0%). The filtered grey and white matter maps were then combined into one map by weighting with their respective probability maps. Voxels in the strain map with absolute strains exceeding 1% were removed before smoothing. The effective volume used within the moving average filter is shown for the displacement and strain maps at 7T (e,g) and 3T (f,h). The smoothed volumetric strain maps clearly show grey-white matter contrast in various regions that is consistent between 3T and 7T measurements.

4. Discussion

Tissue Motion

In this study, we implemented a 3D cine-DENSE at 7T to assess the cardiac-induced brain tissue volumetric strain in healthy subjects. We found a consistent pattern of tissue volume change amongst all subjects, with expansion (volume increase) occurring during the first 30% of the cardiac cycle. We also observed approximately four times higher peak volumetric strains of grey matter compared with white matter, which demonstrates the feasibility of DENSE as a tool to elucidate differences in the pulsatile behaviour of the brain's anatomical structures. Compared with 3T, DENSE at 7T yields a factor of 3 more SNR, which is currently not enough for a voxel-wise analysis of the volumetric strain as will be discussed further below.

The sharp, positive gradient of the strain curve between 0 and ~30% of the cardiac cycle suggests that volumetric strain reflects rapid expansion of the brain tissue due to a fast increase in blood volume of the small vessels within the tissue during systole, instead of tissue compression caused by the large vessels outside the brain tissue. The negative slope of the strain curve likely reflects relaxation of the brain tissue (due to outflow of venous blood) during diastole to its original state. The peak volumetric strain values found in this study show good agreement with other methods of evaluating brain volume changes over the cardiac cycle in healthy subjects. Hirsch et al.[14] found brain tissue peak volumetric strain values of $(2.8 \pm 1.9)*10^{-4}$ for an ROI in white matter. Volumetric strain can equivalently be characterised in terms of the physical volume change if the initial volume is known. Applying the average volume used in the whole brain tissue mask as an estimate for the initial volume, the mean peak delta volume in this study was 0.47 ml ± 0.10 ml and 0.53 ± 0.13 ml for 7T and 3T respectively. Under the Monroe-Kellie doctrine, these changes in brain tissue volume over the cardiac cycle should balance the CSF volume displaced into the spinal canal over the same time period[6,7]. The measured changes in brain tissue volume for this study compare favourably with the values of displaced CSF volumes reported in the literature (0.46 ± 0.15 ml, 0.51 ± 0.17 ml, 0.55 ± 0.12 ml, 0.58 ± 0.12 ml, 0.71 ± 0.32 ml, 0.77 ± 0.23 ml)[21–26]. Changes in blood volume within the larger arteries over the cardiac cycle may also contribute to the caudally displaced CSF volume, making it difficult to disentangle the effect of arterial blood and brain tissue volume changes on spinal CSF volume dynamics. However, the expansion of the brain tissue appears to be a greater effect given the relative timings of CSF and blood outflow from the head in comparison with the termination of arterial expansion[7], thereby allowing reasonable comparison of cardiac-induced brain tissue swelling with displaced spinal CSF volume. Additionally, compression of the venous system may also accommodate the expanding brain tissue and arterial volumes within the intracranial vault.

Volumetric strain is induced by the swelling of blood vessels within the incompressible tissue during systole[7,14] , and therefore also contains information on tissue stiffness. White matter has been observed to be stiffer than grey matter[27] which may explain the results of our study,

where smaller volumetric strains were consistently found in the former in comparison with the latter. Thus, even under the assumption that the systolic blood volume change is proportional to the baseline blood volume, the ratio of the peak white and grey matter volumetric strains found in this study would not reflect the ratio of the blood volumes that occupies these two tissue types. Results found in the literature also support this view. Exploiting an MRI technique which combined arterial spin labelling and blood oxygen-level dependent effects, Bulte et al. obtained a grey-to-white matter blood volume ratio of 1.56[28]. Vonken et al.[29] and Artzi et al.[30] utilized dynamic susceptibility contrast MRI to find a higher ratio of 1.87 and 2.38, respectively. The considerably higher ratio found in this study between these two tissue types thus demonstrates the entangled tissue blood volume change and stiffness information contained within the volumetric strain measurement. The expansion of leptomeningeal arteries running within tightly folded sulci may also force apart the surrounding tissue. Such tissue displacements would still be incorporated within our tissue masks, and would result in an apparent volumetric strain that is not derived from the swelling of the small vessels. As CSF fills the sulci and fissures of the brain, the contribution of these areas containing 'artificial tissue expansion' on our estimations of brain tissue volumetric strain was therefore limited due to the removal of CSF regions from the analysis. However, the segmentation of CSF can be insufficient in regions where the grey matter is tightly folded, resulting in the retention of these areas within the volumetric strain map. The number of voxels where this occurs is difficult to quantify manually, but is expected to be small relative to the total number of voxels used in the estimation of small vessel pulsation. Therefore, while the contribution of these areas containing 'artificial tissue expansion' is likely suppressed through averaging, it nonetheless could also partially explain the larger volumetric strain observed in the grey matter compared to white matter.

Owing to the difficulty of visualising the small vessels in vivo, cSVD is typically assessed by imaging the lesions found within the brain parenchyma that arise from the disease. Volumetric strain is however a parameter map derived from the joint 'mechanical' contributions of both the viscoelastic tissue and the changing blood volume occupying the underlying small vessels. Thus, it may be well suited as a potential neuroimaging biomarker for cSVD, conceivably even before the onset of lacunar infarcts and white matter lesions which characterise the disease, and also during its progression[2]. In that case, these volumetric strain maps would offer a powerful tool for elucidating the pathophysiology of the disease. As the heart is the primary input to the studied intracranial dynamics, changes in cardiac function as a result of age or disease may also affect brain tissue volumetric strain measurements. Thus, normalisation to cardiac function may be necessary to effectively evaluate any changes in brain tissue volumetric strain that would occur in the presence cSVD. Additionally, the viscoelastic tissue properties can be derived from cardiac-related displacement maps obtained by elastography[1]. This would allow (at least partially) to disentangle the changes in the volumetric strain due to the small vessels from the differences in tissue properties as assessed from elastography in cSVD

Various cine-MRI based approaches such as magnetic resonance elastography, phase contrast MRI and DENSE have been used to measure brain tissue pulsatility[4,7,14]. Of note, the high availability of pre-implemented phase contrast MRI sequences on the scanners of various MR vendors offers in principle a straightforward method to compute brain tissue displacement from the integrated velocity measurements and hence to calculate volumetric strain, provided a very low velocity encoding (below 1 cm/s) is allowed by the user interface. However, strong bipolar gradients and short ramp times are necessary to encode the low velocities of brain tissue motion, which leads to relatively long repetition times due to gradient duty cycle limitations, and which can result in large phase errors due to eddy currents[31]. Additionally, the integration procedure that is needed to compute the displacement fields from the velocity maps increases the uncertainty in the resulting strain map, potentially limiting its use in quantification of brain tissue expansion. Therefore, considering the much greater sensitivity to motion of DENSE compared with phase contrast MRI, DENSE appears to be a better overall tool for investigating the phenomenon of brain tissue expansion despite its inherently low SNR.

SNR

The acquisition of a separate noise map avoided typical problems in SNR calculations that can occur when the signal and noise values are from different spatial locations[32]. By averaging over all voxels containing brain tissue, the SNR analysis yielded representative SNR values to study the field strength dependence. The observed SNR differences may be partially affected by the differing gradient performance and coils available on both MR systems. The spatial variation in SNR observed at 7T may reflect the spatial inhomogeneity of the transmitted flip angles and the local sensitivity of the close-fitting 32 receive coils. Nevertheless, at 7T the SNR performance is likely improved over that at 3T thanks to the greater number of coil elements[33] and the closer fit of the receive coil to the subject's head. While this effect is minimised in the deeper areas of the brain, it may explain the 7T to 3T SNR ratio of 3.2 found in this study, which is higher than the expected value of 2.66. Although the higher SNR allows computation of a volumetric strain map with less uncertainty, the mean values for peak volumetric strain at 7T and 3T found in this study are approximately one order of magnitude lower than the calculated uncertainty per voxel, which currently limits the feasibility of a voxel-wise analysis for the current resolution (2.2 mm isotropic).

A reduction of the noise in our DENSE measurements by about a factor of 10 would permit a voxel-wise analysis of the peak volumetric strain map. This could be feasible (at the cost of temporal information) by acquiring a single cardiac phase at peak strain. In this case the use of a fixed 90° excitation pulse could be employed to vastly improve the SNR compared with the variable flip angle strategy used in this study[34]. Further improvements in SNR through the use of specialised local surface coils may also facilitate a voxel-wise analysis of peak volumetric strain in superficial brain regions. Also, de-noising algorithms exist that

show considerable improvement in other noisy MRI data such as cardiac motion[35] and diffusion weighted imaging[36]. These improvements remain the focus of future work.

Boosting the SNR by increasing the voxel size may also be a reasonable strategy for reducing the uncertainty in the volumetric strain map. Increasing the voxel size is more efficient than simply averaging over a greater number of smaller voxels. By way of illustration, averaging over two voxels can increase the SNR in the strain maps by $\sqrt{2}$ whereas increasing the voxel size by a factor of two to occupy a similar volume increases the SNR by a factor of $2\sqrt{2}$, (SNR_M increases by $\sqrt{2}$ and the derivative is more stable due to the larger distance between voxels, Eq. [7] in Chapter 2 (part III)), while it even speeds up the acquisition by a factor of 2. However, this strategy of increasing the voxel size should be used with restraint to avoid partial volume effects. Finally, the use of other acquisition strategies, such as those employing a balanced displacement encoding[37] may also boost the SNR efficiency.

The B1 inhomogeneity and T1 variation throughout the brain tissue limits the effectiveness of the variable flip angle approach as proposed by Fischer et al.[18] at both field strengths. Nonetheless, the low CoV values for all subjects indicates that the variable flip angle approach used in this study produces good signal stability over the cardiac cycle.
In this study we employed an EPI readout as it has a high speed and high SNR-efficiency[38], which is needed for this application. Consequently, we observed typical geometric EPI distortions (most visible in the prefrontal cortex) arising from off resonance spins due to the main magnetic field inhomogeneity. Using a spiral acquisition scheme may further increase the SNR[39], but requires currently offline reconstruction including compensation for the image blur from main field inhomogeneity which may be considerable at 7T. Unlike DENSE for cardiac applications, we didn't observe typical EPI artefacts induced by fast motion, which also could be alleviated by spiral readouts[40]. This is probably due to a generally lower amount of motion in the brain images, in combination with a very high motion encoding frequency, which effectively spoils the fast moving blood in the larger arteries.

Finally, a complete dataset of three orthogonal displacement measurements is required for volumetric strain computation. Image artefacts in any of these datasets, or de-synchronicity between the three datasets could cause inaccurate calculations. Similar to Soellinger et al.[4] we observed artefacts in our DENSE images, which were most pronounced at the end of the cardiac cycle, and most severe in the FH displacement datasets. These artefacts were excluded from our volumetric strain. However, the whole brain tissue strain curve seems not to fully return to the initial value as one would expect for measurements of 100% of the cardiac cycle, which suggests imperfect artefact removal. Retrospective gating and/or motion navigators may reduce these artefacts while speeding up the acquisition. Further work is also needed to establish the reproducibility of this method and to develop a more time-efficient, artefact-free cine-DENSE to evaluate the potential for investigating differences between

healthy subjects and the ageing population or patients with cSVD. An interesting candidate for improving the cine-DENSE could come from combining compressed sensing and parallel imaging, a technique which was recently shown for cardiac imaging[41].

5. Conclusion

This study demonstrated that DENSE at 7T and 3T allows the quantification of cardiac-induced whole brain tissue motion, despite the inherently low SNR of the DENSE acquisition. The method was shown at 7T to be sufficiently sensitive to detect physiological differences in volumetric strain, such as between grey and white matter in healthy human subjects, reflecting the difference in pulsatile behaviour between these two tissue types. Thus, the method holds potential for studying the blood volume pulsations of the cerebral small vessels, both under healthy conditions and in diseases such as cSVD.

References

1. Weaver, J. B. *et al.* Brain mechanical property measurement using MRE with intrinsic activation. *Phys Med Biol* **57**, 7275–7287 (2012).
2. Sack, I. *et al.* The impact of aging and gender on brain viscoelasticity. *Neuroimage* **46**, 652–657 (2009).
3. Tsao, C. W. *et al.* Relations of arterial stiffness and endothelial function to brain aging in the community. *Neurology* **81**, 984–991 (2013).
4. Soellinger, M., Rutz, A. K., Kozerke, S. & Boesiger, P. 3D cine displacement-encoded MRI of pulsatile brain motion. *Magn Reson Med* **61**, 153–162 (2009).
5. Bianciardi, M. *et al.* The pulsatility volume index: an indicator of cerebrovascular compliance based on fast magnetic resonance imaging of cardiac and respiratory pulsatility. *Philosophical Transactions of the Royal Society A: Mathematical, Physical and Engineering Sciences* **374**, 20150184 (2016).
6. Enzmann, D. R. & Pelc, N. J. Cerebrospinal fluid flow measured by phase-contrast cine MR. *AJNR Am J Neuroradiol* **14**, 1301–1307 (1993).
7. Greitz, D. *et al.* Pulsatile brain movement and associated hydrodynamics studied by magnetic resonance phase imaging. *Neuroradiology* **34**, 370–380 (1992).
8. Poncelet, B. P., Wedeen, V. J., Weisskoff, R. M. & Cohen, M. S. Brain parenchyma motion: measurement with cine echo-planar MR imaging. *Radiology* **185**, 645–651 (1992).
9. Feinberg, D. A. & Mark, A. S. Human brain motion and cerebrospinal fluid circulation demonstrated with MR velocity imaging. *Radiology* **163**, 793–799 (1987).
10. Pujol, J. *et al.* Motion of the cerebellar tonsils in Chiari type I malformation studied by cine phase-contrast MRI. *Neurology* **45**, 1746–1753 (1995).
11. Zhu, D. C., Xenos, M., Linninger, A. A. & Penn, R. D. Dynamics of lateral ventricle and cerebrospinal fluid in normal and hydrocephalic brains. *Journal of Magnetic Resonance Imaging* **24**, 756–770 (2006).
12. Zhong, X. *et al.* Tracking brain motion during the cardiac cycle using spiral cine-DENSE MRI. *Med Phys* **36**, 3413–3419 (2009).
13. Pahlavian, S. H., Oshinski, J., Zhong, X., Loth, F. & Amini, R. Regional Quantification of Brain Tissue Strain Using Displacement-Encoding With Stimulated Echoes Magnetic Resonance Imaging. *J Biomech Eng* **140**, 081010 (2018).
14. Hirsch, S. *et al.* In vivo measurement of volumetric strain in the human brain induced by arterial pulsation and harmonic waves. *Magn Reson Med* **70**, 671–683 (2013).
15. Reese, T. G., Feinberg, D. A., Dou, J. & Wedeen, V. J. Phase contrast MRI of myocardial 3D strain by encoding contiguous slices in a single shot. *Magn Reson Med* **47**, 665–676 (2002).
16. Zhu, J.-M. & Smith, I. C. P. Stimulated Anti-Echo Selection in Spatially Localized NMR Spectroscopy. *Journal of Magnetic Resonance* **136**, 1–5 (1999).
17. Ogg, R. J., Kingsley, R. B. & Taylor, J. S. WET, a T1- and B1-Insensitive Water-Suppression Method for in Vivo Localized 1H NMR Spectroscopy. *J Magn Reson B* **104**, 1–10 (1994).
18. Fischer, S. E., McKinnon, G. C., Maier, S. E. & Boesiger, P. Improved myocardial tagging contrast. *Magn Reson Med* **30**, 191–200 (1993).
19. Klein, S., Staring, M., Murphy, K., Viergever, M. A. & Pluim, J. elastix: A Toolbox for Intensity-Based Medical Image Registration. *IEEE Trans Med Imaging* **29**, 196–205 (2010).
20. Henkelman, R. M. Measurement of signal intensities in the presence of noise in MR images. *Med Phys* **12**, 232–233 (1985).
21. Stoquart-ElSankari, S. *et al.* A Phase-Contrast MRI Study of Physiologic Cerebral Venous Flow. *Journal of Cerebral Blood Flow & Metabolism* **29**, 1208–1215 (2009).
22. Stoquart-El Sankari, S. *et al.* Phase-Contrast MR Imaging Support for the Diagnosis of Aqueductal Stenosis. *American Journal of Neuroradiology* **30**, 209–214 (2009).
23. Alperin, N., Lee, S. H., Sivaramakrishnan, A. & Hushek, S. G. Quantifying the effect of posture on intracranial physiology in humans by MRI flow studies. *Journal of Magnetic Resonance Imaging* **22**, 591–596 (2005).
24. Balédent, O. Imaging of the cerebrospinal fluid circulation. in *Adult Hydrocephalus* (ed. Rigamonti, D.) 121–138 (Cambridge University Press, 2014). doi:10.1017/CBO9781139382816.013.

25. Wåhlin, A., Ambarki, K., Birgander, R., Malm, J. & Eklund, A. Intracranial pulsatility is associated with regional brain volume in elderly individuals. *Neurobiol Aging* **35**, 365–372 (2014).
26. Wåhlin, A. *et al.* Phase contrast MRI quantification of pulsatile volumes of brain arteries, veins, and cerebrospinal fluids compartments: Repeatability and physiological interactions. *Journal of Magnetic Resonance Imaging* **35**, 1055–1062 (2012).
27. Jin, X., Zhu, F., Mao, H., Shen, M. & Yang, K. H. A comprehensive experimental study on material properties of human brain tissue. *J Biomech* **46**, 2795–2801 (2013).
28. Bulte, D., Chiarelli, P., Wise, R. & Jezzard, P. Measurement of cerebral blood volume in humans using hyperoxic MRI contrast. *J Magn Reson Imaging* **26**, 894–9 (2007).
29. Vonken, E. J., van Osch, M. J., Bakker, C. J. & Viergever, M. A. Measurement of cerebral perfusion with dual-echo multi-slice quantitative dynamic susceptibility contrast MRI. *J Magn Reson Imaging* **10**, 109–17 (1999).
30. Artzi, M. *et al.* Human cerebral blood volume measurements using dynamic contrast enhancement in comparison to dynamic susceptibility contrast MRI. *Neuroradiology* **57**, 671–8 (2015).
31. Krishnamurthy, L. C., Mao, D., King, K. S. & Lu, H. Correction and optimization of a T2-based approach to map blood oxygenation in small cerebral veins. *Magn Reson Med* **75**, 1100–1109 (2016).
32. Dietrich, O., Raya, J. G., Reeder, S. B., Reiser, M. F. & Schoenberg, S. O. Measurement of signal-to-noise ratios in MR images: Influence of multichannel coils, parallel imaging, and reconstruction filters. *Journal of Magnetic Resonance Imaging* **26**, 375–385 (2007).
33. de Zwart, J. A. *et al.* Signal-to-noise ratio and parallel imaging performance of a 16-channel receive-only brain coil array at 3.0 Tesla. *Magn Reson Med* **51**, 22–26 (2004).
34. Sigfridsson, A., Haraldsson, H., Ebbers, T., Knutsson, H. & Sakuma, H. In vivo SNR in DENSE MRI; temporal and regional effects of field strength, receiver coil sensitivity and flip angle strategies. *Magn Reson Imaging* **29**, 202–208 (2011).
35. Spottiswoode, B. S. *et al.* Tracking myocardial motion from cine DENSE images using spatiotemporal phase unwrapping and temporal fitting. *IEEE Trans Med Imaging* **26**, 15–30 (2007).
36. St-Jean, S., Coupé, P. & Descoteaux, M. Non Local Spatial and Angular Matching: Enabling higher spatial resolution diffusion MRI datasets through adaptive denoising. *Med Image Anal* **32**, 115–130 (2016).
37. Zhong, X., Helm, P. A. & Epstein, F. H. Balanced multipoint Displacement encoding for DENSE MRI. *Magn Reson Med* **61**, 981–988 (2009).
38. Kim, D., Gilson, W. D., Kramer, C. M. & Epstein, F. H. Myocardial tissue tracking with two-dimensional cine displacement-encoded MR imaging: development and initial evaluation. *Radiology* **230**, 862–71 (2004).
39. Zhong, X., Spottiswoode, B. S., Meyer, C. H., Kramer, C. M. & Epstein, F. H. Imaging three-dimensional myocardial mechanics using navigator-gated volumetric spiral cine DENSE MRI. *Magn Reson Med* **64**, 1089–1097 (2010).
40. Zhong, X., Spottiswoode, B. S., Meyer, C. H. & Epstein, F. H. Two-dimensional Spiral Cine DENSE. *Proceedings of the International Society for Magnetic Resonance in Medicine* **7**, 756 (2007).
41. Chen, X. *et al.* Accelerated two-dimensional cine DENSE cardiovascular magnetic resonance using compressed sensing and parallel imaging. *Journal of Cardiovascular Magnetic Resonance* **18**, 1–14 (2016).

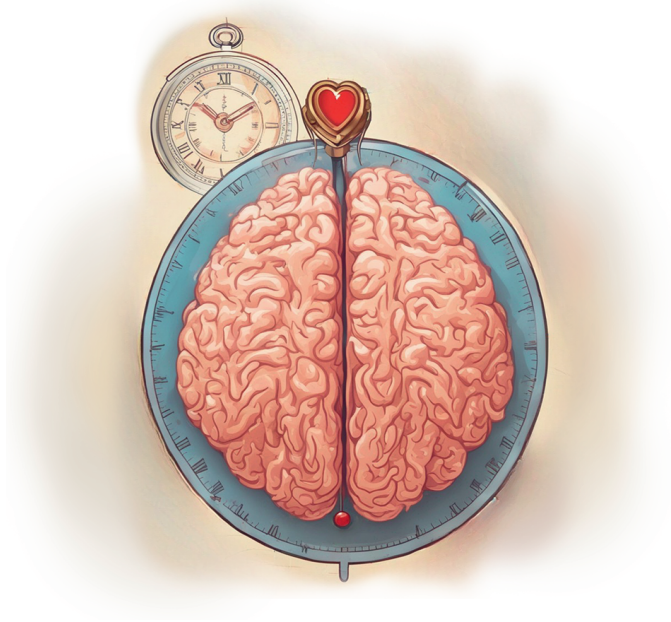

Chapter 2 (Part II)

Verification of DENSE brain tissue measurements using PC-MRI

This chapter is based on the research article published as: Adams, A. L., Kuijf, H. J., Viergever, M. A., Luijten, P. R., & Zwanenburg, J. J. M. (*2019*). *Quantifying cardiac-induced brain tissue expansion using DENSE*. NMR Biomed, *32*, e4050.

.

Chapter 2 (Part II)

1. Introduction

The investigation of cardiac-induced brain tissue volumetric strain as proposed in this study requires the acquisition of three orthogonally oriented displacement maps of brain tissue motion over the cardiac cycle. Naturally, the correct interpretation of the tissue volumetric strain (i.e., the amount of tissue expansion or compression) depends upon the correctness of the amplitudes and signs of the displacement maps used to compute the volumetric strain. To assess the correctness of the amplitudes and signs of brain tissue displacements obtained from our implementation of displacement encoding using stimulated echoes (DENSE), we compared velocity maps derived from these measurements with a vendor implemented phase contrast MRI (PC-MRI) acquisition.

2. Method

Velocity maps were acquired in the same directions as the DENSE measurements (Right-Left (RL), Anterior-Posterior (AP) and Feet-Head (FH)) using a vendor implemented PC-MRI acquisition. See Table 1 for PC-MRI scan parameters, which were designed to be comparable to those used in the DENSE acquisition. The two acquisitions were performed in the same subjects and data was acquired during the same scan session.

We then derived velocity maps from three DENSE measurements by taking the temporal derivative of the motion maps, and compared the DENSE derived velocity maps to the PC-MRI based velocity maps after temporal alignment. The PC-MRI measurements were acquired retrospectively, using the signal from a pulse oximeter placed on the finger to synchronize the acquisitions to the cardiac cycle. The signal from the pulse oximeter is delayed relative to the VCG signal used to trigger the DENSE acquisitions. This is due to the delay between the ventricular depolarisation at the heart (which gives a characteristic signal peak used in VCG prospective triggering) and the detection of the arterial pulse wave as it arrives at the pulse oximeter located at the finger. Therefore, after interpolating the DENSE-derived and PC-MRI mean velocity curves to the same temporal grid, the PC-MRI was shifted by approximately 215ms to account for this delay, thereby better aligning the time to peak of both curves.

Our analysis consisted of assessing, first, the general agreement of the global spatial patterns of the tissue velocity between the two acquisition methods, and second, the agreement of the mean velocity measured over the cardiac cycle within a region of interest (ROI) (see Figure 1).

3. Results & Discussion

The general spatial patterns of DENSE-derived and PC-MRI velocity maps were found to agree for all directions measured, see Figure 2. This confirms that the implementation of the DENSE technique was correct. The general shape and amplitudes of the mean-velocity curves at the selected ROI for both methods were also in agreement.

Parameter	Value
V_{enc} (mm/s)	3
Resolution (mm)	2.2 isotropic
FOV (mm) (FHxAPxRL)	250 x 250 x 190
TR (ms)	40
TE (ms)	25
EPI factor	15
Readout BW (Hz/pixel)	2258.4
EPI Phase Encoding BW (Hz/pixel)	84.2
Max. gradient strength (mT/m)	24
Max. gradient slew rate (T/m/s)	100
SENSE (AP x RL)	2.7 x 2.5
Flip angle (deg)	15
Triggering	Retrospective, (pulse oximeter)
Scan duration (at 60 beats per minute)	3 x 2.3 mins

Table 1. PC-MRI imaging parameters used to evaluate the correctness of DENSE displacement signs and amplitudes.

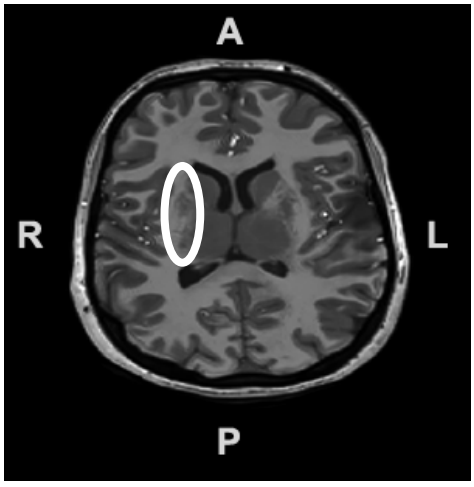

Figure 1. High resolution T1 image showing the approximate location of the ROI used to obtain the mean velocity curves. The ROI was placed at a location that best illustrates the unique profiles of the mean velocity for each measured direction.

The primary peak (or dip for the FH dataset due to the negative velocities) observed in the mean velocity curves for all directions is likely related to tissue motion induced by the arterial pulse wave during systole[1], while the secondary peak (or dip in FH) possibly arises from the energy deposited to the brain by the reflected arterial pulse wave.

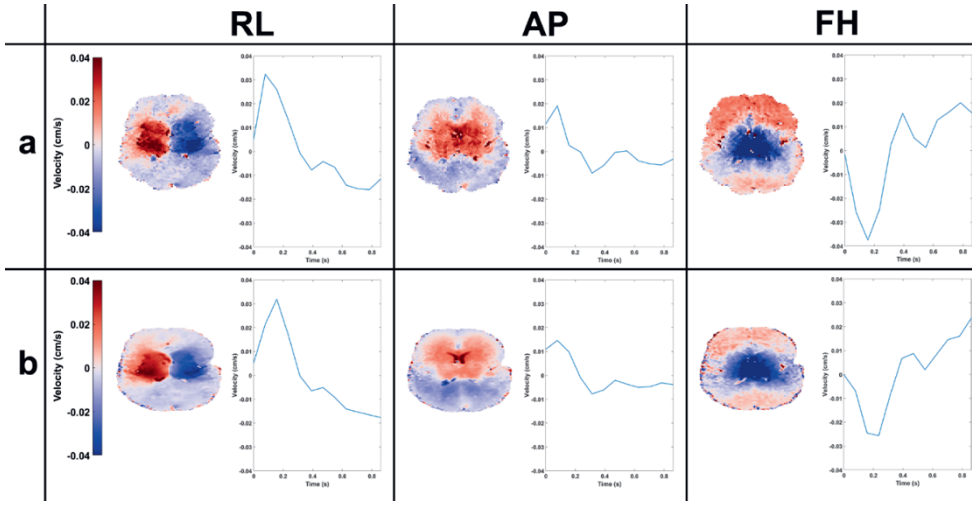

Figure 2. a) RL, AP and FH PC-MRI brain tissue velocity maps of a subject shown at the moment of peak velocity measured over the cardiac cycle for each respective direction. The corresponding mean velocity curve for the ROI indicated in Figure 1 is also shown, for all acquired phases of the cardiac cycle. b) DENSE-derived velocity maps of the same subject in the RL, AP and FH directions, also shown at the moment of peak velocity. The corresponding mean velocity curve for the ROI indicated in Figure 1 is also shown. The PC-MRI images are shown with the acquired resolution (2.3 mm isotropic), while the DENSE-derived velocity maps shown here were registered and interpolated (without smoothing) to the subject's high resolution T1 image (1.0 mm isotropic). This may partially explain the smoother appearance of the DENSE velocity maps in comparison to the PC-MRI images, although most of the smooth appearance is due to the high SNR of the DENSE velocity maps. Positive (red) motion is directed towards the Left, Posterior and Head directions, respectively.

At the moment of peak velocity, the brain tissues were observed moving together towards the midline and down towards the spinal canal. This is consistent with the patterns of cardiac-induced tissue motion reported in the literature[1–4]. It is unclear as to why Soellinger et al. reported motion of the cerebral hemispheres away from each other in the right-left direction, despite also comparing their VCG triggered DENSE measurements to PC-MRI[5].

4. Conclusion

We found good agreement between PC-MRI and DENSE-derived velocity maps of brain tissue motion. The agreement between the two methods supports the notion that the DENSE displacement measurements used in this study had the correct signs and amplitudes. This strengthens the finding of mean positive whole brain tissue volumetric strain over the cardiac cycle (reflecting expansion of brain tissue due to swelling of the microvasculature) and the associated amount of peak volume change reported in this study.

References

1. Greitz D, Wirestam R, Franck A, Nordell B, Thomsen C, Stahlberg F. Pulsatile brain movement and associated hydrodynamics studied by magnetic resonance phase imaging. *Neuroradiology*. 1992;34(5):370-380. doi:10.1007/BF00596493
2. Poncelet BP, Wedeen VJ, Weisskoff RM, Cohen MS. Brain parenchyma motion: measurement with cine echo-planar MR imaging. *Radiology*. 1992;185(3):645-651. doi:10.1148/radiology.185.3.1438740
3. Weaver JB, Pattison AJ, McGarry MD, et al. Brain mechanical property measurement using MRE with intrinsic activation. *Phys Med Biol*. 2012;57(22):7275-7287. doi:10.1088/0031-9155/57/22/7275
4. Hirsch S, Klatt D, Freimann F, Scheel M, Braun J, Sack I. In vivo measurement of volumetric strain in the human brain induced by arterial pulsation and harmonic waves. *Magn Reson Med*. 2013;70(3):671-683. doi:10.1002/mrm.24499
5. Soellinger M, Rutz AK, Kozerke S, Boesiger P. 3D cine displacement-encoded MRI of pulsatile brain motion. *Magn Reson Med*. 2009;61(1):153-162. doi:10.1002/mrm.21802

Chapter 2 (Part III)

A theoretical analysis of noise propagation in the quantification of brain tissue expansion

This chapter is based on the research article published as: Adams, A. L., Kuijf, H. J., Viergever, M. A., Luijten, P. R., & Zwanenburg, J. J. M. (*2019*). *Quantifying cardiac-induced brain tissue expansion using DENSE*. NMR Biomed, *32*, e4050.

The relationship between SNR and volumetric strain uncertainty (noise) is better understood through a voxel-wise error propagation analysis. The volumetric strain is defined here as the regional change in tissue volume ΔV (due to a change in blood volume) relative to the original volume V: $\varepsilon_v = \frac{\Delta V}{V}$. Under the assumption of very small normal deformations, the dimensionless volumetric strain ε_v can be approximated from the divergence of the displacement field D

$$\varepsilon_v \approx \nabla \cdot D = \frac{\partial D_x}{\partial x} + \frac{\partial D_y}{\partial y} + \frac{\partial D_z}{\partial z} \qquad [1]$$

where ∇ is the divergence operator and $\frac{\partial D_x}{\partial x}, \frac{\partial D_y}{\partial y}$ and $\frac{\partial D_z}{\partial z}$ are the partial derivatives of the displacement field D along orthogonal x,y and z directions, respectively. Each orthogonal component of D can be calculated from a pair of motion-sensitive phase images acquired through DENSE by

$$D_{x,y,z} = \frac{D_{enc_{x,y,z}}}{\pi} \times \Delta\varphi_{x,y,z}\,. \qquad [2]$$

where Δφ is the difference image formed by the subtraction of the two displacement encoded phase images with opposite polarity of the encoding gradient to remove the background phase, and D_{enc} is the displacement encoding value in units of meters (similar to the V_{enc} parameter used in phase-contrast MRI, which has units of meters/second).

Of interest is σ_{ε_v}, the resulting noise present in the volumetric strain map. The noise in a single displacement encoded phase image (which is motion encoded in one direction, say, *x*), is related to the SNR in the corresponding magnitude image by

$$\sigma_\varphi = \frac{1}{SNR_M}. \qquad [3]$$

Assuming that the SNR_M in the pair of phase images are the same, the subtraction step to remove the background phase increases the uncertainty (relative to a single phase image) by a factor of $\sqrt{2}$ i.e.

$$\sigma_{\Delta\varphi} = \sqrt{2} \times \sigma_{\varphi.} \qquad [4]$$

However, because the phase images have opposite signs, subtraction yields signal accumulation and the SNR in the resultant image is increased by $\sqrt{2}$.

Given Δx, the voxel size along x, we can define the strain in that direction as

$$\varepsilon_{xx\,(n)} \overset{\text{def}}{\equiv} \frac{D_x(n+1) - D_x(n-1)}{2\Delta x}. \qquad [5]$$

From Eqs. [2] and [5] the noise $\sigma_{\varepsilon_{xx}}$ thus is

$$\sigma_{\varepsilon_{xx}} = \frac{\sqrt{2}}{2\Delta x} \times \frac{D_{enc_x}}{\pi} \times \sigma_{\Delta\varphi}\,. \qquad [6]$$

A similar derivation can be made for the other two directions. Therefore, using Eqs. [3], [4] and [6], we find for the noise in the volumetric strain

$$\sigma_{\varepsilon_v} = \frac{1}{\pi \times SNR_M} \times \sqrt{\sum_{i=x,y,x} \left(\frac{D_{enc_i}}{\Delta i}\right)^2}. \qquad [7]$$

Thus, an improvement in SNR_M reduces the presence of noise in the volumetric strain maps linearly. Similarly, improving the motion sensitivity D_{enc} in all directions linearly reduces σ_{ε_v}. However, increasing the voxel size has a more than linear effect due to the accompanying increase in SNR_M.

Chapter 3

Validating faster DENSE measurements of cardiac-induced brain tissue expansion as a potential tool for investigating cerebral microvascular pulsations

This chapter is based on the research article published as: Adams, A. L., Viergever, M. A., Luijten, P. R., & Zwanenburg, J. J. M. (*2020*). *Validating faster DENSE measurements of cardiac-induced brain tissue expansion as a potential tool for investigating cerebral microvascular pulsations*. Neuroimage, *208*, 116466.

Abstract

Purpose

Displacement Encoding with Stimulated Echoes (DENSE) has recently shown potential for measuring cardiac-induced cerebral volumetric strain in the human brain. As such, it may provide a powerful tool for investigating the cerebral small vessels. However, further development and validation are necessary. This study aims, first, to validate a retrospectively-gated implementation of the DENSE method for assessing brain tissue pulsations as a physiological marker, and second, to use the acquired measurements to explore intracranial volume dynamics.

Method

We acquired repeated measurements of cerebral volumetric strain in 8 healthy subjects, and internally validated these measurements by comparing them to spinal CSF stroke volumes obtained in the same scan session.

Results

Peak volumetric strain was found to be highly repeatable between scan sessions. First/second measured peak volumetric strains were: $(6.4 \pm 1.7)\text{x}10^{-4}$ / $(6.7 \pm 1.6)\text{x}10^{-4}$ for whole brain, $(9.5 \pm 2.5)\text{x}10^{-4}$ / $(9.6 \pm 2.4)\text{x}10^{-4}$ for grey matter, and $(4.4 \pm 1.7)\text{x}10^{-4}$ / $(4.1 \pm 0.8)\text{x}10^{-4}$ for white matter. Grey matter showed significantly higher peak strain ($p<0.001$) and earlier time-to-peak strain ($p<0.02$) than white matter. An approximately linear relationship was found between CSF and brain tissue volume pulsations over the cardiac cycle (mean slope and R^2 of 0.88 ± 0.23 and 0.89 ± 0.07, respectively). The close similarity between CSF and brain tissue volume pulsations implies limited contributions from large intracranial vessel pulsations, providing further evidence for venous compression as an additional mechanism for maintaining stable intracranial pressures over the cardiac cycle. Cerebral pulsatility showed consistent inter-subject peak values in healthy subjects, and was strongly correlated to CSF stroke volumes.

Conclusion

These results strengthen the potential of brain tissue volumetric strain as a means for investigating the intracranial dynamics of the ageing brain in normal or diseased states.

1. Introduction

The small vessels which compose the cerebral microvasculature pulsate as a result of transient increases in intracranial blood volume during the cardiac cycle, thereby causing local tissue displacement[1]. Recently, we used an MR imaging technique called Displacement Encoding with Stimulated Echoes (DENSE)[2] to measure the pulsatile brain tissue motion and indirectly investigate changes in the microvascular blood volume over the cardiac cycle[3]. From the brain tissue motion, volumetric strain (change in tissue volume ΔV relative to the original volume V: $\varepsilon_v = \frac{\Delta V}{V}$) was computed. Peak volumetric strain showed differences between grey matter and white matter that matched the relative blood volume differences between these two tissue types, suggesting that tissue volumetric strain reflects swelling of the microvasculature embedded in the tissue. The ability to study the swelling of the microvasculature bed within the brain would be an advantage of DENSE over 'mass-balance' approaches that study blood- and CSF flows at the spinal canal[4,5], which cannot distinguish blood volume changes originating from the large vessels in the subarachnoidal CSF and volume changes originating from the vascular bed in the brain tissue.

Although DENSE comes at the cost of a factor of 2 in signal-to-noise (compared to a spin echo), it is an ideal method for investigating sub-voxel brain tissue motion as it permits the spatial quantification of sub-millimeter tissue motion, and inherently limits eddy current induced phase errors by temporally separating the motion encoding/decoding gradients through the use of a stimulated echo acquisition. For comparison, an optimized phase contrast velocity method would need an encoding velocity (V_{enc}) of about 1 mm/s (approx. maximally 300 µm motion during systole[3,6]), which implies the need for impractically large bipolar gradients, or a large loss in signal-to-noise due to the use of a strongly suboptimal V_{enc}. However, further development and validation of DENSE-derived volumetric strain measurements are necessary to ascertain the feasibility of this approach for investigating the changes to the cerebral microvasculature which may occur naturally with age or with disease. Previous measurements of brain tissue pulsatility were lengthy due to the use of a triggered acquisition that required to scan 120% of the cardiac cycle to obtain full coverage of the cardiac cycle. This effectively led to a repetition time between the motion encodings of two heartbeats (double scan duration), increasing the likelihood of motion artefacts and reducing the clinical viability of the method. Improvements to the acquisition scheme are therefore needed to allow full coverage of the cardiac cycle in a more efficient manner. Additionally, measurement repeatability would offer an insight into whether inter-subject peak volumetric strain variability reflects physiological variation or simply sensitivity of the volumetric strain calculation to noise. Furthermore, internal validation of brain tissue volumetric strain could be achieved through measurements of CSF stroke volume during the same scan session (as the cranial vault has a fixed volume, swelling of brain tissue or the arterial compartments must be compensated by displacing CSF spinally[7,8]).

This study aims, first, to validate a more efficient DENSE method for assessing brain tissue pulsations as a physiological marker, and second, to use the acquired measurements to explore intracranial volume dynamics. To achieve these aims, we first implemented a retrospectively-gated version of DENSE, which reduced the acquisition duration by half, and assessed the repeatability of the brain tissue volumetric strain by performing repeated measurements on healthy subjects. The cardiac-induced volumetric strain was analysed for the whole brain, as well as for grey and white matter tissue separately. Second, for internal validation we measured the CSF spinal stroke volumes as independent physiological measurements of the subjects. Finally, we used the CSF and DENSE measurements to further explore the physiology of intracranial volume dynamics by disentangling the contributions of the large intracranial extracerebral vessels and the cerebral microvasculature to spinally displaced CSF.

2. Materials and Methods

2.1 Measurements

To investigate the repeatability of brain tissue volumetric strain measurements, the DENSE protocol was performed twice within a two-hour period on the same day, with repositioning of the subjects. For the comparison of the DENSE measurements with an independent measurement in the same subjects, a CSF flow scan was also acquired. Informed consent for all measurements was obtained from 8 healthy young subjects of European descent without known cardiovascular or cerebral diseases (3 females, mean age: 27±6) to participate in the study, which was approved by the governing Ethical Review Board of our institution.

In the first scan session, three 4D (3D+time) brain tissue displacement measurements were acquired on a 7T MR scanner (Philips Healthcare) on which we implemented retrospectively-gated DENSE[9]. Similar to previous work[3], the three DENSE acquisitions covered the entire cardiac cycle in the right-left (RL), anterior-posterior (AP) and feet-head (FH) directions, and were acquired using opposite gradient polarities. Retrospectively-gated phase-contrast MRI (PCMRI) was used to acquire time-resolved 2D CSF flow measurements at the C2-C3 level. The PCMRI acquisition was sensitised for motion in the FH direction. Both DENSE and PCMRI measurements were performed using a 32 channel head coil (Nova Medical), and synchronised to the cardiac cycle using a pulse oximeter (POx) attached to the index finger on the left hand.

After the first scan session, subjects were briefly taken out of the MR scanner and allowed to move around freely (for a maximum of 10 minutes) before being repositioned into the scanner for the second scan session. During the second scan session, subjects were re-scanned using the same DENSE protocol as the first session.

Additionally, a 3D T1-weighted FFE scan was also made for both scan sessions for registration and segmentation of the brain tissue. See Table 1 for all relevant scan parameters.

Parameter	T1-weighted FFE	DENSE	PCMRI
Denc[1] (mm) (FH/AP/RL)	--	0.35/0.175/0.175	--
Venc[2] (cm/s) (FH)	--	--	5
Resolution (mm) (FHxAPxRL)	0.93 x 0.93 x 1	1.95 x 1.95 x 2.2	3 x 0.45 x 0.45
FOV (mm) (FHxAPxRL)	300x248x190	250x250x190	3x190x185
TR (ms)	4	35/30/35 (FH/AP/RL)	12
TE (ms)	2	8.7	6.1
EPI factor	--	15	--
TFE factor	600	2	2
Readout/phase BW (Hz/pixel)	405/--	2342/92	474/--
Inversion delay (ms)	1235	--	--
Max. gradient strength (mT/m)	40	30	25
Max. gradient slew rate (T/m/s)	200	150	150
SENSE (APxRL)	2 X 2	1.9 X 2.5	1 x 2
Flip angle (deg)	5	Variable[3]	30
Cardiac synchronization[4]	--	Retrospective	Retrospective
Phases/cardiac cycle	--	20	36 - 40
Scan duration (min:s)[5]	0:48	2:24	1:43

Table 1. Imaging parameters used in the study.
1. Denc: motion (either positive or negative) that induces phase wrap in the subtracted phase images, analogous to the Venc parameter in velocity encoded phase contrast imaging.
2. Velocity was measured in the FH direction. One subject was scanned with a Venc = 10 cm/s to eliminate phase wraps.
3. The flip angles were varied over the cardiac cycle to create a stable signal[10], assuming a T1 of 1100 ms. The maximum flip angle in the sweep was set to 30 degrees, in order to maintain/preserve longitudinal magnetization for tagging at the next cardiac cycle.
4. The retrospectively-gated acquisitions were performed using a pulse oximeter as the triggering device, which was attached to the left index finger.
5. Scan duration reported for a heart rate of 60 beats/min and for one motion encoding direction.

2.2 Analysis:
An identical analysis was performed on the DENSE images acquired from each scan session. The analysis comprised of several steps as described below.

2.2.1 Background Phase Removal
Background phase errors could be removed by subtraction of the two opposing gradient polarity images present for each DENSE acquisition. However, we observed that the background phase was stable for every acquired phase of cardiac cycle. Therefore, we

preferred to remove the background phase by subtracting the first acquired cardiac phase from all others, with the minor consequence of introducing an arbitrary offset which was irrelevant for our peak-to-peak based analysis. This has the benefit that the volumetric strain can be computed from the DENSE displacement fields for each gradient polarity separately, and later combined (after inversion of the negative gradient polarity). This allowed us to do artefact removal for each gradient polarity image, rather than on the level of the subtracted images.

2.2.2 Image Registration

Registration of the DENSE images was performed to correct for typical EPI distortions and subject motion between each displacement-sensitive acquisition. First, AP and FH magnitude images were rigidly registered to RL magnitude images to correct for subject motion between acquisitions. Next, the last RL magnitude image of the cardiac cycle was non-rigidly registered using Elastix[11] to the subject's high resolution T1-weighted image (RL magnitude images were used for the non-rigid registration, as these images showed virtually no artefacts at the end of the cardiac cycle, where image contrast between grey matter and white matter was optimal). Finally, all images were transformed to the T1-weighted image using the non-rigid registration parameters obtained from the registration of the RL image to the T1-weighted image. The magnitude and phase images were combined to form complex images before transformation to the T1-weighted image space to prevent interpolation errors near phase jumps.

2.2.3 Brain Tissue Selection

A brain tissue mask free of large blood vessels, CSF and artefacts must be used to obtain a volumetric strain map which reflects only changes induced by the swelling of the microvasculature embedded in the tissue. A brain tissue mask without the large blood vessels was created by using the Computational Anatomy Toolbox (Jena University Hospital, Departments of Psychiatry and Neurology) extension for SPM12 (Wellcome Trust Centre for Neuroimaging, University College London). The software yields CSF, grey and white matter probability maps from the T1-weighted image which were used to segment the T1-weighted image into CSF, grey and white matter tissue. The large intracranial blood vessels were associated with high intensities in the T1-weighted image, and were therefore incorrectly marked as grey or white matter by SPM12. These large blood vessels were removed from the grey and white matter probability masks using morphological area opening. Voxels in the grey and white matter tissue masks with a probability less than 0.95, or a CSF probability greater than zero (as determined by SPM12) were subsequently removed.

2.2.4 Artefact Removal

Physiological motion that is not synchronized with the triggering device, leads to an inter-shot phase instability and thus image artefacts. The sensitivity to such motion increases with increasing delay between motion-encoding and –decoding, and is, thus, maximal at the end of the cardiac cycle. As subjects have most freedom to move in the FH direction, while breathing causes a roll over the AP-axis[12] (mimicking FH motion in the frontal areas of the brain), these artefacts in the DENSE images are most extreme in the FH acquisitions[3,13]). These artefacts were typically characterised in the magnitude images by a rapidly decaying image intensity throughout the latter half of the cardiac cycle (see Figure 6). This characteristic was used to be remove the artefacts from the brain tissue masks used for the volumetric strain analysis. The spatial location of the artefacts was different in each gradient polarity image, an observation which we exploited to maximise the brain region available for the analysis. The artefacts were detected and removed from the whole brain tissue mask as follows.

First, an estimate of the DENSE signal-to-noise ratio (SNR) for each gradient polarity was created by dividing the magnitude image from the end of the cardiac cycle (when the artefacts were most prominent) by the temporal standard deviation as defined in Eqn 1,

$$\mathrm{SNR}[i,j,k] = \frac{\mathrm{Mag}[i,j,k,n]}{\sqrt{\frac{\sum_{t=1}^{n}(\mathrm{Mag}[i,j,k,t] - \frac{1}{n}\sum_{t=1}^{n}\mathrm{Mag}[i,j,k,t])^2}{n-1}}} \quad \text{Eqn 1.}$$

where *i,j,k* are image coordinates and *t=1* represents the first of *n* acquired cardiac phases. Secondly, the estimated SNR map was thresholded to create a mask free of artefacts. A threshold value of five was empirically determined to be satisfactory for this purpose. Finally, the artefact-free tissue mask was combined with the grey and white matter tissue masks using logical conjunction.

2.2.5 Volumetric Strain Calculation

Volumetric strain maps were created as follows. First, raw phase images were extracted from the registered complex images. Second, the raw phase images were converted to displacement maps by multiplying the phase image by twice the Denc value (since the analysis was performed separately for each gradient polarity, and the Denc parameter reflects the maximum displacement which does not induce a phase wrap in the subtracted phase images, see Table 1). Third, 1D strains were computed as the gradient of the RL, AP, and FH displacement maps in the RL, AP and FH direction, respectively. Wraps in the resulting 1D strain maps (i.e. phase wraps in the displacement maps that are propagated to the 1D

strain map due to the derivative operation) were spatially unwrapped under the assumption of small strains (difference in displacement between neighbouring voxels being smaller than the tag spacing). Finally, volumetric strain maps were obtained as the sum of the three 1D strains (which represents the divergence of the displacement vector field) within the 'cleaned' grey and white matter tissue masks separately. Absolute volumetric strain values greater that 1% for over half the cardiac cycle were attributed to contributions from partial-volumed CSF, remnant artefacts or large blood vessels in the tissue masks and were thus removed.

Grey and white matter volumetric strain curves were created by calculating the mean value within the volumetric strain map at each acquired cardiac phase. The volumetric strain curves obtained from the separate analysis of both gradient polarities were combined by first negating the strain curve derived from the negative gradient polarity followed by point-wise averaging. A mean, whole brain volumetric strain curve was subsequently constructed by summing the grey and white matter strain curves, weighted by the ratio of their respective tissue volumes to the whole brain tissue volume (obtained from SPM12).

2.2.6 Measurement Reference Adjustment

The measurement reference was adjusted to reflect tissue expansion similar to that obtained from other measurements triggered using a vectorcardiographic signal[3]. This was necessary because DENSE is a measure of relative displacement accruing from the time of encoding[14], and the signal from the POx utilised in this study is delayed relative to the vectorcardiogram (VCG). The minima of the whole brain volumetric strain curves obtained in this study were therefore set to zero and the curves were shifted to start at this beginning of the physiological cardiac cycle (close to the R-wave). Grey and white matter strain curves were also shifted temporally by the same amount.

2.2.7 CSF Stroke Volume Analysis

The oscillating volumetric flow of CSF at the C2-C3 level was analysed as follows. A region of interest (ROI) was created using the magnitude and phase image for guidance. Phase wraps in the velocity map within the ROI were rare and were corrected through temporal unwrapping, if present. The temporal average of the velocity map was set to zero. CSF volumetric flow was then computed as the product of the average velocity within the ROI and its area. The time integral of volumetric flow curve was calculated to obtain the CSF volume changes over the cardiac cycle. Each subject's CSF volume change curve was shifted by the same temporal offset as their respective whole brain volumetric strain curve. CSF stroke volume was defined as the peak-to-peak value of the CSF volume change curve.

2.2.8. Exploring intracranial volume dynamics

2.2.8.1 Volume change of intracranial tissue including grey and white matter differences

To investigate the intracranial tissue volume dynamics, the whole brain, grey and white matter volumetric strain curves were converted to volume changes using their respective total volume (derived from SPM). To explore physiological differences between grey and white matter tissue, the ratio of the peak grey and white matter volumetric strain curves was calculated. The time-to-peak of the volumetric strain curves was also determined.

2.2.8.2 Volume change of large intracranial vessels

A constant intracranial volume, as per the Monro-Kellie doctrine, was assumed for every phase of the cardiac cycle. The volume change of the large, intracranial vessels (summed volumes of the arterial and venous extracerebral vasculature) could then be derived from the brain and CSF volumes as defined in Eqn 2,

$$\Delta AV(t) + \Delta VV(t) = \Delta CSFV(t) - \Delta BV(t) + \Delta BSV(t) + \Delta ICV(t) \qquad 1 \leq t \leq n \qquad \text{Eqn 2.}$$

where ΔAV + ΔVV is the net volume change of the extracerebral (but intracranial) arterial and venous blood vessels. ΔCSFV and ΔBV are the CSF and brain tissue components within the cranium respectively, all at one of *n* possible frames. ΔBSV is the volume change of the brain stem displaced into the spinal canal, which was found to be negligible compared to the other components (data not shown), and thus ignored. ΔICV represents the cardiac-induced volume change of the cranial vault, which is zero (Monro-Kellie).

2.2.9 Statistics

Agreement of peak-to-peak whole brain, grey and white matter volumetric strain values from both scan sessions was assessed using Bland-Altman plots. Student's t-test was used to assess differences in the peak and time-to-peak volumetric strain values of the grey and white matter tissue. A linear regression was used to assess the relationship between cardiac-induced CSF and whole brain volume changes.

3. Results

DENSE and CSF flow measurements and analyses for all subjects were successfully completed. Figure 1 shows example images of displacement and strain maps obtained from one subject. The observed laterally directed motion of the brain tissue arises from the use of the POx for cardiac gating and reflects tissue relaxation following the peak systolic pulse. As with previous studies[3,6,15], larger displacements were found in the FH direction in comparison with the RL and AP directions, and typically occurred below the cerebellar tentorium. Despite the relative smoothness of the displacement maps, the strain maps were noticeably noisier in appearance.

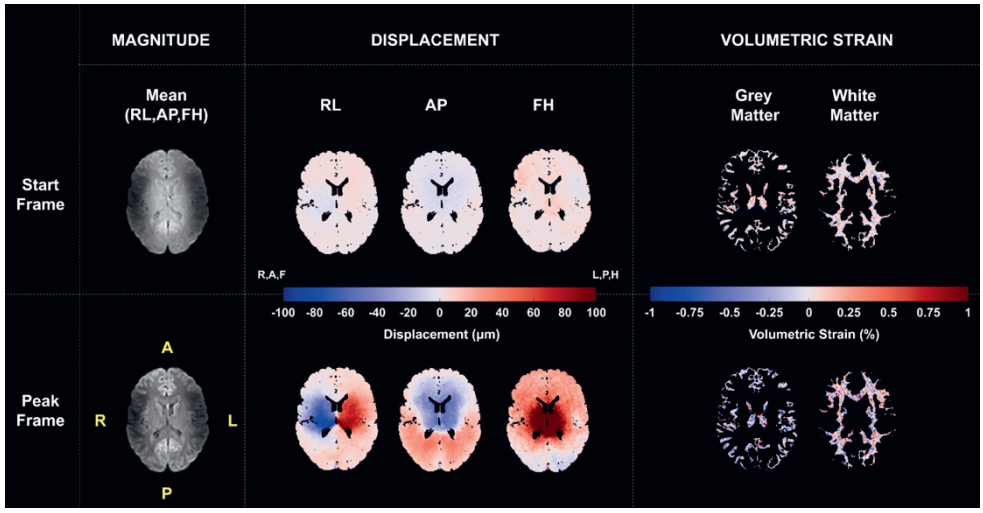

Figure 1. Example magnitude and displacement images at the start and peak frames obtained from the retrospective DENSE acquisition triggered using a pulse oximeter. Grey and white matter volumetric strain maps are also shown. Images show displacement away from the mid-line due to the use of a pulse oximeter signal for cardiac synchronisation rather than the VCG R-wave, which yields a different reference point in the cardiac cycle for which the displacement is zero. This also results in the apparent compression observable in the strain maps.

The mean volumetric strain curves covering the entire cardiac cycle for whole brain, grey matter and white matter tissue are shown in Figure 2. The general shape of the volumetric strain curves was similar for all measurements and subjects. The mean peak volumetric strain values obtained from the first scan session were (mean ± std): $(6.4 \pm 1.7)\text{x}10^{-4}$ (whole brain), $(9.5 \pm 2.5)\text{x}10^{-4}$ (grey matter), and $(4.4 \pm 1.7)\text{x}10^{-4}$ (white matter), corresponding to peak volume changes of 0.82 ± 0.24 ml, 0.68 ± 0.20 ml and 0.24 ± 0.09 ml, respectively. The mean volumetric strain values from the first scan session were calculated using ROIs

containing (32.6 ± 8.0)% and (46.4 ± 13.5)% of the available tissue for grey and white matter, respectively. For the second scan session, the mean peak volumetric strain values were: (6.7 ± 1.6)x10^{-4} (whole brain), (9.6 ± 2.4)x10^{-4} (grey matter) and (4.1 ± 0.8)x10^{-4} (white matter), corresponding to peak volume changes of 0.86 ± 0.22 ml, 0.69 ± 0.19 ml and 0.23 ± 0.05 ml, respectively. The mean volumetric strain values from the second scan session were calculated using ROIs containing (36.4 ± 3.7)% and (52.9 ± 6.7)% of the available tissue for grey and white matter, respectively.

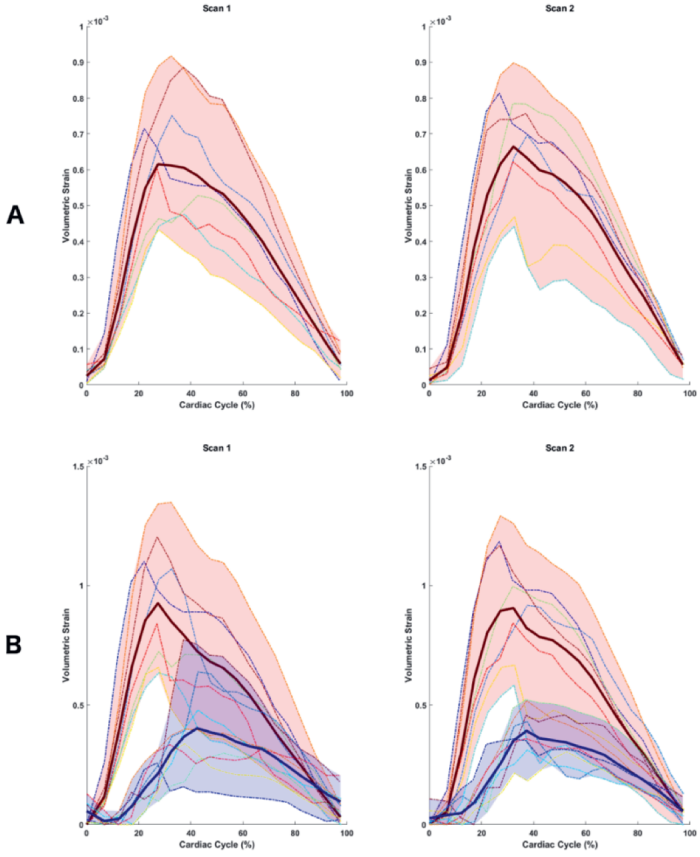

Figure 2. Whole brain (A), and grey and white matter (B) volumetric strain curves for all subjects for the first and second scan sessions, shifted to reflect brain tissue volume changes relative to the R-wave as a reference point. The strain curves show characteristic swelling of brain during systole and relaxation during diastole. In addition to differences in their peak volumetric strain values, a delay in onset of the peak volumetric strain can be seen between grey and white matter tissue (red and blue shaded regions in B, respectively). The bold line indicates the mean over all subjects. The shaded regions around the strain curves reflect subject variability, where each subject is represented by a unique, consistent colour to aid subject comparison between scan sessions.

Figure 3 shows Bland-Altman plots of the mean peak volumetric strain values for whole brain, grey and white matter tissue from both scan sessions. The mean peak grey matter volumetric strain values were observed to have a higher inter-subject variability than those of white matter.

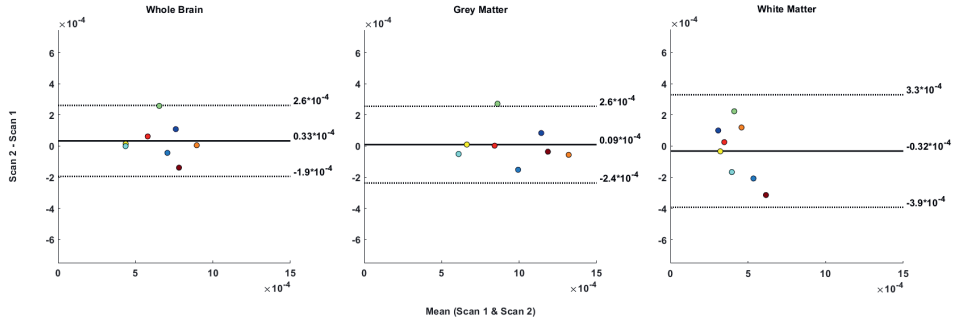

Figure 3. Bland-Altman plot showing the repeatability of whole brain, grey and white matter peak volumetric strains. The dotted lines indicate the limits of agreement (1.96 x standard deviation), whilst the bold line indicates the mean difference. Each colour represents a specific subject.

A good agreement was found between the changes in the CSF and brain volumes over the cardiac cycle for all subjects (see Table 2 and Figure 4). Linear regression of CSF vs whole brain tissue volume changes yielded a mean slope of 0.88 ± 0.23 with an R^2 value of 0.89 ± 0.07. The mean peak CSF stroke volume was 0.74 ± 0.33 ml. The derived volume changes of the large intracranial vessels were relatively limited, with a mean stroke volume of 0.33 ± 0.10 ml. The volume changes of the CSF, brain and large intracranial vessels over the entire cardiac cycle are shown in Figure 5.

Subjects	Slope	Intercept	R^2	RMSE
1	1.09	0.07	0.91	0.10
2	1.15	0.04	0.96	0.07
3	0.74	0.05	0.95	0.03
4	0.69	-0.01	0.89	0.05
5	0.60	0.00	0.88	0.04
6	0.70	0.05	0.84	0.12
7	0.86	0.04	0.75	0.08
8	1.19	0.07	0.97	0.08
(Mean ± std)	**0.88 ± 0.23**	**0.04 ± 0.03**	**0.89 ± 0.07**	**0.07 ± 0.03**

Table 2. Results of the linear regression analysis of the cardiac-induced CSF and brain tissue volume changes for each subject in this study.

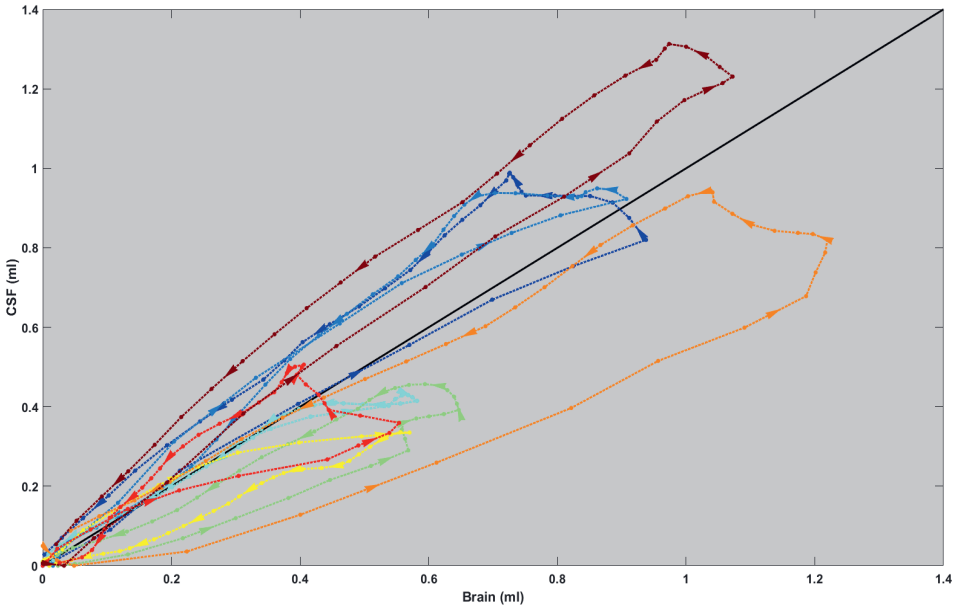

Figure 4. CSF vs brain tissue volume changes over the measured cardiac cycle. The black solid line represents y=x. Each coloured line represents a specific subject. Larger dots on the lines signify measurement points. A hysteresis effect is noticeable, with the direction indicated by the arrow heads.

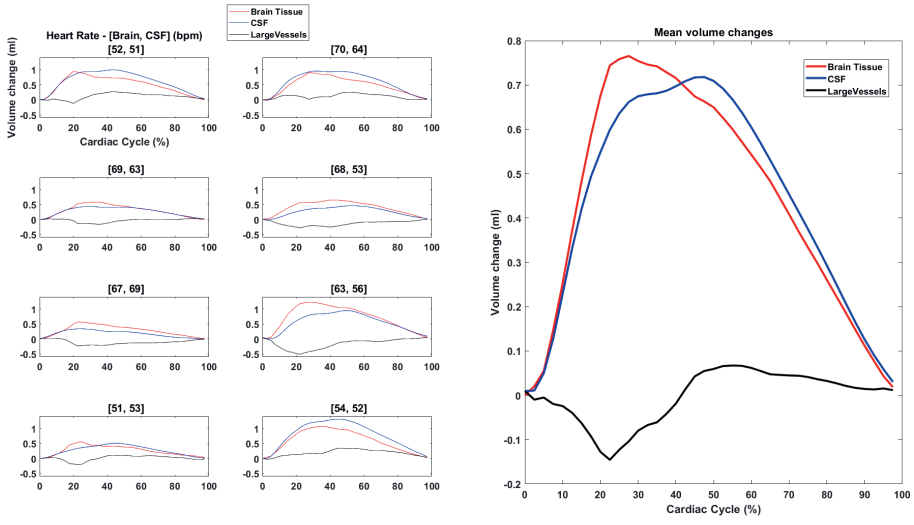

Figure 5. Brain and CSF volume changes over the cardiac cycle for all subjects. Positive values of the CSF volume change curve indicate volume displaced into the spinal canal. The estimated contribution of the large intracranial vessels (including both arteries and veins) is also shown. The mean heart rate during measurements of the brain and CSF volume changes is indicated between brackets above each figure.

The mean peak volumetric strain of grey matter was significantly higher than that of white matter, with a p-value < 0.001 in both scan sessions. The peak grey to white matter volumetric strain ratio was 2.4 ± 0.9 (first scan session) and 2.3 ± 0.4 (second scan session). After correcting for the delay between the pulse oximeter and VCG R-wave, the mean peak whole brain volumetric strain occurred at (mean ± std) (32.4 ± 6.3)% and (32.9 ± 3.1)% of the cardiac cycle for the first and second scan sessions, respectively. For both scan sessions, the time-to-peak for grey and white matter was found to be significantly different. For the first scan session, mean grey and white matter volumetric strain peaked at (28.0 ± 3.2)% and (38.6 ± 7.2)% of the cardiac cycle, respectively (p-value < 0.004). In the second scan session, the peak value for grey and white matter occurred at (31.0 ± 3.5)% and (40.4 ± 7.1)% of the cardiac cycle, respectively (p-value < 0.02).

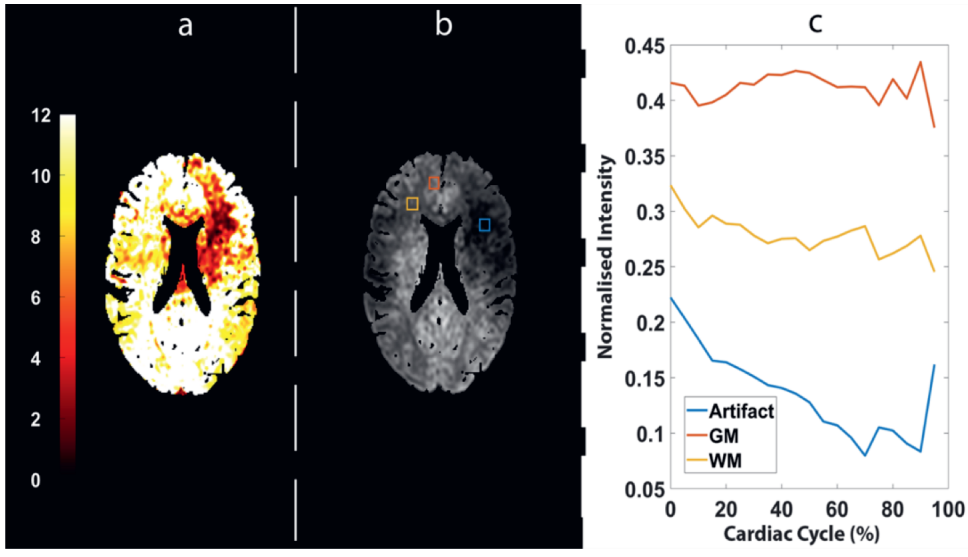

Figure 6. (a) Example image of an SNR map used to estimate the artefact locations, and (b) DENSE Feet-Head magnitude image at the end of the cardiac cycle (i.e. maximal delay between encoding and decoding gradients). The red, yellow and blue coloured boxes represent grey matter, white matter and artefact regions repsectively. These regions-of-interest were used to generate (c), mean intensity variation of grey matter, white matter and artefact areas over the cardiac cycle. Intensity values were normalised between 0 and 1 for all acquired frames of the masked slice shown in (b)

4. Discussion

We validated a faster DENSE implementation as a method for quantifying cardiac-induced brain tissue pulsations. Shorter scan durations were achieved through the use of a retrospectively-gated implementation of DENSE. The peak brain tissue volumetric strain value was found to be consistent between repeated measurements for whole brain and grey matter, and fairly consistent for white matter. Additionally, the brain tissue volume changes agreed well with independent measures of CSF volume change in the same subjects. The DENSE and CSF measurements were used to further explore intracranial volume dynamics. Relative to white matter, grey matter showed a considerably higher peak volume change that occurred considerably earlier in the cardiac cycle. Under the assumption of a fixed intracranial volume and the incompressible tissue constituents of the cranial vault, we inferred a relatively small net contribution of the large intracranial extracerebral vessels (having a diameter in the order of 1mm and more) to the CSF volume expelled towards the spinal canal during the cardiac cycle.

A retrospectively-gated implementation of DENSE was used in this study to expand on the early work on cardiac-driven pulsatile brain motion established by previous authors such as Feinberg et al.[16], Greitz et al.[17], and others more recently[3,6,18]. In comparison with our previous work utilizing DENSE to acquire cardiac-induced brain tissue motion[3], the retrospectively-gated implementation of DENSE reduced the scan duration by half whilst still achieving a similar SNR[19]. The reduced scan time not only improves its candidacy for use in clinical research, but also reduces potential subject-based motion artefacts. Although the retrospectively-gated algorithm is compatible with the use of a VCG signal for cardiac synchronisation, utilisation of the POx instead simplifies measurement setup whilst providing a stable signal, free from magnetohydrodynamic artefacts. A minor consequence of using the POx in this manner is an implied compression of brain tissue due to the peak-systolic cardiac phase used as a reference point for triggering the DENSE measurements. As shown in this study, this issue can be easily corrected in post-processing.

The Bland-Altman analysis revealed good agreement of peak brain tissue volumetric strain between measurements. We observed lower SNR at the centre of the brain due to the lower sensitivity of the receive coil array. This lower SNR, in addition to the generally lower mean peak volumetric strain values may explain the limited repeatability observed in this study for white matter. Nonetheless, the high repeatability of the peak whole brain volumetric strain, in conjunction with the high correlation to CSF volume changes, suggests that the variability in peak volumetric strain observed amongst subjects reflects physiological variation rather than measurement error. Due to the relatively long acquisition, respiration effects are averaged out, thus its impact on the variation observed in this study was limited. It should be noted that from our previous work[3], it was estimated that increasing the DENSE SNR by a

factor of ~10 allows for a voxel-wise analysis of the peak volumetric strain. In terms of SNR, this is equivalent to averaging ~100 voxels. Therefore, in this study spatial smoothing of the data was unnecessary since results were obtained from averaging over 10k voxels.

The approximately linear relationship (as obtained from the regression analysis) between CSF and brain tissue volume changes is consistent with current concepts of intracranial volume change. In order to compensate for the increased blood volume which enters the cranium from the heart during each cardiac cycle, a similar volume of CSF is flushed out into the spinal canal, thereby assisting with the maintenance of a stable intracranial pressure[20–23]. Thus, if only the average brain volume change is of interest, one might use CSF stroke volume measurements at the level of the spinal canal, which are shown to be readily available at clinical field strengths[4]. The internal validation of our method using CSF volume changes increases confidence in the volume change measurements obtained using DENSE, despite the inherent sensitivity of the volumetric strain calculation to noise.

Exploration of the volume changes in the large intracranial vessels was achievable using the results obtained from the internal validation of our method. Fundamental to the exploration of these volume changes is the notion of intracranial volume change (ICVC). Several investigators have previously calculated ICVCs by summing transcranial blood and CSF flows into and out of the cranium over the cardiac cycle. Based on this approach, average maximum ICVCs of 0.6 ± 0.1 ml[24] , 0.48 ± 0.15 ml[25] and 0.43 ± 0.12 ml[26] have been reported. Our results are complementary to these measurements as we quantified the contribution of the swelling of the vasculature embedded in the brain tissue to the CSF expelled in the spinal canal. Considering these vessels to belong by definition to the microvasculature, we estimated the swelling of the extracerebral vasculature (or intracranial 'macrovasculature') by subtracting the brain tissue volume from the CSF volume. This estimation is based on the assumption that the intracranial volume is truly rigid and does not show a volume change over the cardiac cycle. We believe that this is a valid assumption since the skull is three orders of magnitude stiffer[27] than the brain tissue[28]. Even in the soft brain tissue, only a volume change of about 1 ml is observed. However, if the estimated ICVCs in the literature are realistic (or reflect tissue and/or fluid flows through other foramina), such ICVCs have to be added to our estimated macrovascular volume pulsations. This still would yield stroke volumes of the large intracranial vessels of similar size as the stroke volume of the microvasculature, underscoring that the contribution of the microvasculature cannot be ignored. On the other hand, if the ICVC truly is negligible, our findings of limited volume change in the large intracranial (but extracerebral) blood vessels implies compression of the cortical veins and cavernous sinus. In either case, direct measurements of the blood volume changes in the extracerebral macrovascular are challenging due to the complex venous drainage system[29]. Therefore, the method of indirect estimation as performed in our study

may provide a means to gain further insights into the intracranial volume dynamics. We observed a net negative volume of the extracerebral macrovascular compartment during systole, which may reflect an initial venous compression[23,30,31] due to the rapid increase in intracranial pressure[32], before the CSF can be displaced. As such, due to the tightly coupled pressure-volume relationships between the incompressible constituents of the cranial cavity, reduced or abnormal CSF expulsion, such as that which occurs in the elderly[33] or in disorders such as Chiari I malformation[34], may be associated with altered microvascular pulsations within the brain tissue. Altered microvascular pulsations may also occur as a result of intracranial hypertension[35], hydrocephalus and age-related 'pulse wave encephalopathy'[36].

The measured differences in the mean volumetric strain value of grey and white matter tissue reflects the physiological differences between these two tissue types. Since white matter is stiffer than grey matter[37], the lower volumetric strain (or, equivalently, volume change) for the former obtained in this study may not only reflect differences in the blood volume occupying both tissue types, but also differences in tissue viscoelasticity. The vascular organization within the brain parenchyma results in grey matter being perfused before white matter, and intuitively provides an explanation for the delay observed between peak grey and white matter volumetric strain. However, given the speed of the arterial pulse wave, and the mean distance between the two tissue types, it is unlikely that this delay can be measured with the temporal resolution used in this study. Rather, a more likely explanation for the observed delay in peak swelling between grey and white matter can be surmised from the BOLD-CVR studies performed by Bhogal et al.[38], where it was suggested that grey matter is preferentially filled with blood due to its denser vascularization. Therefore, grey matter may buffer cardiac-induced blood volume changes before these are redirected to the white matter. It is unclear how the surrounding tissue stiffness properties affect the propagation of the arterial pulse wave throughout the microvasculature. One approach may be to lump tissue and vessel wall stiffness as a single parameter in biomechanical modelling[39], which is outside the scope of this work.

Our results are similar to those reported in the literature. The peak volumetric strain values obtained in this study are in agreement with previous measurements of tissue volumetric strain using prospectively-triggered DENSE[3] and PCMRI[40]. Furthermore, the peak grey to white matter volume change ratio of approximately 2.4 found in this study is similar to that obtained in other MR based methods of assessing brain tissue blood volume variations over the cardiac cycle. Viessmann et al.[41] assessed the signal fluctuations derived from double-echo EPI scans and found an approximate factor of 2 in the T2* fluctuations of grey and white matter, with the former being larger. They associated these T2* fluctuations with blood volume changes between these two tissue types. Interestingly, they also observed phase delays between different grey matter regions but do not report such a relation between grey

and white matter. Rivera-Rivera et al.[42] also investigated brain tissue blood volume differences using T2* signal fluctuations, enhanced through the use of ferumoxytol as a contrast agent and instead obtained through a spiral acquisition. As in this study, they also obtained a significant difference between grey and white matter blood volume pulsations over the cardiac cycle, however they found a slightly lower ratio of approximately 1.6. The ratio they obtained may have been limited by the model used to estimate brain volume changes. They also do not report any differences in the time to peak of grey and white matter microvascular blood volumes, which may be due to the reconstructed temporal resolution and retrospective binning used in that study. The group mean CSF stroke volume measurements achieved in our study are also similar to those obtained by other investigators using PCMRI to measure volumetric CSF flow at the C2-C3 cervical level: 0.58 ± 0.12 ml[43], 0.71 ± 0.32 ml[44], 0.77 ± 0.23 ml[45].

Cerebral small vessel disease is an age-linked, neurological disorder characterized by damage to the microvasculature and the surrounding tissue bed[46]. As such, brain tissue volumetric strain measurements, which uniquely contain joint information on both vascular and tissue function, may prove to be a useful tool for investigating early pathological changes induced by this disease, conceivably even before the vascular/neuronal damage is visible on typical CT/MR images. Moreover, cardiac pulsation is claimed to be involved in the brain's clearance system[47]. Although it is unlikely that cardiac pulsation drives a net fluid flow in the tissue, it is well conceivable that the observed tissue deformations contribute to mixing of fluids and, thus, to more effective waste transport[48,49]. In this study we observed consistency between repeated measurements of brain tissue volumetric strain, and also internal consistency of brain tissue and CSF intracranial volume exchange in accordance to the Monro-Kellie doctrine. These consistencies together strengthen the potential of this method as a biomarker of the microvascular function for investigating the ageing brain under healthy and diseased conditions. Our measurements also revealed an inter-subject variation, which is likely related to physiological differences, including inter-subject variation in intracranial pressure[35]. Future work is warranted to explore these differences to determine whether a particular physiology may be linked to age, sex and/or risk factors for disorders such as stroke or cerebral small vessel disease. Additionally, given the existing inter-subject variation in controls, future studies comparing matched controls with patients or elderly are needed to investigate the power of this technique for detecting disease or changes with age (where a reduction in tissue strain is expected given CSF stroke volume reduction with age[50]).

Several biomechanical phenomena underlie the volumetric strain values reported in this study: the change in blood volume of the microvasculature within the parenchyma[51], the net pulsatile pressure acting on the parenchyma[52] and the parenchyma's viscoelastic properties[53]. As previously discussed, our volumetric strain measurements may provide early insights into diseases which alter those underlying phenomena. Moreover, in some cases, minor

differences in cardiac-induced pulsatile pressure may be assumed throughout the brain parenchyma[54]. Under that assumption, the parenchymal viscoelastic properties can be approximated using MR elastography reconstructions derived from displacement measurements such as those acquired in this study[55,56]. This would in principle allow the disentanglement of the tissue volume change from its viscoelastic properties, allowing separate quantification of changes to these specific biomechanical phenomena due to age or disease. Future work is also warranted to explore how cardiac-induced brain tissue volumetric strain measurements depend on the actual physiology during the measurements such as heart rate and respiration rate, which may vary based on the level of anxiety of the patient in the scanner.

Due to the sensitivity required to accurately measure brain tissue displacement, which would introduce multiple phase-wraps of CSF motion at the C2-C3 level, simultaneous measurements of brain tissue and CSF motion from the DENSE images were not possible. In some subjects we noted a discrepancy in the average heart-rate between DENSE and CSF measurements (see Fig 5). CSF and arterial flow waveforms are known to be a function of heart rate[57,58]. The heart rate discrepancy may thus restrict interpretations of the brain tissue and CSF intracranial volume imbalance.

As with other measurements of brain tissue using DENSE[3,6], some images contained artefacts which may be related to the SENSE acceleration, intra-voxel dephasing, and subject motion including respiration. Although these artefact regions were excluded from the analysis, their removal may have hampered measurement repeatability by the exclusion of volumetric strain data from key brain regions. The removal of these artefacts, and an increase in measurement SNR would further allow brain region volumetric strain analyses using smaller ROIs, and is the focus of future work. A further limitation of this study is the use of registration software to correct for EPI distortions, which could be improved through the use of an acquired B0-field map.

5. Conclusion

Cardiac-induced brain tissue pulsatility has consistent inter-subject peak values in repeated measurements of healthy subjects. Furthermore, it is strongly correlated to CSF volume changes measured at the C2-C3 level. The successful internal validation of measured brain volume changes to CSF displaced into the spinal canal suggests that due to venous compression, the extracerebral macrovasculature offers a relatively minor contribution to CSF intracranial dynamics over the cardiac cycle. The consistency between repeated brain tissue volumetric strain measurements, and internal validation to CSF measurements strengthens the potential of brain tissue volumetric strain as a tool for investigating the ageing brain in normal or diseased states.

References

1. Sweetman B, Linninger AA. Cerebrospinal fluid flow dynamics in the central nervous system. *Ann Biomed Eng*. 2011;39(1):484-496. doi:10.1007/s10439-010-0141-0
2. Aletras AH, Ding S, Balaban RS, Wen H. DENSE: Displacement Encoding with Stimulated Echoes in Cardiac Functional MRI. *Journal of Magnetic Resonance*. 1999;137(1):247-252. doi:10.1006/jmre.1998.1676
3. Adams AL, Kuijf HJ, Viergever MA, Luijten PR, Zwanenburg JJM. Quantifying cardiac-induced brain tissue expansion using DENSE. *NMR Biomed*. 2019;32(2):1-13. doi:10.1002/nbm.4050
4. Balédent O, Henry-Feugeas MC, Idy-Peretti I. Cerebrospinal fluid dynamics and relation with blood flow: a magnetic resonance study with semiautomated cerebrospinal fluid segmentation. *Invest Radiol*. 2001;36(7):368-377. doi:10.1097/00004424-200107000-00003
5. Wåhlin A, Ambarki K, Hauksson J, Birgander R, Malm J, Eklund A. Phase contrast MRI quantification of pulsatile volumes of brain arteries, veins, and cerebrospinal fluids compartments: Repeatability and physiological interactions. *Journal of Magnetic Resonance Imaging*. 2012;35(5):1055-1062. doi:10.1002/jmri.23527
6. Soellinger M, Rutz AK, Kozerke S, Boesiger P. 3D cine displacement-encoded MRI of pulsatile brain motion. *Magn Reson Med*. 2009;61(1):153-162. doi:10.1002/mrm.21802
7. Enzmann DR, Pelc NJ. Cerebrospinal fluid flow measured by phase-contrast cine MR. *AJNR Am J Neuroradiol*. 1993;14(6):1301-1307. http://www.ncbi.nlm.nih.gov/pubmed/8279323
8. Greitz D, Wirestam R, Franck A, Nordell B, Thomsen C, Stahlberg F. Pulsatile brain movement and associated hydrodynamics studied by magnetic resonance phase imaging. *Neuroradiology*. 1992;34(5):370-380. doi:10.1007/BF00596493
9. Adams AL, Luijten PR, Zwanenburg JJM. An SNR analysis of DENSE at 7T vs 3T for the measurement of whole brain tissue pulsatility. In: *Proceedings of the Joint Annual Meeting ISMRM-ESMRMB*. ; 2018.
10. Stuber M, Spiegel MA, Fischer SE, et al. Single breath-hold slice-following CSPAMM myocardial tagging. *Magnetic Resonance Materials in Physics, Biology and Medicine*. 1999;9(1-2):85-91. doi:10.1016/S1352-8661(99)00049-6
11. Klein S, Staring M, Murphy K, Viergever MA, Pluim J. elastix: A Toolbox for Intensity-Based Medical Image Registration. *IEEE Trans Med Imaging*. 2010;29(1):196-205. doi:10.1109/TMI.2009.2035616
12. Sloots JJ, Adams AL, Luijten PR, Biessels GJ, Zwanenburg JJM. Unraveling Cardiac and Respiratory Contributions to Brain Tissue Motion using Single Shot 2D DENSE at 7T MRI. In: *Proceedings of the Joint Annual Meeting ISMRM-ESMRMB*. ; 2018.
13. Soellinger M, Rutz AK, Kozerke S, Boesiger P. 3D cine displacement-encoded MRI of pulsatile brain motion. *Magn Reson Med*. 2009;61(1):153-162. doi:10.1002/mrm.21802
14. Aletras AH, Ding S, Balaban RS, Wen H. DENSE: Displacement Encoding with Stimulated Echoes in Cardiac Functional MRI. *Journal of Magnetic Resonance*. 1999;137(1):247-252. doi:10.1006/jmre.1998.1676
15. Pahlavian SH, Oshinski J, Zhong X, Loth F, Amini R. Regional Quantification of Brain Tissue Strain Using Displacement-Encoding With Stimulated Echoes Magnetic Resonance Imaging. *J Biomech Eng*. 2018;140(8):081010. doi:10.1115/1.4040227
16. Feinberg DA, Mark AS. Human brain motion and cerebrospinal fluid circulation demonstrated with MR velocity imaging. *Radiology*. 1987;163(3):793-799. doi:10.1148/radiology.163.3.3575734
17. Greitz D, Wirestam R, Franck A, Nordell B, Thomsen C, Stahlberg F. Pulsatile brain movement and associated hydrodynamics studied by magnetic resonance phase imaging. *Neuroradiology*. 1992;34(5):370-380. doi:10.1007/BF00596493
18. Pahlavian SH, Oshinski J, Zhong X, Loth F, Amini R. Regional Quantification of Brain Tissue Strain Using Displacement-Encoding With Stimulated Echoes Magnetic Resonance Imaging. *J Biomech Eng*. 2018;140(8):081010. doi:10.1115/1.4040227

19. Adams AL, Sloots JJ, Luijten PR, Zwanenburg JJM. SNR analysis of retrospectively gated DENSE at 7T for the measurement of brain tissue pulsatility. In: *Proceedings of the Joint Annual Meeting ISMRM-ESMRMB*. ; 2018.
20. Alperin N, Vikingstad EM, Gomez-Anson B, Levin DN. Hemodynamically independent analysis of cerebrospinal fluid and brain motion observed with dynamic phase contrast MRI. *Magn Reson Med*. 1996;35(5):741-754. doi:10.1002/mrm.1910350516
21. Balédent O, Henry-Feugeas MC, Idy-Peretti I. Cerebrospinal fluid dynamics and relation with blood flow: a magnetic resonance study with semiautomated cerebrospinal fluid segmentation. *Invest Radiol*. 2001;36(7):368-377. doi:10.1097/00004424-200107000-00003
22. Capel C, Baroncini M, Gondry-Jouet C, et al. Cerebrospinal Fluid and Cerebral Blood Flows in Idiopathic Intracranial Hypertension. In: *Acta Neurochirurgica, Supplementum*. Vol 126. ; 2018:237-241. doi:10.1007/978-3-319-65798-1_48
23. Enzmann DR, Pelc NJ. Cerebrospinal fluid flow measured by phase-contrast cine MR. *AJNR Am J Neuroradiol*. 1993;14(6):1301-1307.
24. Balédent O, Fin L, Khuoy L, et al. Brain hydrodynamics study by phase-contrast magnetic resonance imaging and transcranial color doppler. *Journal of Magnetic Resonance Imaging*. 2006;24(5):995-1004. doi:10.1002/jmri.20722
25. Alperin N, Lee SH, Sivaramakrishnan A, Hushek SG. Quantifying the effect of posture on intracranial physiology in humans by MRI flow studies. *Journal of Magnetic Resonance Imaging*. 2005;22(5):591-596. doi:10.1002/jmri.20427
26. Tsai YH, Chen HC, Tung H, et al. Noninvasive assessment of intracranial elastance and pressure in spontaneous intracranial hypotension by MRI. *Journal of Magnetic Resonance Imaging*. Published online 2018:1-9. doi:10.1002/jmri.25976
27. Peterson J, Dechow PC. Material properties of the human cranial vault and zygoma. *Anatomical Record - Part A Discoveries in Molecular, Cellular, and Evolutionary Biology*. 2003;274(1):785-797. doi:10.1002/ar.a.10096
28. Jin X, Zhu F, Mao H, Shen M, Yang KH. A comprehensive experimental study on material properties of human brain tissue. *J Biomech*. 2013;46(16):2795-2801. doi:10.1016/j.jbiomech.2013.09.001
29. Schaller B. Physiology of cerebral venous blood flow: from experimental data in animals to normal function in humans. *Brain Res Rev*. 2004;46(3):243-260. doi:10.1016/j.brainresrev.2004.04.005
30. Greitz D. Radiological Assessment of Hydrocephalus: New Theories and Implications for Therapy. *Neuroradiol J*. 2006;19(4):475-495. doi:10.1177/197140090601900407
31. DE Simone R, Ranieri A, Bonavita V. Starling resistors, autoregulation of cerebral perfusion and the pathogenesis of idiopathic intracranial hypertension. *Panminerva Med*. 2017;59(1):76-89. doi:10.23736/S0031-0808.16.03248-1
32. Alperin N, Mazda M, Lichtor T, Lee SH. From Cerebrospinal Fluid Pulsation to Noninvasive Intracranial Compliance and Pressure Measured by MRI Flow Studies. *Curr Med Imaging Rev*. 2006;2(1):117-129. doi:10.2174/157340506775541622
33. Stoquart-ElSankari S, Balédent O, Gondry-Jouet C, Makki M, Godefroy O, Meyer ME. Aging Effects on Cerebral Blood and Cerebrospinal Fluid Flows. *Journal of Cerebral Blood Flow & Metabolism*. 2007;27(9):1563-1572. doi:10.1038/sj.jcbfm.9600462
34. Haughton VM, Korosec FR, Medow JE, Dolar MT, Iskandar BJ. Peak systolic and diastolic CSF velocity in the foramen magnum in adult patients with Chiari I malformations and in normal control participants. *American Journal of Neuroradiology*. 2003;24(2):169-176.
35. Saindane AM, Qiu D, Oshinski JN, et al. Noninvasive Assessment of Intracranial Pressure Status in Idiopathic Intracranial Hypertension Using Displacement Encoding with Stimulated Echoes (DENSE) MRI: A Prospective Patient Study with Contemporaneous CSF Pressure Correlation. *American Journal of Neuroradiology*. 2018;39(2):311-316. doi:10.3174/ajnr.A5486

36. Cecile Henry-Feugeas M, Koskas P. Cerebral Vascular Aging: Extending the Concept of Pulse Wave Encephalopathy Through Capillaries to the Cerebral Veins. *Current Aging Sciencee*. 2012;5(2):157-167. doi:10.2174/1874609811205020157
37. Jin X, Zhu F, Mao H, Shen M, Yang KH. A comprehensive experimental study on material properties of human brain tissue. *J Biomech*. 2013;46(16):2795-2801. doi:10.1016/j.jbiomech.2013.09.001
38. Bhogal AA, Philippens MEP, Siero JCW, et al. Examining the regional and cerebral depth-dependent BOLD cerebrovascular reactivity response at 7T. *Neuroimage*. 2015;114:239-248. doi:10.1016/j.neuroimage.2015.04.014
39. Ambarki K, Baledent O, Kongolo G, Bouzerar R, Fall S, Meyer ME. A new lumped-parameter model of cerebrospinal hydrodynamics during the cardiac cycle in healthy volunteers. *IEEE Trans Biomed Eng*. 2007;54(3):483-491. doi:10.1109/TBME.2006.890492
40. Hirsch S, Klatt D, Freimann F, Scheel M, Braun J, Sack I. In vivo measurement of volumetric strain in the human brain induced by arterial pulsation and harmonic waves. *Magn Reson Med*. 2013;70(3):671-683. doi:10.1002/mrm.24499
41. Viessmann O, Möller HE, Jezzard P. Cardiac cycle-induced EPI time series fluctuations in the brain: Their temporal shifts, inflow effects and T2∗fluctuations. *Neuroimage*. 2017;162(August):93-105. doi:10.1016/j.neuroimage.2017.08.061
42. Rivera-Rivera LA, Johnson KM, Turski PA, Wieben O, Schubert T. Measurement of microvascular cerebral blood volume changes over the cardiac cycle with ferumoxytol-enhanced T 2 * MRI. *Magn Reson Med*. 2019;(July 2018):1-11. doi:10.1002/mrm.27670
43. Balédent O. Imaging of the cerebrospinal fluid circulation. In: Rigamonti D, ed. *Adult Hydrocephalus*. Cambridge University Press; 2014:121-138. doi:10.1017/CBO9781139382816.013
44. Wåhlin A, Ambarki K, Birgander R, Malm J, Eklund A. Intracranial pulsatility is associated with regional brain volume in elderly individuals. *Neurobiol Aging*. 2014;35(2):365-372. doi:10.1016/j.neurobiolaging.2013.08.026
45. Wåhlin A, Ambarki K, Hauksson J, Birgander R, Malm J, Eklund A. Phase contrast MRI quantification of pulsatile volumes of brain arteries, veins, and cerebrospinal fluids compartments: Repeatability and physiological interactions. *Journal of Magnetic Resonance Imaging*. 2012;35(5):1055-1062. doi:10.1002/jmri.23527
46. Shi Y, Wardlaw JM. Update on cerebral small vessel disease: a dynamic whole-brain disease. *Bmj*. 2016;1(3):83-92. doi:10.1136/svn-2016-000035
47. Iliff JJ, Wang M, Zeppenfeld DM, et al. Cerebral Arterial Pulsation Drives Paravascular CSF-Interstitial Fluid Exchange in the Murine Brain. *Journal of Neuroscience*. 2013;33(46):18190-18199. doi:10.1523/JNEUROSCI.1592-13.2013
48. Asgari M, De Zélicourt D, Kurtcuoglu V. Glymphatic solute transport does not require bulk flow. *Sci Rep*. 2016;6:1-11. doi:10.1038/srep38635
49. Bedussi B, Almasian M, de Vos J, VanBavel E, Bakker ENTP. Paravascular spaces at the brain surface: Low resistance pathways for cerebrospinal fluid flow. *Journal of Cerebral Blood Flow and Metabolism*. 2018;38(4):719-726. doi:10.1177/0271678X17737984
50. Stoquart-ElSankari S, Balédent O, Gondry-Jouet C, Makki M, Godefroy O, Meyer ME. Aging Effects on Cerebral Blood and Cerebrospinal Fluid Flows. *Journal of Cerebral Blood Flow & Metabolism*. 2007;27(9):1563-1572. doi:10.1038/sj.jcbfm.9600462
51. Sweetman B, Linninger AA. Cerebrospinal fluid flow dynamics in the central nervous system. *Ann Biomed Eng*. 2011;39(1):484-496. doi:10.1007/s10439-010-0141-0
52. Mousavi SR, Fehlner A, Streitberger KJ, Braun J, Samani A, Sack I. Measurement of in vivo cerebral volumetric strain induced by the Valsalva maneuver. *J Biomech*. 2014;47(7):1652-1657. doi:10.1016/j.jbiomech.2014.02.038
53. Hirsch S, Klatt D, Freimann F, Scheel M, Braun J, Sack I. In vivo measurement of volumetric strain in the human brain induced by arterial pulsation and harmonic waves. *Magn Reson Med*. 2013;70(3):671-683. doi:10.1002/mrm.24499

54. Eide PK. Comparison of simultaneous continuous intracranial pressure (ICP) signals from ICP sensors placed within the brain parenchyma and the epidural space. *Med Eng Phys*. 2008;30(1):34-40. doi:10.1016/j.medengphy.2007.01.005
55. Weaver JB, Pattison AJ, McGarry MD, et al. Brain mechanical property measurement using MRE with intrinsic activation. *Phys Med Biol*. 2012;57(22):7275-7287. doi:10.1088/0031-9155/57/22/7275
56. Zorgani A, Souchon R, Dinh AH, et al. Brain palpation from physiological vibrations using MRI. *Proceedings of the National Academy of Sciences*. 2015;112(42):12917-12921. doi:10.1073/pnas.1509895112
57. Strik C, Klose U, Erb M, Strik H, Grodd W. Intracranial oscillations of cerebrospinal fluid and blood flows: Analysis with magnetic resonance imaging. *Journal of Magnetic Resonance Imaging*. 2002;15(3):251-258. doi:10.1002/jmri.10084
58. Daouk J, Bouzerar R, Baledent O. Heart rate and respiration influence on macroscopic blood and CSF flows. *Acta radiol*. 2017;58(8):977-982. doi:10.1177/0284185116676655

Chapter 4 (Part I)

Measurements of cardiac-induced brain tissue pulsations in patients with white matter lesions

This chapter is based on the following research article currently in submission to the Journal of Magnetic Resonance Imaging: Adams, A. L., Rots, M., de Borst, G. J., & Zwanenburg, J. J. M. (*2023*). *Measurements of Cardiac-Induced Brain Tissue Pulsations in Patients with White Matter Lesions*.

Abstract

Background
Volumetric strain is a useful metric for quantifying cardiac-induced brain tissue pulsations as it provides an indirect assessment of microvascular physiology, thereby enabling potential investigations into cerebral small vessel disease. However, proof-of-concept in patients with vascular disease is lacking.

Method
In this exploratory study, volumetric strain parameters in patients with internal carotid artery stenosis were compared to those in a young, healthy control group. Volumetric strain peak and time-to-peak observations were made for the whole brain (WB), grey matter (GM), normal appearing white matter (NAWM), hyper-intense white matter (WMH) and regions at risk to development of WMH (WMH_R).

Results
For the intra-group analyses, significantly higher peak volumetric strains were found in the GM compared to the NAWM regions of interest (ROIs) for both patients ($p=0.020$) and controls ($p=0.003$).

For the inter-group analyses, the patient group demonstrated significantly earlier time to peak strain in the NAWM ($p=0.019$) and WMH ($p=0.002$) ROIs when compared to the corresponding regions in controls. The patient group also showed significantly later time to peak strain in the GM ($p=0.001$) and WB ($p=0.029$) ROIs. The group mean strain waveforms in the WMH and WMH_R ROIs were qualitatively observed to show an altered waveform in comparison to their NAWM counterparts. Additionally, a larger heterogeneity in the strain maps was also observed in the patient group.

Conclusion
We observed altered volumetric strain patterns in the patient cohort which are interpreted to arising from a stiffer vasculature in this group. These results are consistent with the pulse wave encephalopathy hypothesis. This study further demonstrates the potential of brain tissue volumetric strain measurements as a tool to elucidate changes to the brain microvasculature which arise due to disease or age.

1. Introduction

The brain exhibits small, local brain tissue deformations due to the cardiac-induced changes in the blood volume found within the tissue microvasculature. Damage to the tissue microvasculature may lead to the formation of white matter lesions and other lesions typical for cerebral small vessel disease (cSVD), which have cognitive and related social consequences[1]. Some damage to the microvasculature is naturally expected with age under the pulse wave encephalopathy (PWE) hypothesis and general trend of arteriosclerosis in the aging population[2,3]. In brief, the PWE hypothesis describes a mechanism by which the microvasculature is damaged through the transfer of a higher pulsatile energy deeper into the microvasculature due to reduced compliance in upstream arteries. Thus, neuroimaging methods which are sensitized to measure brain tissue pulsations may provide insight into one of the major drivers of microvascular damage, and in the long run yield quantitative diagnostic or prognostic tools for diseases arising from damaged microvasculature.

However, measuring brain tissue motion in-vivo is currently challenging, particularly due to the amplitudes of tissue displacement associated with microvascular pulsations. The pulsatile brain tissue motion can be quantified non-invasively with MRI-based methods[4–6]. MRI-based methods can provide whole brain coverage and estimations of cardiac-induced displacements that are orders of magnitude smaller than the voxel size of the underlying MRI images. Recently, the MRI-based technique Displacement Encoding with Stimulated Echoes (DENSE) was developed for investigating the brain tissue microvasculature[6,7]. Volumetric strain can be derived from displacement measurements of brain tissue motion, and provides an estimate of the volume change in the brain tissue as a result of cardiac output. It thus provides an indirect window into the physiological functioning of the smaller vessels penetrating the brain tissue. Preliminary results using this approach are encouraging, permitting localisation and quantification of the cardiac-induced blood volume changes associated with the microvascular pulsations.

Although the first experiences with this technique are promising, and suggest that DENSE measurements of brain tissue pulsation can inform on the microvascular function, proof-of-concept in patients with vascular disease is lacking. Given the sensitivity of DENSE measurements to motion artifacts, the inherently low image SNR[8], and the noise-sensitive computation necessary to calculate the volumetric strain metric, application in patients might be challenging, and it is uncertain whether the method is sufficiently sensitive to detect differences between patients and controls. In this exploratory study, we aimed to evaluate the potential usefulness of cardiac-induced volumetric strain as a tool for investigating microvascular function in patients with cerebrovascular disease. To this end, we compared volumetric strain parameters in elderly patients with internal carotid artery stenosis to those in a young, healthy control group. The comparison included whole brain (WB), grey matter

(GM), normal appearing white matter (NAWM), as well as regions with hyper-intense white matter (WMH).

2. Method

2.1 Measurements

Informed consent was obtained from 7 elderly subjects (2 females, 73 ± 5 years) and 8 young subjects (3 females, mean age: 27 ± 6 years) to partake in this study, which was approved by the Ethical Review Board of our institution. The data gathered for the elderly subjects were acquired as part of a separate clinical trial, and data for the young subjects were previously collected[6]. Research conducted on all participants was performed in accordance with the Declaration of Helsinki. While the young subjects had no known history of cardiovascular or cerebral diseases, the elderly subjects suffered from ≥70% stenosis of either the left or right carotid artery, and were scheduled to undergo a carotid artery endarterectomy shortly after imaging. These two subject populations are henceforth denoted as the healthy controls and the patient group, respectively.

For all subjects, 4D (3D + time) retrospectively-gated DENSE measurements of brain tissue were acquired with a 7T MR scanner (Philips Healthcare, Best, The Netherlands) using a 2-channel volume transmit and 32-channel receive head coil (Nova Medical, Houston, United States). The measurements were sensitized to encode displacements in the right-left, anterior-posterior and feet-head directions, and were acquired in two dynamics with opposing polarity[6,7]. The DENSE measurements were synchronised to the cardiac cycle using a pulse oximeter attached to the index finger of the subjects. A 3D T1-weighted FFE scan was also acquired during the same scan session for registration and segmentation of brain tissue.
Additionally, 3D FLAIR images of the patient group were acquired at 3T MR (Philips Healthcare, Best, The Netherlands). These FLAIR images were used for segmentation of WMH.

All acquisition parameters are summarised in Table 1.

2.2 Measurements analysis

2.2.1 Strain computation

As previously described[6], measurement analysis commenced with the co-registration of the three orthogonally sensitized DENSE images to each other, and then to the T1-weighted image space. The raw phase data were converted to displacement maps representing Eulerian brain tissue displacement using the appropriate encoding value (Table 1). Artifacts, which typically occurred towards the end of the cardiac cycle, were removed as previously described.

Parameter	DENSE	T1-weighted FFE	FLAIR
Denc[1] (mm) (FH/AP/RL)	0.35*/0.175/0.175	--	--
Acquired resolution (mm) (FHxAPxRL)	2.2 x 2.2 x 2.2	1.0 x 1.0 x 1.0	1.0 x 1.0 x 1.0
FOV (mm) (FHxAPxRL)	250x250x190	300x248x190	250 x 250 x 180
TR (ms)	35/30/35 (FH/AP/RL)	4	5000
TE (ms)	8.7	2	252.7
EPI factor	15	--	182
TFE factor	2	600	--
Number of Averages	1	1	2
Readout/phase BW (Hz/pixel)	2342/92	405/--	1240
Inversion delay (ms)	--	1235	1700
SENSE (APxRL)	1.9 X 2.5	2 X 2	2.4 x 2
Flip angle (deg)	Variable[3]	5	90
Cardiac synchronization[3]	Retrospective	--	--
Phases/cardiac cycle	20	--	--
Scan duration (min:s)[4]	2:24	0:48	6:15
Field Strength (T)	7	7	3

Table 1. Scan acquisition parameters.
1. Denc: The absolute displacement which induces a phase wrap in the subtracted phase images, analogous to the Venc parameter in velocity encoded phase contrast imaging. *For 4 subjects in the patient group, a FH encoding value of 0.54 was used to suppress phase wraps in the acquired measurements.
2. The flip angles were varied over the cardiac cycle to create a stable signal[9], assuming a T1 of 1100 ms. The maximum flip angle in the sweep was set to 30 degrees in order to preserve the longitudinal magnetization for tagging in the next cardiac cycle.
3. The retrospectively-gated DENSE acquisitions were performed using a pulse oximeter as the triggering device, which was attached to the left index finger.
4. Scan duration is reported for a heart rate of 60 beats/min and for one motion encoding direction.

Volumetric strain was calculated as the divergence of the tissue displacement maps. Divergence is a spatial operator which acts across neighbouring voxels, which may contain different tissue types, thus confounding tissue-based region of interest (ROI) analyses. To limit the 'bleeding' of neighbouring ROIs, the displacement maps were masked with the brain tissue ROIs prior to the volumetric strain calculation. The volumetric strain maps were first generated for each DENSE dynamic, after which the strain dynamics were averaged together (strains derived from the negatively acquired dynamic were negated). Creating the strain maps in this manner maximized the available ROI sizes, as 'holes' from excluded artefact areas[6] were filled using values from the both dynamics. Additionally, voxels with an absolute volumetric strain exceeding 1.5 % were excluded from the analysis as they are unrealistic for cardiac-induced tissue motion derived from the microvasculature[6]. Consequently, voxels with strains exceeding the threshold were removed from the ROI for

all cardiac frames, regardless of the time frame of occurrence. A complimentary analysis of the high strain voxels can be found in the accompanying Chapter 4 (part II).
The strain data were shifted temporally to reflect volumetric strain arising from vectorcardiogram synchronisation instead of a pulse oximeter placed at the index finger[6]. An example volumetric strain map is shown in Figure 1.

2.2.2 Brain tissue ROIs

Brain tissue ROIs were created using the Computational Anatomy Toolbox (Jena University Hospital, Departments of Psychiatry and Neurology)[10] extension for SPM12 (Wellcome Trust Centre for Neuroimaging, University College London - https://fil.ion.ucl.ac.uk/spm). The Computational Anatomy Toolbox automatically segments the brain tissue from the 3D T1-weighted image, resulting in CSF, GM and WM tissue probability maps. Voxels in the tissue probability map with a probability exceeding 95% were used to define the GM and WM tissue ROIs. Similarly, the WB tissue ROI was constructed by combining the grey and white matter tissue probability maps.

Using the T1-weighted image as input, the Computational Anatomy Toolbox was also used to generate an anatomical map with labels for the brain stem and cerebellum. As WMH are predominantly located in the cerebrum, the analysis was simplified by removing regions labelled as brain stem and cerebellum from all tissue ROIs. Additionally, voxels with a non-zero probability in the CSF tissue probability map were removed from all tissue ROIs.
Although typical tissue volumes of the healthy young brain are in the range of 1-1.5 L[11], in this study less tissue volume was available for analysis due to erosion of ROI edges as a result of performing spatial derivatives to calculate the volumetric strain. This loss of tissue volume for analysis was further compounded by the omission of the brain stem and cerebellum from all ROIs, as well as omission of tissue regions which contained artifacts.

2.2.3 WMH ROI

The WMH were identified in the patient group using the lesion prediction algorithm[12] as implemented in the Lesion Segmentation Tool toolbox (version 3.0.0 - www.statistical-modelling.de/lst.html) for SPM12. The toolbox identified lesions for each patient using their associated FLAIR and T1-weighted images as input, and generated a lesion probability map in the subject's T1-weighted image space. The WMH ROI was defined as regions with a

probability greater than 70% in the lesion probability map (Figure 2a). The WMH and WM ROIs were used to define the NAWM ROI. The control group consisted of healthy young subjects and therefore had no WMH.

2.2.4 WMH-risk ROI

WMH-risk (WMH_R) probability maps were generated for the control group using a WMH count map, derived from a multi-centre/multi-scanner image dataset consisting of 170 subjects[13]. The WMH count map was constructed in MNI space, where the value of each voxel in the map represented the summed occurrence of a WMH from all subjects in the dataset at that specific voxel location. Elastix[14] was used to transform the WMH count map from MNI space to the native T1-weighted image space acquired for each subject in this study. The voxel values in the WMH count map were rescaled to lie between 0 and 100 to represent a WMH_R probability map. The WMH_R ROI was then defined as regions in the WMH_R probability map with a probability greater than 25% (see Figure 2b)).

2.3 Statistics

The average volumetric strain in all ROIs (WB, GM, NAWM and WMH or WMH_R) for each cardiac frame was calculated, resulting in 4 volumetric strain curves for each subject. The individual strain curves were observed to be noisy, which for some subjects resulted in difficulty identifying a clear peak (Fig 5). Therefore, for each ROI the group mean strain curve was first calculated and used to determine the moment of group peak strain. The peak strain for each subject was then defined as the subject's maximum strain value in a 3x1 window centered at the moment of group peak. This value was used to calculated the group mean +/- std peak strain.

For both the patient and control groups, Student's paired T-Test was used to investigate the intra-group differences between the GM and NAWM peak volumetric strain. Similarly, intra-group differences in peak volumetric strain between NAWM and WMH (patient group), and between NAWM and WMH_R (control group) regions of interest were investigated.
Student's unpaired T-Test was used to explore inter-group differences in peak GM and NAWM between the patient and control groups.

3. Results

All DENSE measurements were successfully acquired for both study groups. However, one subject in the patient group was removed from further analyses after qualitative inspection of the data revealed the presence of a large number of phase artifacts. In the remaining subjects, displacement and strain maps were successfully obtained from the DENSE data. The mean tissue volume obtained from the T1w scan was smaller in the patient group vs controls (group mean ± std, including brain stem and cerebellum): 1044 ± 111 cm^3 vs 1308 ± 53 cm^3, respectively. Likewise, the mean tissue volume in the masks in which the volumetric strain (without brain stem or cerebellum) was smaller in the patient group then in the control group: 801 ± 88 cm^3 vs 1082 ± 61 cm^3, respectively. With respect to the total tissue volume, a relatively large volume of high strain voxels was removed from the patient

group in comparison to the controls (group mean± std : (119 ± 56) cm^3 vs (15.5 ± 4.6) cm^3, respectively).

We observed spatially similar brain tissue displacement patterns in patient and controls, which were directed towards the ventricles and foramen magnum. However, the volumetric strain maps looked relatively noisy, and no overt spatial patterns were observed (see Figure 1). Despite the noisy appearance of the strain maps, the mean tissue strain curves revealed a general increase in volumetric strain during systole, followed by a (relatively) slower decrease to baseline during diastole.

The mean volumetric strain for all analysed ROIs and also the time to peak is reported in Table 2. The ratio of the mean volumetric strain for GM vs NAWM was also determined (group mean± std) for patients (1.5 ± 0.4) and controls = (2.4 ± 1.3).

	Volumetric Strain Peak (Mean ± Std) x 10^{-4}		***Time to Peak (%) (Mean ± Std)***		***ROI Volume (ml) (Mean ± Std)***	
	Patients	***Controls***	***Patients***	***Controls***	***Patients***	***Controls***
GM	(6.5 ± 1.6)	(8.4 ± 2.4)	(37.5 ± 2.5)	(29.4 ± 3.9)	(30.5 ± 16.7)	(167.3 ± 30.7)
NAWM	(4.4 ± 0.9)	(4.0 ± 1.4)	(40.0 ± 4.1)	(46.3 ± 3.3)	(110.6 ± 53.3)	(186.0 ± 22.6)
WB	(5.9 ± 1.2)	(5.2 ± 1.4)	(40.0 ± 4.1)	(34.4 ± 3.0)	(364.1 ± 154.1)	(825.6 ± 75.0)
WMH	(6.6 ± 3.5)	-	(35.0 ± 4.1)		(7.6± 9.2)	-
WMH_R	-	(3.5 ± 1.7)		(44.4 ± 3.9)	-	(24.0 ± 2.2)

Table 2. Group mean peak volumetric strain within the analysed ROIs, and the associated mean ROI volumes. We further report the group mean time to peak of the volumetric strain within the analysed ROIs, which is reported as percentage of the participant's average cardiac cycle (relative to a vectorcardiogram trigger). GM=grey matter; NAWM=normal appearing white matter; WMH=white matter hyperintensity; WMH_R = white matter hyperintensity risk

	Volumetric Strain Peak	*Volumetric Strain Time to Peak*
	p-value	p-value
(Patient) intra-group paired t-test		
GM vs NAWM	**0.020**	0.203
NAWM vs WMH	0.183	0.111
(Controls) intra-group paired t-test		
GM VS NAWM	**0.003**	**0.001 <**
NAWM VS WMH$_R$	0.263	0.197
Inter-group unpaired t-test		
Patient GM vs Control GM	0.115	**0.001**
Patient NAWM vs Control NAWM	0.596	**0.019**
Patient WB vs Control WB	0.358	**0.029**
Patient WMH vs Control WMH$_R$	0.106	**0.002**

Table 3. Results of the inter- and intra-group t-test for differences in the group mean volumetric strain peak, and time to peak among the GM, NAWM, WMH and WMH$_R$ regions of interest. Bolded values reflect significant differences (p-value < 0.05)

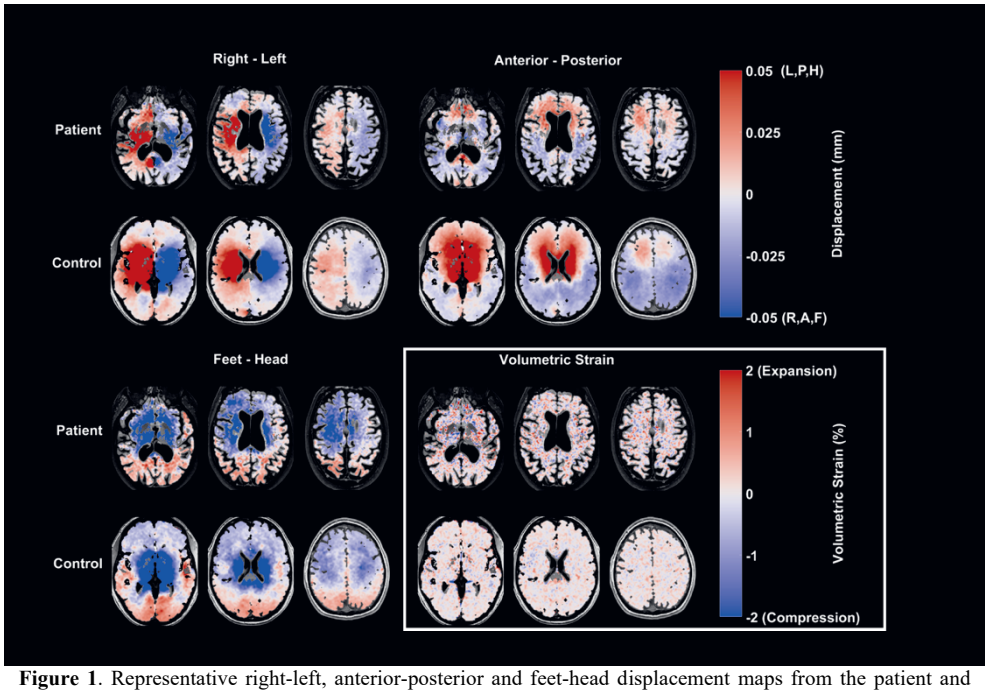

Figure 1. Representative right-left, anterior-posterior and feet-head displacement maps from the patient and control cohorts. The derived volumetric strain map is also shown. All maps are represented at the moment of peak systole.

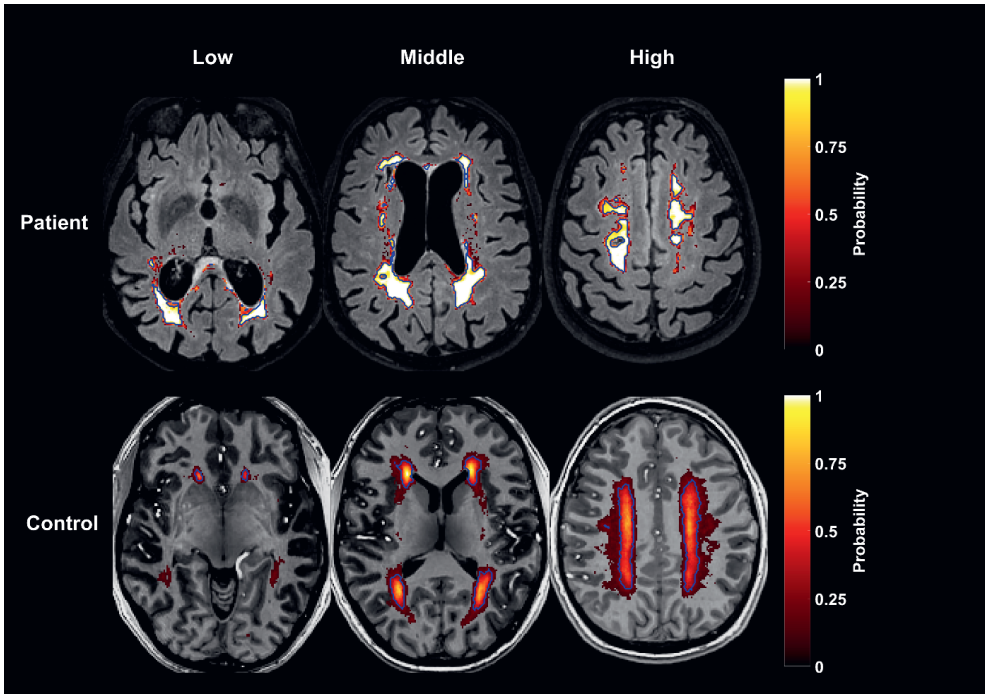

Figure 2. Representative images showing the WMH (patient) and WMH_R (controls) probability maps, overlaid on the subject's FLAIR (patient) and T1-weighted (controls) MR images. The WMH_R maps represent the probability of developing a WMH later in life, given a WMH incidence map derived from a cohort of 170 patients. Image slices are shown at the low, middle and high regions of the brain. The WMH and WMH_R ROIs used in this study are delineated in blue.

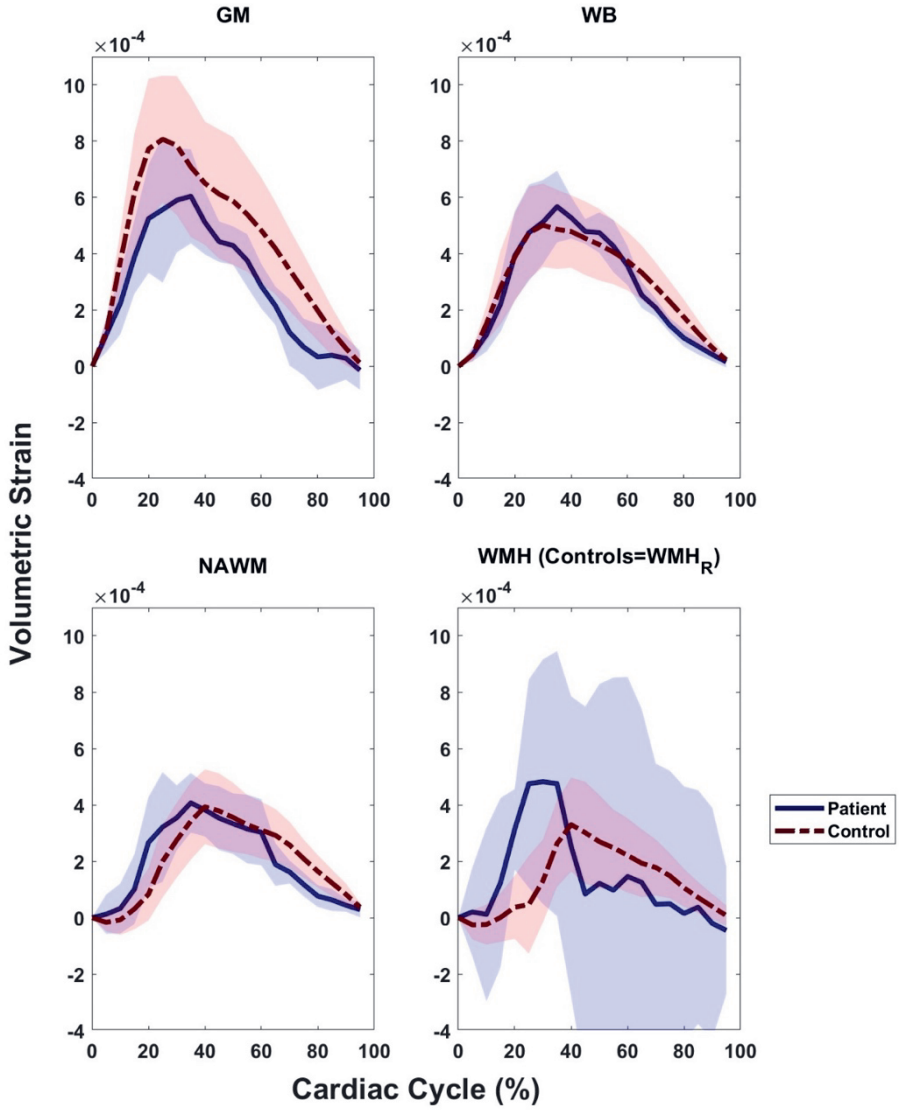

Figure 3. Group mean strain curves for all ROIs, representing regional brain tissue strain over the cardiac cycle beginning at systole. The shaded regions reflect the group mean standard deviation.

4. Discussion

Cardiac-induced brain tissue volumetric strain measurements covering the entire brain and cardiac cycle were obtained in a patient and control cohort. This study evaluated the peak, and time to peak volumetric strain within anatomical-based ROIs (GM, NAWM, WB), WMH (patients), and regions at risk to the development of WMH (controls). The volumetric strain measurements reflect blood volume changes occurring within the ROIs as a result of cardiac output[6]. WMH are a suitable target to evaluate the potential usefulness of cardiac-induced volumetric strain since they are thought to result from microvascular dysfunction[1,15–17]. Significantly higher peak volumetric strains were found in the GM compared to the NAWM ROI for both patients and controls. Additionally, the patient group demonstrated significantly earlier time to peak strain in the NAWM and WMH ROIs compared to the corresponding regions in controls, and a significantly later time to peak in the GM and WB ROIs. Taken altogether, the earlier peak strains in the NAWM of the patients can be interpreted as arising from a stiffer vasculature in this group. These results highlight the utility of volumetric strain to illuminate physiological alterations to brain tissue as a result of age and disease.

4.1 Volumetric strain peak observations

For the inter-group analyses, the GM, NAWM, WB and WMH/ WMH_R peak strains were not found to be significantly different. Given the vastly different age, physical condition, and diseased state of the two groups, a difference in peak strain was expected. However, the relatively small sample size and the intrinsically high noise levels of the volumetric strain measurements likely yielded insufficient power to observe such differences. On the other hand, biological differences between the groups may also manifest in other characteristics of the strain energy, such as time to peak, which is expanded on below. Using the mean tissue volumes and peak volumetric strain (Table 2), we estimate a peak brain tissue volume change of approximately 0.47 ml and 0.55 ml for the patient and control groups, respectively (Table S3). Previously, we demonstrated that the whole brain volume change is correlated to the CSF stroke volume at the cranio-cervical junction level[6], suggesting that the brain tissue also contributes to the maintenance of a stable intracranial pressure. Stoquart-ElSankari et al. report a reduction in CSF stroke volume for healthy elderly subjects[18], as do Burman et al.[19], which is consistent with our measurements of a reduced cardiac-induced brain tissue volume change in the patient group. However, a more recent study shows an increase of CSF stroke volume with age in healthy elderly subjects[20]. This is not at ends with our results since it is conceivable that the peak brain tissue strain is altered differently depending on the relative rate of stiffening in microvasculature versus macrovasculature which occurs naturally with age. If the microvasculature is much stiffer than the macrovasculature then a reduction in tissue volumetric strain is expected. Conversely, a stiffer macrovasculature in comparison to the microvasculature should lead to an increase in peak volumetric strain due to a larger pulsatile energy being transferred to the microvasculature. Therefore, an increase or decrease

in the corresponding CSF stroke volume may be found with age depending on the cohort or disease being studied. This highlights a potential challenge with interpretation of the strain measurements.

For the intra-group analyses, the GM peak strain was significantly larger than the NAWM peak strain for both the patient ($p=0.02$) and controls ($p<0.01$). We previously hypothesised that in healthy subjects, time to peak differences between grey and white matter may be related to a preferential deposit of blood to grey matter due to its denser vascularisation, which acts as a buffer before the blood volume arrives in the white matter[6,21]. The centripetal vascular organisation of the brain may also contribute to the reduced NAWM peak since more pulsatile energy can be dampened along the longer medullary and subcortical arteries which nourish the NAWM relative to the shorter cortical arteries which nourish the GM[22]. In this study, we observed in the patient group a reduced ratio between peak GM and NAWM, resulting from a decrease in GM strain and concomitant increase in NAWM strain. This, in conjunction with the observed simultaneous earlier filling of NAWM, may reflect a stiffer extracerebral and intracortical vascularisation which directs the pulsatile energy deeper into the WM. With age, arteriosclerosis of the cerebral arteries leads to stiffening of the vessel walls and a reduced damping of the cardiac pulsatile energy, which is thought to damage the microvasculature[27], possibly contributing to the onset of WM lesions[23] and cerebral Small Vessel Disease[24]. However, no significant differences were observed in the WMH and WMHR ROIs when compared to the NAWM ROI, suggesting that peak cardiac-induced volumetric strain alone cannot differentiate between the global changes in white matter associated with cSVD[25,26], and the specific underlying pathological changes which result in WMH.

4.2 Volumetric Strain Time to Peak Observations

The statistically significant later GM peak for the patient population in comparison to the controls is peculiar, but may be interpreted as stiffening of the GM microvasculature. In that case, although the stiffer microvasculature still retains some capacity to expand, evidently the pressure corresponding to pulsatile energy is directed towards 'flushing' the microvasculature instead of dilation. This would also explain the slightly diminished peak observed in that ROI in comparison to the controls. However, the contribution from the fraction of large strains which were excluded from this analysis also cannot be ignored, as notably their inclusion leads to a time to peak which is not significantly different than the controls (Table 2 in Chapter 4 (part II)).

Curiously, relative to the controls, we observed in the patient group a delay in their GM time to peak representing about 6% of cardiac cycle, and a simultaneous earlier onset of peak NAWM of about 6%, leading to a reduced delta in time to peak of both ROIs (~3% of the

cardiac cycle in patients compared to ~16% in controls). Congruent with our earlier reasoning, we interpret the statistically significant earlier onset of peak NAWM strain in the patient group when compared to the controls as a faster transfer of pulsatile energy from the cerebral vessels into the WM microvasculature due to intracranial arteriosclerosis which is associated with the age and vascular disease of the patient population. The intracranial vascular organisation leads to blood pressure gradients in the brain. In particular, the thalamic and lenticulostriate perforators are functionally terminal arteries that feed the deep white matter, and are under high pressure[27]. As such the higher pressure and likely stiffer vasculature of the patient group may contribute to the observed early transfer of strain energy to the deep white matter. In light of this, the WMH significantly earlier time to peak in comparison to the corresponding at-risk regions in the control group is expected, given their location in the WM tissue. Further, as we did not discriminate WMH by location in this analysis, the WMH in the flow territories of the thalamic and lenticulostriate perforators may experience particularly early strain due to the high pressure in these perforators.

4.3 Volumetric strain waveform observations

Although not quantitatively analysed, from a qualitative perspective the group mean strain waveforms provides an interesting insight into the (ex)-changes of the pulsatile energy between the ROIs over an average cardiac cycle. The group mean curves of WMH and WMH_R qualitatively show an altered waveform in comparison to their NAWM counterparts. In patients there is a rapid rise and fall from peak during systole compared to the NAWM, whereas in controls, the alteration to the shape of the strain curve is more subtle, with mainly a delayed rise during systole. The delayed onset of the strain wave in controls in the WMH_R region likely reflects that this region is at the end of the vascular bed[27].

The large inter-subject variation present in the patient WMH curves (which is notably absent in other ROIs) may be attributed to the relatively low ROI volume, and the spatial distribution of the lesions among the patients. A larger fluid content in the WMH ROI arising from leakage of the blood brain barrier, decreased interstitial fluid drainage and increased perivascular spaces[25] may also be a compounding factor. Additionally, an increase in brain tissue fluid content is associated with WM lesions and increased pulsations from a stiffened arterial vasculature[23]. The increased fluid content in the lesion tissue will likely alter the tissue's viscoelastic properties relative to NAWM, potentially contributing to the observed 'chaotic' pattern of pulsatile strains in the WMH ROI.

4.4 Volumetric strain map observations

A larger heterogeneity in the volumetric strain map was observed in the patient population, which is further supported by the histograms of the WB peak strain (see Figure 1 of Chapter 4 (part II)). The larger heterogeneity may be a result of higher physiological noise. Increased

thermal noise due to different scanner hardware and software cannot fully be excluded, since the data of the patient group was acquired at a much later date than the control group, but is not likely as this amount of increased noise would also lead to visible image quality reduction in other (anatomic) scans, which was not observed. Another relevant factor might be involuntary head motion, which is known to be altered in patients with brain disease[28]. When considering the potential contribution of physiological noise, the age-related decline in capillary density[29,30] and concomitant decline in brain tissue stiffness, and variation across brain tissue regions[31,32], and further alterations in disease[33–35] may explain the larger heterogeneity under a simplistic model where the compliance of the microvascular vessel walls and surrounding parenchyma are treated as one entity. Such a simple model ignores the perivascular spaces (PVS) that surrounds the penetrating vasculature, which is known to be enlarged in cohorts expressing WMH[36] and, and also exhibits pulsatile flow characteristics[37]. Due to the dynamic behaviour and incompressibility of its constituent fluids, it is assumed that extending the simple model to include enlarged PVS would lead to increased heterogeneity. We note that size and presence of PVS throughout the brain tissue[38] leads to the natural conclusion that they must also be included in our volumetric strain maps, and thus posit that larger PVS are another potential explanation for the larger strain heterogeneity observed in the patient group.

4.5 FH displacement encoding observations

Analogously to the velocity encoding parameter V_{enc}, we previously designed the displacement encoding parameter D_{enc} to reflect the maximum wrap-free displacement in the resulting subtracted phase images[6,7]. In this study, we observed the need to increase the D_{enc} value of the FH DENSE measurements for some subjects in the patient group due to high sensitivity to artifacts, which occur due to phase inconsistency in the segmented 3D acquisition. Such inconsistency can occur from inconsistent contributions of the respiration and involuntary head motion, which is mainly in the FH direction as motion in the AP and RL directions are more constricted due to gravity and the fixation of the patient in the headcoil by padding, respectively. This observation also points to higher head motion in the patients relative to controls. Although increasing the D_{enc} causes an increase in the image magnitude SNR (less signal loss from diffusion effects[39]), the resulting sensitivity to displacements is decreased, which mitigates the sensitivity to artifacts from motion variability between the different shots of the 3D acquisition[8,40]. At the same time, also larger heartbeat-induced FH brain motion was observed (data not shown). The reason for the larger displacements in these subjects is unclear, however a general decreased intracranial compliance associated with age may be complicit[41–43], allowing the transfer of greater pulsatile energy (momentum) to the parenchyma.

4.6 Study limitations

In this study, we lacked age-matched controls, which would likely have improved our understanding of the effect of age on the tissue volumetric strain separately from the disease which exist in our patient population. Nonetheless, despite the lack of age-matched controls and low number of subjects per group available for analysis, we believe this work is informative as a first explorative study of how the method performs in patients. In the healthy controls, we assessed the WM at-risk regions, without care that WMH may never develop in those subjects. Ideally, a proper analysis would stem from a longitudinal study comparing before/after measurements of groups who did and did not develop WMH in those regions, or at all. Even then, some care is also necessary in interpreting the tissue volumetric strain across ROIs, as one must consider not only differences in the underlying tissue compliance/viscoelastic properties[44], but likely also vascular differences such as average vessel size, type, density[45], and stiffness. Interpretations across subject groups should consider these differences as well, since the diameter and density of the small vessels change with age, dementia and leukoaraiosis[29,30]. Therefore, comparisons of tissue volumetric strain between the patient and control groups likely also compare the contribution of small vessels of different sizes and density. Despite, or rather because of these limitations, we mark our objective as complete as we have demonstrated that brain tissue volumetric strain can detect differences between patients with vascular disease and healthy controls. It thus provides another tool in our arsenal to yield new insights into alterations to the brain as a result of age and disease.

5. Conclusion

We observed significantly altered volumetric strain patterns in a patient cohort which were consistent with the pulse wave encephalopathy hypothesis. This study further demonstrates the potential of brain tissue volumetric strain measurements as a tool to elucidate the changes to the brain microvasculature which arise due to disease or age, which might help in understanding brain tissue lesions seen in patients with cerebral small vessel disease.

References

1. Mitchell GF, van Buchem MA, Sigurdsson S, et al. Arterial stiffness, pressure and flow pulsatility and brain structure and function: the Age, Gene/Environment Susceptibility – Reykjavik Study. *Brain*. 2011;134(11):3398-3407. doi:10.1093/brain/awr253
2. Henry-Feugeas MC, Roy C, Baron G, Schouman-Claeys E. Leukoaraiosis and pulse-wave encephalopathy: Observations with phase-contrast MRI in mild cognitive impairment. *Journal of Neuroradiology*. 2009;36(4):212-218. doi:10.1016/j.neurad.2009.01.003
3. Tarumi T, de Jong DLK, Zhu DC, et al. Central artery stiffness, baroreflex sensitivity, and brain white matter neuronal fiber integrity in older adults. *Neuroimage*. 2015;110:162-170. doi:10.1016/j.neuroimage.2015.01.041
4. Nwotchouang BST, Eppelheimer MS, Biswas D, et al. Accuracy of cardiac-induced brain motion measurement using displacement-encoding with stimulated echoes (DENSE) magnetic resonance imaging (MRI): A phantom study. *Magn Reson Med*. 2021;85(3):1237-1247. doi:10.1002/mrm.28490
5. Soellinger M, Rutz AK, Kozerke S, Boesiger P. 3D cine displacement-encoded MRI of pulsatile brain motion. *Magn Reson Med*. 2009;61(1):153-162. doi:10.1002/mrm.21802
6. Adams AL, Viergever MA, Luijten PR, Zwanenburg JJM. Validating faster DENSE measurements of cardiac-induced brain tissue expansion as a potential tool for investigating cerebral microvascular pulsations. *Neuroimage*. 2020;208(December 2019):116466. doi:10.1016/j.neuroimage.2019.116466
7. Adams AL, Kuijf HJ, Viergever MA, Luijten PR, Zwanenburg JJM. Quantifying cardiac-induced brain tissue expansion using DENSE. *NMR Biomed*. 2019;32(2):e4050. doi:10.1002/nbm.4050
8. Spottiswoode BS, Zhong X, Hess AT, et al. Tracking myocardial motion from cine DENSE images using spatiotemporal phase unwrapping and temporal fitting. *IEEE Trans Med Imaging*. 2007;26(1):15-30. doi:10.1109/TMI.2006.884215
9. Stuber M, Spiegel MA, Fischer SE, et al. Single breath-hold slice-following CSPAMM myocardial tagging. *Magnetic Resonance Materials in Physics, Biology and Medicine*. 1999;9(1-2):85-91. doi:10.1016/S1352-8661(99)00049-6
10. Gaser C, Dahnke R, Thompson PM, Kurth F, Luders E. CAT-A Computational Anatomy Toolbox for the Analysis of Structural MRI Data. *bioRxiv*. Published online 2022. doi:10.1101/2022.06.11.495736
11. Kijonka M, Borys D, Psiuk-Maksymowicz K, et al. Whole Brain and Cranial Size Adjustments in Volumetric Brain Analyses of Sex- and Age-Related Trends. *Front Neurosci*. 2020;14. doi:10.3389/fnins.2020.00278
12. Schmidt P. Bayesian inference for structured additive regression models for large-scale problems with applications to medical imaging. Dissertation, LMU München: Faculty of Mathematics, Computer Science and Statistics. 2016;(November):Chapter 6.1.
13. Kuijf HJ, Casamitjana A, Collins DL, et al. Standardized Assessment of Automatic Segmentation of White Matter Hyperintensities and Results of the WMH Segmentation Challenge. *IEEE Trans Med Imaging*. 2019;38(11):2556-2568. doi:10.1109/TMI.2019.2905770
14. Klein S, Staring M, Murphy K, Viergever MA, Pluim J. elastix: A Toolbox for Intensity-Based Medical Image Registration. *IEEE Trans Med Imaging*. 2010;29(1):196-205. doi:10.1109/TMI.2009.2035616
15. Wardlaw JM, Smith C, Dichgans M. Small vessel disease: mechanisms and clinical implications. *Lancet Neurol*. 2019;18(7):684-696. doi:10.1016/S1474-4422(19)30079-1
16. Aribisala BS, Morris Z, Eadie E, et al. Blood Pressure, Internal Carotid Artery Flow Parameters, and Age-Related White Matter Hyperintensities. *Hypertension*. 2014;63(5):1011-1018. doi:10.1161/HYPERTENSIONAHA.113.02735
17. Tsao CW, Seshadri S, Beiser AS, et al. Relations of arterial stiffness and endothelial function to brain aging in the community. *Neurology*. 2013;81(11):984-991. doi:10.1212/WNL.0b013e3182a43e1c

18. Stoquart-ElSankari S, Balédent O, Gondry-Jouet C, Makki M, Godefroy O, Meyer ME. Aging Effects on Cerebral Blood and Cerebrospinal Fluid Flows. *Journal of Cerebral Blood Flow & Metabolism*. 2007;27(9):1563-1572. doi:10.1038/sj.jcbfm.9600462
19. Burman R, Alperin N, Lee SH, Ertl-Wagner B. Patient-specific cranio-spinal compliance distribution using lumped-parameter model: its relation with ICP over a wide age range. *Fluids Barriers CNS*. 2018;15(1):29. doi:10.1186/s12987-018-0115-4
20. Lokossou A, Metanbou S, Gondry-Jouet C, Balédent O. Extracranial versus intracranial hydro-hemodynamics during aging: A PC-MRI pilot cross-sectional study. *Fluids Barriers CNS*. 2020;17(1). doi:10.1186/s12987-019-0163-4
21. Bhogal AA, Philippens MEP, Siero JCW, et al. Examining the regional and cerebral depth-dependent BOLD cerebrovascular reactivity response at 7T. *Neuroimage*. 2015;114:239-248. doi:10.1016/j.neuroimage.2015.04.014
22. Smirnov M, Destrieux C, Maldonado IL. Cerebral white matter vasculature: still uncharted? *Brain*. 2021;144(12):3561-3575. doi:10.1093/brain/awab273
23. Bateman GA. Pulse wave encephalopathy: A spectrum hypothesis incorporating Alzheimer's disease, vascular dementia and normal pressure hydrocephalus. *Med Hypotheses*. 2004;62(2):182-187. doi:10.1016/S0306-9877(03)00330-X
24. Henry Feugeas MC, de Marco G, Peretti II, Godon-Hardy S, Fredy D, Claeys ES. Age-related cerebral white matter changes and pulse-wave encephalopathy: Observations with three-dimensional MRI. *Magn Reson Imaging*. 2005;23(9):929-937. doi:10.1016/j.mri.2005.09.002
25. Wardlaw JM, Makin SJ, Valdés Hernández MC, et al. Blood-brain barrier failure as a core mechanism in cerebral small vessel disease and dementia: evidence from a cohort study. *Alzheimer's and Dementia*. 2017;13(6):634-643. doi:10.1016/j.jalz.2016.09.006
26. Papma JM, de Groot M, de Koning I, et al. Cerebral small vessel disease affects white matter microstructure in mild cognitive impairment. *Hum Brain Mapp*. 2014;35(6):2836-2851. doi:10.1002/hbm.22370
27. Spence J. Blood Pressure Gradients in the Brain: Their Importance to Understanding Pathogenesis of Cerebral Small Vessel Disease. *Brain Sci*. 2019;9(2):21. doi:10.3390/brainsci9020021
28. Zeng LL, Wang D, Fox MD, et al. Neurobiological basis of head motion in brain imaging. *Proc Natl Acad Sci U S A*. 2014;111(16):6058-6062. doi:10.1073/pnas.1317424111
29. Choi H il, Ryu CW, Kim S, Rhee HY, Jahng GH. Changes in Microvascular Morphology in Subcortical Vascular Dementia: A Study of Vessel Size Magnetic Resonance Imaging. *Front Neurol*. 2020;11. doi:10.3389/fneur.2020.545450
30. Brown WR, Thore CR. Review: Cerebral microvascular pathology in ageing and neurodegeneration. *Neuropathol Appl Neurobiol*. 2011;37(1):56-74. doi:10.1111/j.1365-2990.2010.01139.x
31. Takamura T, Motosugi U, Sasaki Y, et al. Influence of Age on Global and Regional Brain Stiffness in Young and Middle-Aged Adults. *Journal of Magnetic Resonance Imaging*. 2020;51(3):727-733. doi:10.1002/jmri.26881
32. Yin Z, Romano AJ, Manduca A, Ehman RL, Huston J. Stiffness and beyond: What MR elastography can tell us about brain structure and function under physiologic and pathologic conditions. *Topics in Magnetic Resonance Imaging*. 2018;27(5):305-318. doi:10.1097/RMR.0000000000000178
33. ElSheikh M, Arani A, Perry A, et al. MR elastography demonstrates unique regional brain stiffness patterns in dementias. *American Journal of Roentgenology*. 2017;209(2):403-408. doi:10.2214/AJR.16.17455
34. Murphy MC, Jones DT, Jack CR, et al. Regional brain stiffness changes across the Alzheimer's disease spectrum. *Neuroimage Clin*. 2016;10:283-290. doi:10.1016/j.nicl.2015.12.007
35. Chaze CA, McIlvain G, Smith DR, et al. Altered brain tissue viscoelasticity in pediatric cerebral palsy measured by magnetic resonance elastography. *Neuroimage Clin*. 2019;22. doi:10.1016/j.nicl.2019.101750

36. Potter GM, Doubal FN, Jackson CA, et al. Enlarged perivascular spaces and cerebral small vessel disease. *International Journal of Stroke*. 2015;10(3):376-381. doi:10.1111/ijs.12054
37. Mestre H, Tithof J, Du T, et al. Flow of cerebrospinal fluid is driven by arterial pulsations and is reduced in hypertension. *Nat Commun*. 2018;9(1):4878. doi:10.1038/s41467-018-07318-3
38. Sepehrband F, Barisano G, Sheikh-Bahaei N, et al. Image processing approaches to enhance perivascular space visibility and quantification using MRI. *Sci Rep*. 2019;9(1). doi:10.1038/s41598-019-48910-x
39. Sloots JJ, Biessels GJ, de Luca A, Zwanenburg JJM. Strain Tensor Imaging: Cardiac-induced brain tissue deformation in humans quantified with high-field MRI. *Neuroimage*. 2021;236. doi:10.1016/j.neuroimage.2021.118078
40. Epstein FH, Gilson WD. Displacement-encoded cardiac MRI using cosine and sine modulation to eliminate (CANSEL) artifact-generating echoes. *Magn Reson Med*. 2004;52(4):774-781. doi:10.1002/mrm.20232
41. Czosnyka Z, Whitfield PC, Donovan, Pickard T, John D. *Age Dependence of Cerebrospinal Pressure: Volume Compensation in Patients with Hydrocephalus*.; 2001. http://insight.cumbria.ac.uk/id/eprint/1046/
42. Bateman GA, Levi CR, Schofield P, Wang Y, Lovett EC. The venous manifestations of pulse wave encephalopathy: Windkessel dysfunction in normal aging and senile dementia. *Neuroradiology*. 2008;50(6):491-497. doi:10.1007/s00234-008-0374-x
43. Eppelheimer MS, Nwotchouang BST, Pahlavian SH, et al. Cerebellar and brainstem displacement measured with DENSE MRI in chiari malformation following posterior fossa decompression surgery. *Radiology*. 2021;301(1):187-194. doi:10.1148/radiol.2021203036
44. Ji S, Fan X, Roberts DW, Paulsen KD. Cortical Surface Strain Estimation Using Stereovision. In: Vol 100. ; 2011:412-419. doi:10.1007/978-3-642-23623-5_52
45. Lauwers F, Cassot F, Lauwers-Cances V, Puwanarajah P, Duvernoy H. Morphometry of the human cerebral cortex microcirculation: General characteristics and space-related profiles. *Neuroimage*. 2008;39(3):936-948. doi:10.1016/j.neuroimage.2007.09.024

Chapter 4 (Part II)

Investigating the high strain energies present in measurements of cardiac-induced brain tissue pulsations in patients with white matter lesions

This chapter is based on the following research article currently in submission to the Journal of Magnetic Resonance Imaging: Adams, A. L., Rots, M., de Borst, G. J., & Zwanenburg, J. J. M. (*2023*). *Measurements of Cardiac-Induced Brain Tissue Pulsations in Patients with White Matter Lesions*.

1. Introduction

In section 2.2.1 of Chapter 4 (part I), we reported the exclusion of volumetric strains with an absolute value exceeding 1.5% (henceforth referred to as high strains). Previously, a threshold of 1% was used for healthy subjects[1] as it is thought to represent an unrealistic change in blood volume for the tissue microvasculature. Typical grey and white matter volumes are in the range of 620 – 800 cm^3 [2], thus a volumetric strain of 1.5% would suggest an equivalent change of 9.3 – 12 ml of blood volume within the tissue as a result of cardiac output. This unrealistic value for voxel strains may arise from other physiological sources, such as partial volume effects arising from the (extra)cerebral macrovasculature or CSF pulsations, or simply noise. As these sources were not of interest for our interpretation of the tissue microvasculature, a strict rule was employed to exclude voxels from the ROIs if they exhibited a high strain value at any moment in cardiac cycle.

2. Method

A histogram analysis of the peak volumetric strains for all subjects (Figure 1) suggests that for patients, even the slightly increased threshold of 1.5% removes the tail ends of their distributions, and feasibly valuable data about that cohort. Therefore, a complimentary analysis was performed to observe the influence of the high strains by repeating the analysis with their inclusion. This allows a holistic view of the cardiac-induced intracranial pulsations in the patient group, and how it is potentially altered relative to healthy controls. An examination of the mean waveform, volume and temporal occurrence of the high strain voxels in the tissue ROIs was also performed to separately explore intra- and inter-subject differences in these high strain voxels.

3. Results and Discussion

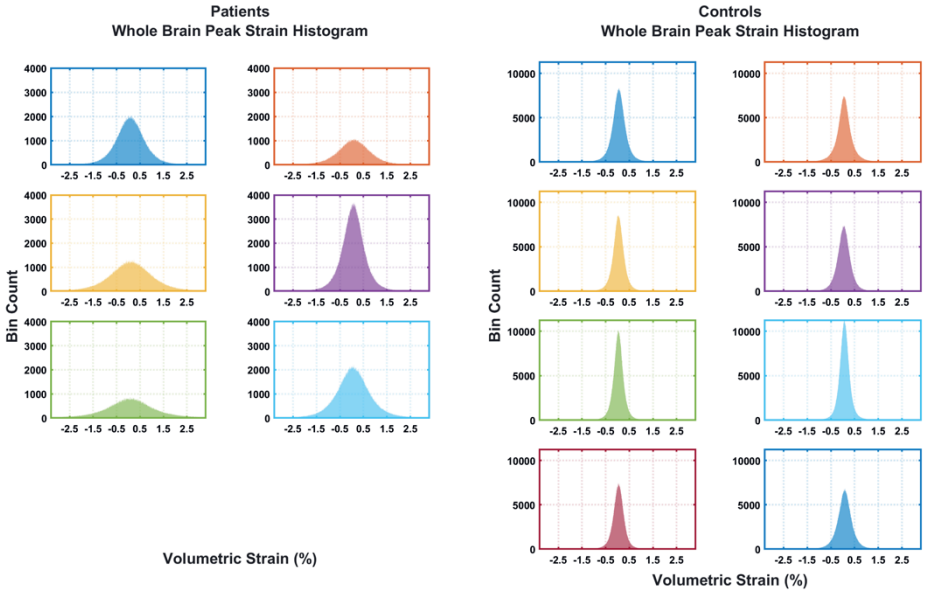

Figure 1. Histogram analysis of peak whole brain volumetric strain for the patient and control cohorts. The histogram bin width was set to 0.005 %. Voxels with an absolute strain greater than 1.5% at any moment in the cardiac cycle were labelled as high strain, meaning that the overall volume removed is larger than indicated for the single time point histogram analysis shown here.

We now report the main observations of the volumetric strain measurements which simply include the higher strain energies into the analysis. The peak whole brain volumetric strain results in strikingly broader histograms for the patient group, reflecting a more heterogenous dataset (Figure 1). For the control group, the histograms indicate that most of the strain energy is retained if using previously reported absolute threshold of 1%[1]. However, for some subjects in the patient group using this threshold would result in the removal of a substantial number of voxels. Thus, a threshold of 1.5% was instead used for the analyses in Chapter 4 (part I), as this was deemed a practical tradeoff which allowed reasonable retention of ROI voxel volumes in the patient group, while continuing to limit the influence of higher strains.

Inclusion of the high strains to the grey matter (GM) ROI generally results in a systolic strain rate which is similar between the patients and controls, although with a slightly diminished peak value and earlier time to peak in the former. Curiously, the diastolic component of the GM ROI strain is largely unchanged whether the high strains are included or excluded. This hints that the high strain energy may predominantly have a systolic effect in that ROI. The volumetric strain in the normal appearing white matter (NAWM) ROI is also altered in the

patients, revealing a rapid rise during systole and peak strain value that exceeds that of the controls, and slightly delayed decrease during diastole. Taken together, it suggests that the higher strains in the NAWM strains are somewhat compensatory to the apparently "restricted" GM strain activity.

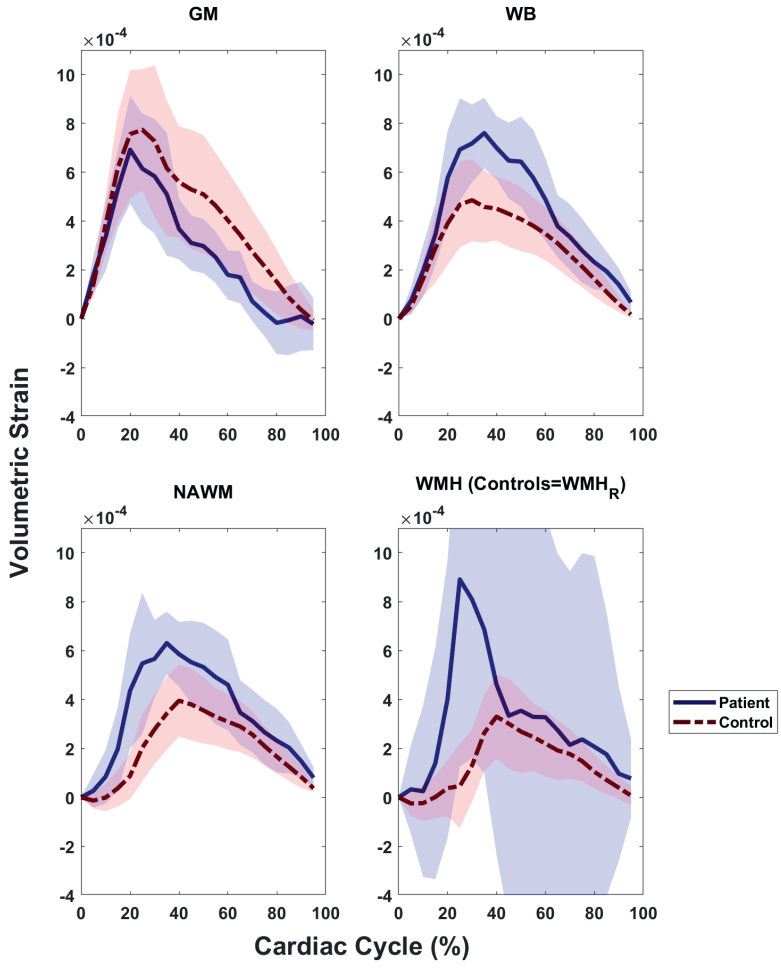

Figure 2. Group mean strain curves for ROIs, representing the combined effect of the full range of strain energies detected in the brain tissue over the cardiac cycle, beginning at systole. Shaded regions reflect the group mean standard deviation.

The whole brain (WB) ROI strains are larger in the patient group. When compared to the high strain excluded analyses, the predominant change in the volumetric strain waveform occurs in the late systolic - early diastolic phase. As the whole brain strain is more susceptible to partial volume effects due to the tissue mask definition, the observed changes might be

related to including venous and/or CSF physiological sources, as follows. In the case of a venous source, this could occur from a mislabelled segmentation leading to the inclusion of highly compliant venous vessels like the sagittal sinuses in the tissue ROIs analyses. If instead the higher strain energies reflect a CSF source, then this could occur from separation of neighbouring gyri due to CSF inflow.

In comparison to the analysis where the high strains are excluded, the general effect of the high strains are primarily amplification of the NAWM and WB strain curves. Thus, if the source of the high strains are CSF pulsations, then this would suggest the presence of small CSF pulsations also in the NAWM tissue. This could feasibly arise from perivascular pulsations in the NAWM ROI, as the perivascular space is known to be enlarged with age[3], and co-occurs in patients with WM lesions and other markers of cerebral small vessel disease[4,5]. Their relatively small diameter (<2mm)[6] would also lead to their inclusion in the tissue strain measurements. However, if the high strain energies reflect contributions mainly from the venous microvasculature, this result further demonstrates the important role of the venous compartment to intracranial compliance.

The group mean strain curves derived from the hyperintense WM (WMH) ROIs demonstrate a large peak during early systole, and rapid decline near end-systole, suggesting that the compression component of the high strain energy quickly acts to limit further expansion in late-systole. The inter-subject variation is also substantially larger in the WMH ROI compared to the ROI representing WMH risk (WMH_R) in the controls. This is likely indicative of chaotic pulsatile energy in this ROI, which is further supported from the high strain volume and occurrence analysis (Figure 3), where despite having the smallest median volume fraction of the patient group, the high strain energies in the WMH ROI have the widest range of occurrences per cardiac cycle.

	Volumetric Strain (Mean ± Std) x 10^{-4}		**Time to Peak (%) (Mean ± Std)**		**ROI Volume (ml) (Mean ± Std)**	
	Patients	**Controls**	**Patients**	**Controls**	**Patients**	**Controls**
Grey Matter	(7.5 ± 2.2)	(8.3 ± 2.7)	(27.5 ± 2.5)	(29.4 ± 3.9)	(41.6 ± 16.1)	(173.2 ± 31.6)
White Matter	(6.6 ± 1.1)	(4.0 ± 1.5)	(40.0 ± 4.1)	(45.6 ± 3.9)	(147.0 ± 49.0)	(187.5 ± 22.2)
Whole Brain	(7.8 ± 1.4)	(5.1 ± 1.6)	(39.2 ± 4.5)	(34.4 ± 3.0)	(482.6 ± 139.8)	(841.1 ± 76.2)
WMH	(10.7 ± 6.8)	-	(31.7 ± 2.4)		(9.3± 12.0)	-
WMH_R	-	(3.4 ± 1.7)		(44.4 ± 3.9)	-	(24.0 ± 2.2)

Table 1. Group mean volumetric strain within the analysed ROIs, and the associated mean ROI volumes, inclusive of high strain energies. We further report the group mean time to peak of the volumetric strain within the analysed ROIs, which is reported as percentage of the participant's average cardiac cycle (relative to a vectorcardiogram trigger).WMH=white matter hyperintensity, WMH_R = white matter hyperintensity risk

The volume of high strain voxels is substantially larger in the patient group in comparison to the controls (group mean± std : (118.5 ± 56.3) cm^3 vs (15.5 ± 4.6) cm^3, respectively). Given the relative volume differences, it is perhaps unsurprising that the main contribution of the high strain energies when included in the analysis is primarily reflected in the patient cohort. The use of an absolute threshold implies that both expansive and compressive high strain energies are included in the averaging. It is thus surprising that the net effect of their inclusion is an observed increase in peak volumetric strain across all ROIs (as a decrease could similarly occur due to the inclusion of compression strains). In the GM ROI, inclusion of high strains also results in earlier time to peak (approximate delta of 10% of the cardiac cycle). This observation adds to the notion that these high volumetric strains are not just (thermal) noise, as noise would average out to zero, but rather reflect physiological effects.

	Peak Volumetric Strain	**Time to Peak Volumetric Strain**
	p-value	p-value
(Patient) intra-group paired t-test		
GM vs NAWM	0.391	**0.002**
NAWM vs WMH	0.187	**0.020**
(Controls) intra-group paired t-test		
GM VS NAWM	**0.006**	**0.001** <
NAWM VS WMH_R	0.249	0.351
Inter-group unpaired t-test		
Patient GM vs Control GM	0.591	0.331
Patient NAWM vs Control NAWM	**0.005**	**0.037**
Patient WB vs Control WB	**0.008**	0.071
Patient WMH vs Control WMH_R	0.062	**0.001** <

Table 2. Results of the inter- and intra-group t-test for differences in the group mean volumetric strain peak, and time to peak among the grey matter, white matter, WMH and at-risk WMH (WMH_R) regions of interest. Bolded values reflect significant differences (p-value < 0.05)

Inclusion of the high strain energies in the patient intra-subject analysis results in GM and NAWM ROIs having similar strain amplitudes. However, the relative timing of their time to peak (TTP) becomes significantly different. We observe no change in significance in intra-group analysis for controls when the high strains are included versus excluded. However, the loss of significance in GM and NAWM TTP inter-group analyses implies that inclusion of high strain energies in the patient group leads to a peak timing which is more similar to healthy tissue, which is suggestive of a compensatory mechanism in the GM.

We note the change in ratio of GM to NAWM volumetric strain to unity for patient group (patients = (1.1 ± 0.4), controls = (2.4 ± 1.4)) when high strain energies are including in the analyses. This is also reflected in the estimated relative tissue volume change. As actual WM

lesions were excluded from the NAWM ROI, this result can be interpreted as arising only from the NAWM. In this ROI the observed volume increase (obtained by multiplying the total NAWM volume with the observed peak volumetric strain) is substantially larger in patients (0.27 ± 0.04) cm^3 than in controls (0.19 ± 0.07) cm^3, which is consistent with pulse wave encephalopathy hypothesis of excessive pulsations in the microvasculature due to a reduced damping in the stiffer (larger) vessels.

	Volume Delta (cm^3) (Excluding high strains)		**Volume Delta (cm^3) (Including high strains)**	
	Patients	***Controls***	***Patients***	***Controls***
GM	(0.24 ± 0.05)	(0.48 ± 0.17)	(0.27 ± 0.07)	(0.47 ± 0.18)
NAWM	(0.18 ± 0.04)	(0.19 ± 0.06)	(0.27 ± 0.04)	(0.19 ± 0.07)
WB	(0.47 ± 0.08)	(0.55 ± 0.18)	(0.62 ± 0.09)	(0.54 ± 0.20)

Table 3. Group mean cardiac-induced peak tissue volume changes in the grey and white matter tissue, and the whole brain, with and without exclusion of high strains. Voxels with high strain are defined as those with an absolute volumetric strain exceeding 1.5% at any moment in the cardiac cycle.

The boxplots in Figure 3a represent the relative distributions of the high strain voxels within the ROIs. The large fractional volumes observed for all ROIs in the patient group signifies that their altered high strain energy is a large-scale effect which occurs throughout the cerebrum. Incorporating the results from both subject groups indicates a slight predisposition of the high strains occurring in the GM vs NAWM ROIs. The occurrence percentage of the high strains in the GM and WB ROIs is generally larger in the controls than for the patients (both using the same threshold of 1.5%), despite the lower volume fraction in the control group. Interestingly, in the patient group the high strains occur more often in the NAWM tissue than for the controls. There also appears to be a general shift towards a higher occurrence of high strain voxels in the WMH ROI, in comparison to the WMH_R ROI in controls.

Finally, we plot the average value of the volume representing the high strain voxels as a function of time to gain insight on its source from the waveform shape. In our DENSE implementation, we utilised ramped flip angles to provide constant SNR overtime[7,8]. Thus, if noise predominantly influenced the generation of high strain voxels, then the resulting waveform would also be appreciably noisy. We instead observe a waveform with characteristics akin to the volumetric strain when the high strain voxels are excluded from the analysis. This is suggestive that the high strain voxels predominantly have physiological origin.

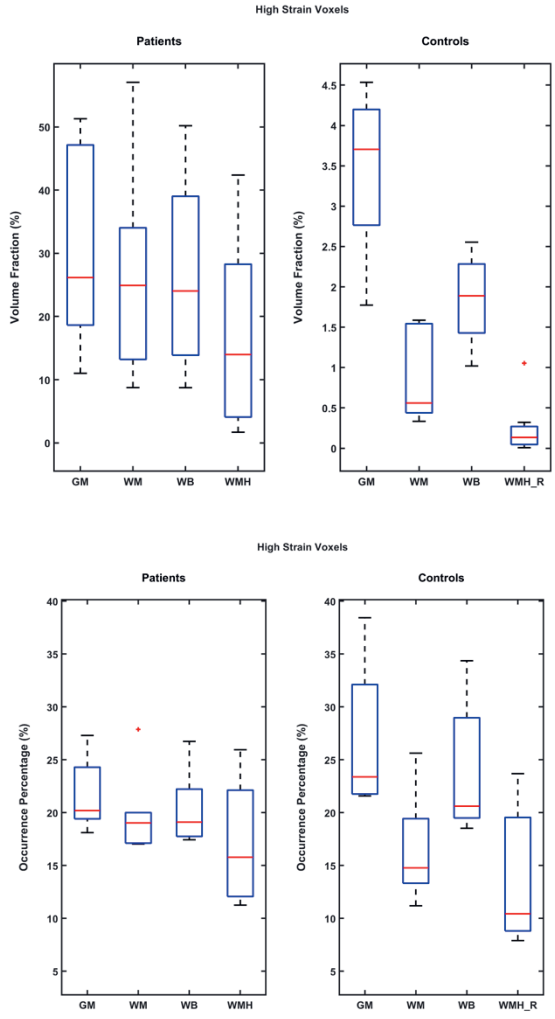

Figure 3. Boxplots of the total high strain voxel volume as a fractional percentage of the ROI volume. The occurrence percentage as a function of ROI is also shown for the patient and control groups. The occurrence percentage was derived from the number of occurrences of high strain voxels in the respective ROI over the cardiac cycle. The boxplot whiskers represent the 2.7 sigma limit. Note the different scaling for the controls for the volume fraction.

The high strains for the patient GM ROIs contribute a rapid exchange of expansive and compressive strains during the period associated with systole, which leads to a net compressive effect for the remainder of the cardiac cycle, and a slow return to baseline during diastole. The GM ROI strain behaviour is different to the other patient ROIs, and implies existence of a mechanism in the GM ROI which quickly blocks the high, expansive strains.

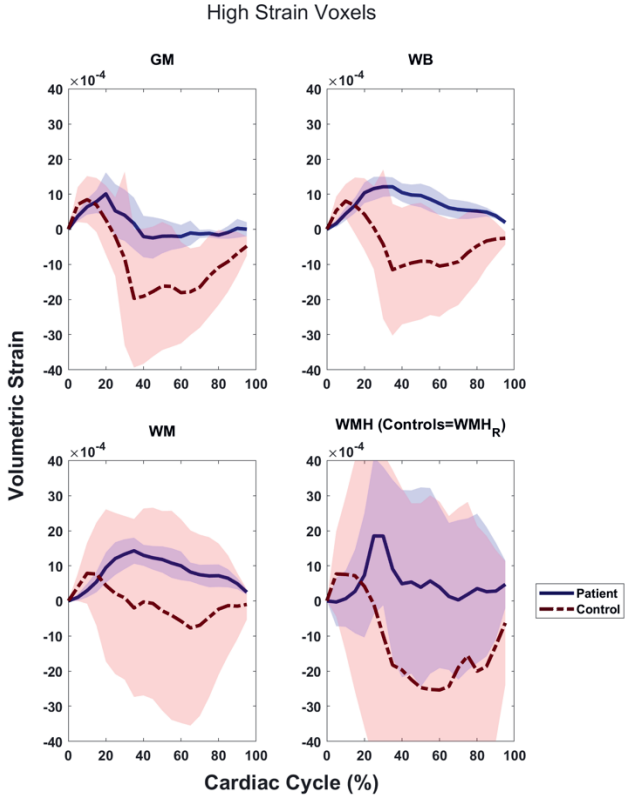

Figure 4. Group mean high strain curves for ROIs, representing the larger strain energies observed over the cardiac cycle, beginning at systole. Shaded regions reflect the group mean standard deviation.

Across the ROIs for the controls, the volume associated with the high strains rapidly expand during early systole, however well before end-systole they begin to experience net compressive strain energies for the remainder of the cardiac cycle. This is interpreted as a volume change induced primarily from the venous compartment of the vasculature, which may still accommodate a brief expansion during systole, and then compress early due to their high compliance around the expanding tissue. In this case, the compression is made possible by blood volume leaving the venous vasculature. We conclude that the net effect of the high strains over the cardiac cycle in patient group is expansion, while in the control group the net effect is compression.

Summary of the High Volumetric Strain Observations

1. A larger volume of high strains voxels is present in the patient group than in the controls. Their inclusion also predominantly affects the patient group results.
2. High strain voxels appear to have an approximately uniform distribution throughout the cerebrum, although there is a slightly lower presence in the NAWM ROI.

3. For a given voxel, a high strain occurs more often per cardiac cycle in the control group than in the patient group for the GM and WB ROIs. For the NAWM ROI, high strains occur more often in the patient group.
4. NAWM peak strains are altered more (increase) than GM by the inclusion of high strain voxels
5. The waveform of the high strain voxels has shape characteristics akin to those derived from brain tissue.
6. In the patient group, the net effect of the high strain voxels over the cardiac cycle is expansion. In the control group, the net effect is compression.

The GM ROIs have the largest fraction of high strain voxels, and high strain activity occurs more often per cardiac cycle in this ROI. Despite their larger presence and frequency of occurrence in GM, the largest change in volumetric strain when including the high strains is observed in the patient NAWM ROI. Cortical GM is expected to have a slightly higher spatial SNR due to closer proximity to the receiver coil than the deeper NAWM[8]. Under the assumption that the high strain voxels primarily reflect noise it would be expected to observe a greater distribution in the NAWM ROIs than GM, however we observed the reverse effect. These facts, together with the general shape of the high strain energy waveforms strongly hints at a physiological signal contained in the high strain energies, instead of just noise.

Finally, due to the different data distributions in the patient and control groups, we likely select for strain contributions from different tissue/vascular compartments in both groups by enforcing the fixed threshold value of 1.5%. This likely explains the vastly different waveforms of their mean value over the cardiac cycle. This, in combination with the suggested physiological source for the higher strains may imply the need for a normalization parameter, which would allow fairer comparisons of the brain tissue volumetric strain between different cohorts, or disease states. While a parameter which is intrinsic to the displacement or strain measurements would be ideal, parameters derived from extra (same-session) measurements such as intracranial pressure[9] could prove useful for this purpose.

4. Conclusion

Despite not yet fully understood, the high strain energies have greater prominence, and relative effect on the patients than in the controls. In our patient cohort, their net effect over the cardiac cycle is expansion, while in healthy controls the net effect is compression. The varied presence (and occurrence over the cardiac cycle) of high strain energy across the ROIs, along with the mean waveform shape hints to a physiological signal at the root of the high strains, rather than simply noise. The high expansive strains maybe be attributed to a reduction in the dampening capacity of the larger, stiffer vessels according to the pulse wave encephalopathy hypothesis, which leads to higher pulsatile energy transmitted to the cerebral microvasculature.

References

1 Adams AL, Viergever MA, Luijten PR, Zwanenburg JJM. Validating faster DENSE measurements of cardiac-induced brain tissue expansion as a potential tool for investigating cerebral microvascular pulsations. *Neuroimage* 2020; **208**: 116466.

2 Farokhian F, Yang C, Beheshti I, Matsuda H, Wu S. Age-related gray and white matter changes in normal adult brains. *Aging Dis* 2017; **8**: 899–909.

3 Heier LA, Bauer CJ, Schwartz L, Zimmerman RD, Morgello S, Deck MDF. Large Virchow-Robin Spaces: MR-Ciinical Correlation. .

4 Potter GM, Doubal FN, Jackson CA, Chappell FM, Sudlow CL, Dennis MS *et al.* Enlarged perivascular spaces and cerebral small vessel disease. *International Journal of Stroke* 2015; **10**: 376–381.

5 Riba-Llena I, Jiménez-Balado J, Castañé X, Girona A, López-Rueda A, Mundet X *et al.* Arterial stiffness is associated with basal ganglia enlarged perivascular spaces and cerebral small vessel disease load. *Stroke* 2018; **49**: 1279–1281.

6 Wardlaw JM, Smith EE, Biessels GJ, Cordonnier C, Fazekas F, Frayne R *et al.* Neuroimaging standards for research into small vessel disease and its contribution to ageing and neurodegeneration. Lancet Neurol. 2013; **12**: 822–838.

7 Adams AL, Kuijf HJ, Viergever MA, Luijten PR, Zwanenburg JJM. Quantifying cardiac-induced brain tissue expansion using DENSE. *NMR Biomed* 2019; **32**: e4050.

8 Adams A, Sloots J-J, Luijten P, Zwanenburg J. SNR analysis of retrospectively gated DENSE at 7T for the measurement of brain tissue pulsatility. In: *Proceedings of the 26th Annual Meeting of ISMRM*. ISMRM: Paris, 2018, pp 2874–2874.

9 Alperin NJ, Lee SH, Loth F, Raksin PB, Lichtor T. MR-Intracranial pressure (ICP): a method to measure intracranial elastance and pressure noninvasively by means of MR imaging: baboon and human study. *Radiology* 2000; **217**: 877–85.

Chapter 5

Quantitative comparison between aMRI and DENSE for the assessment of brain tissue motion

This chapter is based on the research article currently available as a preprint on bioRxiv: Adams, A. L. Terem, I., Champagne, A., Holdsworth, S. J., & Zwanenburg, J. J. M. (*2023*). *Quantitative comparison between aMRI and DENSE for the assessment of brain tissue motion*. bioRxiv, 2023.01.24.525340.

.

Abstract

Purpose
Amplified MRI (aMRI) holds potential for assessing brain tissue motion and strain, using images acquired from readily-available sequences. However, image registration is necessary to extract displacements from the motion-amplified images, which may limit its accuracy. We aimed to separately assess the errors from imperfections in the aMRI amplification, and errors from the registration algorithm, using a semi-synthetic approach.

Method
Ground truth brain tissue motion was derived from smoothed Displacement Encoding with Stimulated Echoes (DENSE) measurements acquired at 7T (8 subjects). Those were then applied to a still sagittal anatomical balanced-SSFP image to obtain a DENSE-animated MRI series to which aMRI (amplification factor 10) was applied. DENSE-amplified MRI series served as a reference (Damp-MRI; amplification factor, 10). Amplified displacements were extracted from aMRI and Damp-MRI using a common registration algorithm. Linear regression was used to estimate the amplification and r^2 agreement of the amplified displacements relative to the ground truth.

Results
The estimated amplification was consistently lower for aMRI-derived displacements (range: [4.9±0.3 5.7±0.3]) than for Damp-MRI measurements (range: [6.7±0.5 7.7±0.5]). Nevertheless, the spatial, temporal and average characteristics of brain tissue motion derived from aMRI were comparable to the ground truth for Anterior-Posterior and Feet-Head displacements: (group averaged $r^2 \geq 0.84$), as were the Damp-MRI derived displacements ($r^2 \geq 0.88$). When aMRI was applied to in-vivo cine-bSSFP images and compared to the ground truth, the results were less favorable, highlighting the need for artefact-free images.

Conclusion
These results strengthen the potential of aMRI as a tool for semi-quantitative assessment of brain tissue motion in disease.

1. Introduction

Brain tissue exhibits cardiac-induced pulsatile displacement which may be altered after injury or disease[1–4], providing a potential mechanism to better understand the pathological mechanisms underlying these diseases. Additionally, brain tissue strain is derivable from tissue displacement fields[5–7], which may provide insights into diseases that affect the (visco)elastic properties of brain tissue, or the cerebral small vessels which act as a conduit for cardiac-induced brain tissue strain[8]. Displacement Encoding with Stimulated Echoes (DENSE)[5,9,10] and amplified MRI (aMRI)[11,12] have the sensitivity to discern the subtle displacements which are associated with brain tissue motion. DENSE encodes displacements in the phase of the MR signal, thereby providing access to measurements of sub-voxel tissue motion. DENSE may therefore be considered as a method that provides quantitative ground truth displacements of brain tissue motion, although it is currently limited with respect to its clinical availability. aMRI, which enables the visualization of brain tissue motion, can be used to estimate the displacement fields through a post-processing amplification algorithm applied on conventional cine-images, which yields a great potential for assessing pulsatile brain tissue motion on clinically available scanners with readily available sequences.

Despite recent advances in amplified-based motion imaging[11,12], the aMRI algorithm yields only the deformed images, and not the displacement fields. Thus, image registration is necessary to quantitatively assess displacements originating from the amplified motion images generated by aMRI, which potentially limits its accuracy for quantitative estimations of brain tissue motion. Additionally, the accuracy of the registration algorithm may be further dependent on tissue contrast and image noise and artefacts, possibly adding to the limitations of aMRI. For those reasons, a direct comparison of the displacements derived from DENSE and aMRI is challenging since it is inherently biased by the confounding errors introduced during image registration. Moreover, accurate quantification of tissue strain within an imaging plane critically depends on good estimation of the amplification factor applied to the two orthogonal components of the 2D displacement field extracted from the registration. This introduces an additional variable that affects the strain calculation, which in itself is already inherently noise-sensitive. Altogether, this provides grounds for the independent assessment of errors introduced by the registration process and the aMRI post-processing, as an avenue to advance the use of amplification algorithms in clinical settings, while having a thorough understanding of its limitations.

In this study, we aimed to separately assess the errors induced by image registration limitations, and by potential imperfections in the aMRI amplification algorithm for quantitative assessment of brain tissue motion. This was done by using a semi-synthetic approach, where a common registration algorithm was used to extract displacements from both aMRI and DENSE-amplified images of brain tissue, which were then compared against

a known ground truth. We further utilized these displacement measurements to calculate brain tissue strain parameters, as an additional sub-analysis for comparing the results from aMRI.

2. Methods

The assessment of potential errors induced by the aMRI algorithm was performed on both a semi-synthetic dataset and an in-vivo dataset. An overview of this assessment is as follows. First, a description of the acquired images, and post-processing of these measurements is provided since these were used to create the data necessary to perform the semi-synthetic analysis. Secondly, the generation of the semi-synthetic dataset is described in depth. Finally, the details of the analysis performed on all the datasets is supplied. Figure 1 contains an overview of the processing steps.

2.1 Acquired measurements

A 7T MR scanner (Achieva, Philips Healthcare, Best, The Netherlands) with a 32 channel head coil (Nova Medical, Wilmington, USA) was used to acquire 4D DENSE images with Feet-Head (FH), Anterior-Posterior (AP) and Right-Left (RL) motion encoding directions. Images were acquired as previously described[6] in 8 healthy subjects of European descent (5 males, mean age: 27±6 years) to extract whole brain tissue displacements covering the entire cardiac cycle. In brief, the following parameters were used: FOV=250x250x190 mm^3, resolution=1.95x1.95x2.2 mm^3, motion sensitivity=0.7 mm/2pi (FH) and 0.35 mm/2pi (AP and RL), temporal resolution=51 ms. The scan duration was 3x2.4 min for a heart rate of 60 bpm, for the three orthogonal motion encoding directions (FH, AP and RL).

2D mid-sagittal (10-20 mm left/right from the interhemispheric fissure) balanced-SSFP (bSSFP) cine-images of all subjects were acquired in the same scan session as the DENSE images, using the following imaging parameters: FOV=240x240 mm^2, resolution=0.83x0.83x3 mm^3, TR=4.1 ms, TE=2 ms, EPI factor=5 (to achieve a high temporal resolution which is desirable for the aMRI algorithm), number of averages=4, flip angle=20°, cardiac synchronization device=pulse oximeter. The total number of reconstructed cardiac frames was 80, for a total acquisition time of approximately 4 minutes. These bSSFP images served as the in-vivo dataset.

A high-resolution T1-weighted image (FOV=300x248x190 mm^3, resolution=0.93x0.93x1 mm^3, TR=4 ms, TE=2 ms, inversion delay=1235 ms, flip angle=5°) was also acquired for all subjects for registration of the processed images in anatomical space.

The governing Ethical Review Board of our institution approved the use of human subjects in this study. Subjects were instructed to lie still in the scanner, and further had their head motion restricted through the use of padding in the transmit/receive head coil.

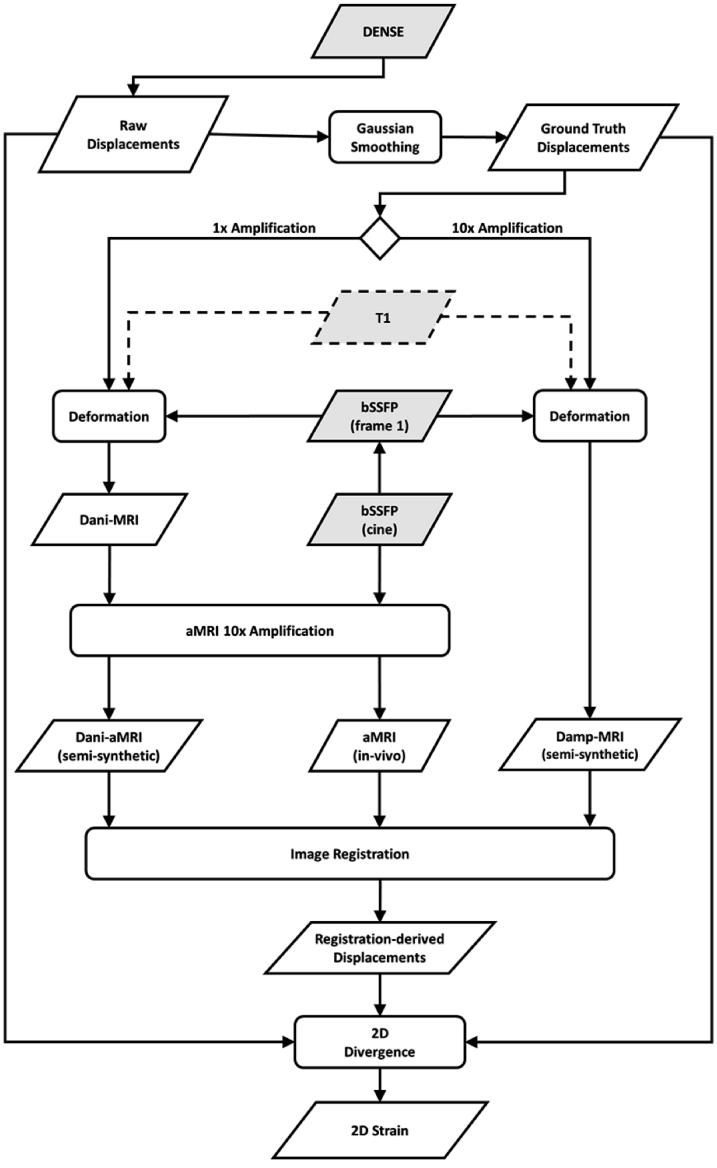

Figure 1. Schematic representation of the processing steps and experiments performed in this study. aMRI = Amplified-MRI, Dani-MRI = DENSE animated MRI, Dani-aMRI = DENSE animated aMRI, Damp-MRI = DENSE amplified MRI. The DENSE, T1-weighted and bSSFP (shaded in blue) were acquired MR images whilst the aMRI, Dani-MRI, Dani-aMRI and Damp-MRI were created using post-processing algorithms. Comparison of Dani-aMRI (registration-derived) displacements and Damp-MRI (registration-derived) displacements to the ground truth displacements allowed for the separate investigation of the errors induced by the registration and aMRI algorithm.

2.2 Post-processing

2.2.1 DENSE

For each subject, the AP and FH DENSE images were first rigidly registered together to correct inter-scan subject motion (with 6 degrees of freedom), and then non-rigidly registered to the T1-weighted image (T1w), resulting in interpolated high-resolution (1 mm isotropic) DENSE images. Registration of the DENSE images with each other, and with the T1w, was performed using the open-source software Elastix[13]. DENSE measurements were temporally adjusted to reflect displacements with respect to end-diastole as reference (vectorcardiogram triggering), instead of at peak-systole (pulse-oximeter triggering). To achieve this (as fully described in Adams et al.[6]), the data were circularly shifted on the time dimension by approximately 250 ms (rounded to an integer number of frames). Subsequent offsets in the displacements were corrected such that displacements at the beginning of the cardiac cycle were zero.

2D ground truth displacements (GTD) were created by spatially smoothing the AP and FH DENSE displacements associated with the same spatial location as the acquired bSSFP images. Smoothing was performed with a Gaussian filter (kernel=21x21 pixels, sigma=3.5). Noise reduction by Gaussian smoothing was found to be a viable method for improving precision, while reducing bias in DENSE measurements[14]. Displacement values outside the brain tissue mask were set to zero before smoothing. The percentage error of the smoothed displacements was determined and found to be small relative to the peak absolute displacement (Figure 2).

2.2.2 Cine-bSSFP

To facilitate creation of the semi-synthetic data, it was desirable to have the bSSFP images in the same image space as the interpolated high-resolution DENSE. Therefore, 2D mid-sagittal slices were extracted from the high-resolution 3D T1w, at the same spatial locations as the bSSFP images. The bSSFP images were then rigidly registered and transformed to the 2D mid-sagittal T1w space. Registration was performed on the first frame of the bSSFP cine images to obtain the rigid transformation parameters, which were then used to transform all subsequent frames to the T1w anatomical space.

High-frequency artefacts were observed in the bSSFP images (Figure 3). As the aMRI amplification and image registration algorithms are sensitive to intensity fluctuations, the high-frequency components were suppressed using a minimum order, infinite impulse response low-pass filter with a cut-off frequency of 3Hz.

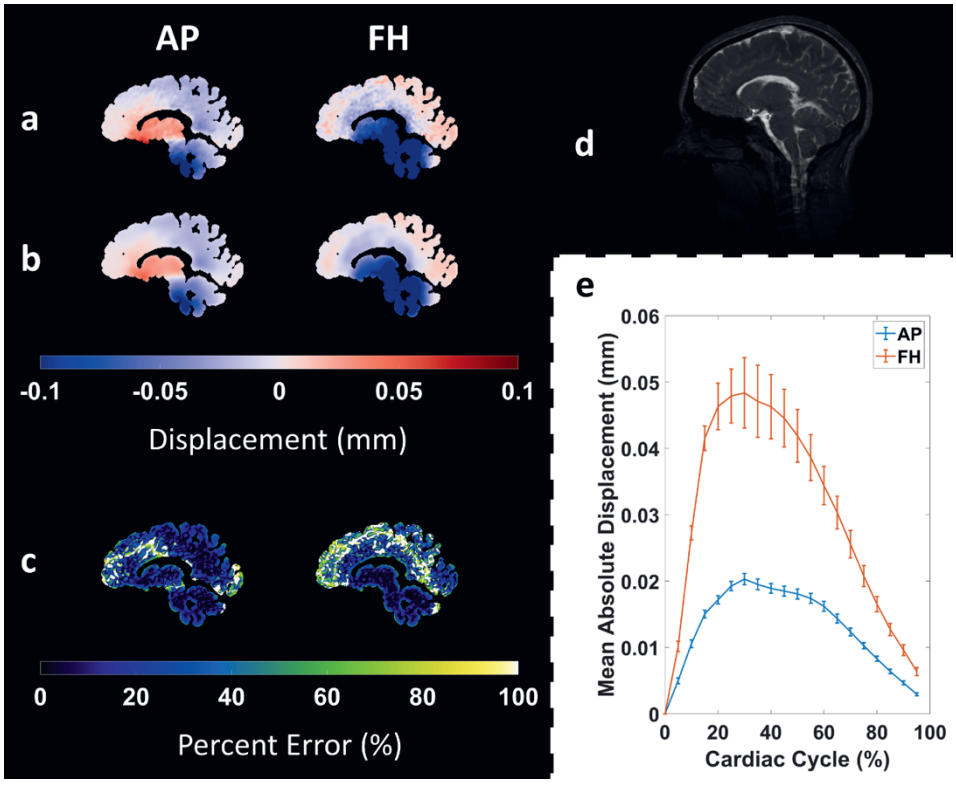

Figure 2. Example AP and FH raw displacements (a) and smoothed ground truth displacements (b) from one subject. Percentage error maps between the raw and smoothed displacements are shown in (c). All maps are shown at the moment of peak displacement for the subject. (d) Reference bSSFP anatomical image. The mean (within the brain tissue) group mean absolute AP and FH 'raw' displacements over the cardiac cycle is shown in (e). Error bars represent the group mean absolute difference between the raw and smoothed displacements.

2.2.3 Tissue masks

Brain tissue masks were generated by performing automatic tissue segmentation using the Computational Anatomy Toolbox (Jena University Hospital, Departments of Psychiatry and Neurology) in SPM12 (Wellcome Trust Centre for Neuroimaging, University College London). Voxels containing only CSF, or partial-volumed with CSF (as determined by the segmentation software) were removed from the brain tissue masks. Regions containing DENSE artefacts were further excluded from the brain tissue masks using an SNR threshold as previously described[6].

2.3 Semi-synthetic dataset

Synthetic data were necessary to untangle the combined errors induced by the aMRI and registration algorithms. To create a test environment with realistic brain tissue motion, the DENSE measurements were used to create a synthetic dataset (hereafter referred to as semi-

synthetic data). This was accomplished as follows: the displacement fields obtained through DENSE were used to deform ('animate') a reference image, thereby providing an animation of the tissue motion over the cardiac cycle. The first frame of the bSSFP acquisition was selected as the reference image, which was deformed using the GTD. The resulting dataset is termed as DENSE-animated images (Dani-MRI). DENSE-amplified images (Damp-MRI) were similarly created by linearly scaling the GTD by a factor of 10 and then using the scaled GTD to deform the bSSFP reference image.

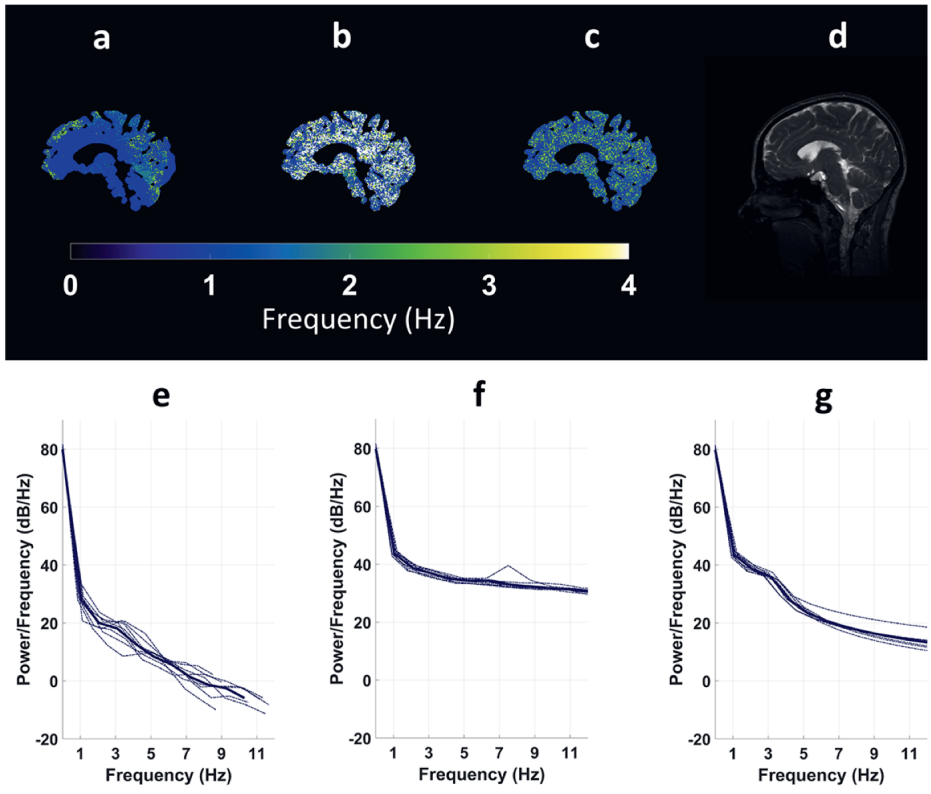

Figure 3. Example max power frequency maps for Dani-MRI (a), the unfiltered in-vivo-aMRI (b) and the low pass filtered in-vivo-aMRI (c). Reference magnitude image is shown in (d). The mean power (with the brain tissue) at different frequencies for the Dani-MRI, the unfiltered in-vivo-aMRI and low-pass filtered in-vivo-aMRI in all subjects is shown in e,f and g, respectively. The bold line signifies the group mean value.

2.4 Analysis

The following analysis steps were performed on the semi-synthetic and in-vivo datasets.

2.4.1 Phase-based amplification

The phase-based aMRI algorithm[12] was used to amplify the motion in the Dani-MRI and the in-vivo bSSFP cine-images. For clarity, we term the amplification of Dani-MRI and in-vivo bSSFP images with aMRI as Dani-aMRI and in-vivo-aMRI, respectively.

aMRI takes as an input a time series of MR images, and outputs images with magnified motion. The main idea behind aMRI is that the motion field is not explicitly estimated, but rather magnified by amplifying temporal intensity changes at a fixed position. Magnification is achieved by decomposing the series of MR images into scale and orientation components using a linear complex-valued steerable pyramid. Temporal variations in the phase of the coefficients of the complex-valued steerable pyramid correspond to motion and can be temporally processed and amplified to reveal imperceptible motion, or attenuated to remove distracting changes.

The original aMRI algorithm[12] enables one to selectively amplify different temporal frequencies, with different amplification factors depending on the physiological information of interest. In addition, an optional amplitude-weighted Gaussian spatial smoothing can be performed on the filtered phases, in order to increase the phase SNR and support a larger amplification factor. In this study, we wanted to quantify and compare the overall motion, while avoiding noise from higher temporal frequencies which existed in the in-vivo bSSFP data. As such, in addition to the low-pass filtering applied on the cine-bSSFP images, we also chose to selectively amplify motion within the range of 0-3 Hz. The use of a cardiac-gated acquisition ensured that most energy was concentrated within this range[12]. Additionally, in order to avoid the loss of motion information, and also perform a better comparison between the Dani-aMRI and Damp-MRI images, we did not apply the optional amplitude-weighted Gaussian filter on the filtered phases.

Using the displacement function $\delta(t)$ and spatial wavelength λ, the amplification parameter α was bounded in the original phase-based study[15] as $\alpha\delta(t) < \frac{\lambda}{4}$ for the regular octave complex steerable pyramid, and $\alpha\delta(t) < \frac{\lambda}{2}$ for the sub-octave complex steerable pyramid. In order to support a larger amplification factor, we decided to use the sub-octave steerable pyramid representation. We tested the sub-octave steerable pyramid with a number of orientations (4, 8, and 16). From this internal analysis, we concluded that the registration algorithm performed best on the sub-octave complex steerable pyramid with 16 orientations filters. We also empirically determined that $\alpha = 10$ generated sufficient amplification to enable accurate registration with minimum artefacts and distortions, and therefore utilized $\alpha = 10$ for the analyses conducted in this study.

2.4.2 Retrieval of amplified displacements and strain

Extraction of the amplified brain tissue displacement maps from the Damp-MRI and aMRI was achieved using deformable image registration. The domain of deformable image registration algorithms is vast; an excellent overview for medical applications is provided by Sotiras et al.[16]. Given the extensive choices available, we selected the registration algorithm developed by Metz et al.[17], which was designed for our application (i.e., motion estimation in dynamic medical images). The registration algorithm capitalizes on the following data characteristics/assumptions to extract displacements with sub-voxel accuracy:

1. The data contains a series of images acquired over a short duration in one scan session. Therefore:
    a. Monomodal image registration can be performed using a simple dissimilarity metric involving image intensities. The algorithm by Metz et al. minimizes the temporal intensity variance to implicitly align the images to an average reference frame.
    b. A group-wise registration approach can be performed, which simultaneously aligns all images in the series. Metz et al.[17] and Ledesma-Carbayo et al.[18] both demonstrated that this approach reduces errors in comparison to the pairwise registration approach, wherein each frame of the image series is registered independently to a chosen reference, or consecutively to a neighboring frame. The group-wise approach utilizes information in all images for the registration (leading to a more robust optimization) and also avoids the need to choose a reference frame, which avoids the bias associated with registering to the reference[19,20].
2. The motion contained in the data series has a physiological source, where the following characteristics are assumed:
    a. The physiological displacements were temporally smooth. For the semi-synthetic approach, the reconstructed temporal resolution of the DENSE data is approximately 51 ms, whereas the in-vivo experiment was achieved using a temporal resolution of approximately 13 ms)
    b. The displacement fields were spatially smooth. For the semi-synthetic analysis, spatial smoothness was enforced by the smoothing of the DENSE data during the creation of the GTD. For the in-vivo experiment, the analysis was limited to displacements within the brain tissue to reduce the impact of potential discontinuities at the tissue-CSF border.
    c. The displacements were temporally cyclic. For both the semi-synthetic and in-vivo experiment, cyclic displacements were enforced by the retrospectively-gated acquisition which was synchronized to the cardiac output.

Extraction of displacements exhibiting spatio-temporal smoothness and cyclic behavior (as described in point 2 above) was achieved in the registration algorithm through the use of a cyclic b-spline transformation model, where the first and last control points on the temporal axis were neighbors[17].

Registration was performed using Elastix. A multiresolution approach, where the image complexity is reduced by downsampling, or smoothing, can be used to improve registration success. However in this study, we opted to only alter the transformation complexity per resolution, which conserves as much image information as possible for the cost function. This was done by altering the b-spline grid spacing per resolution (in voxels, for [x, y, t]) = [20, 20, 2; 12, 12, 1], where x, y and t denote the 2D and time dimensions. The number of iterations per resolution was set to 1000.

Spatial and temporal sampling was performed to reduce computational complexity. Temporal sampling had the additional benefit of limiting the impact of image artefacts on registration accuracy. Spatial sampling was constrained to voxels within the brain tissue mask. The number of spatial and temporal samples per iteration was set to 2000 and 20, respectively. For the semi-synthetic analysis the use of 20 temporal samples per iteration corresponded to using all available frames in every iteration, whereas for the in-vivo analysis this corresponded to ¼ of all available frames per iteration. The temporal resolution of the in-vivo registration-derived displacements was downsampled to match the GTD resolution. An average displacement curve for the amplified and ground truth displacements was found by calculating the average displacement within the brain tissue mask for each frame of the cardiac cycle.

2D strain maps were created from the Damp-MRI and aMRI displacement maps, as well as from the GTD, by calculating the 2D divergence of the amplified and ground truth displacements within the brain tissue masks. For each frame, the average strain within the brain tissue mask was calculated, yielding an average tissue strain curve covering the entire cardiac cycle.

2.4.3 Estimation of the amplification factor and measurement agreement

Linear regression was used to estimate the amplification factor (regression slope) and goodness of fit (r^2) between Damp-MRI derived displacements and the GTD, and also between aMRI-derived displacements and the GTD. For the in-vivo-aMRI, the unsmoothed DENSE measurements were used as the ground truth displacements. To better assess the spatial, temporal and average characteristics of the displacement maps, the linear regression analysis was performed in the following 3 ways:

1. *Between the spatial pattern of the amplified and ground truth displacement maps, for each cardiac frame*.
   We define the resulting estimated amplification and goodness of fit of this spatial linear regression analysis as EA_s and r_s^2, respectively. To obtain EA_s and r_s^2, linear regression was first performed on a per frame basis, between voxels in the brain tissue mask of the amplified displacement and GTD maps to determine *f*, the line of best fit. EA_s was then defined as the slope of *f*. Secondly, r_s^2 was calculated (also on a per frame basis) as shown in Eq. [1], where AD_i is the Damp-MRI or aMRI-derived displacement in the i^{th} voxel within a brain tissue mask consisting of n voxels. SSr and SSt are the total sum of squares of residuals and the total sum of squares, respectively.

$$r^2 \stackrel{\text{def}}{\equiv} 1 - \frac{SSr}{SSt} = 1 - \frac{\sum_{i=1}^{n}(AD_i - f_i)^2}{\sum_{i=1}^{n}(AD_i - \frac{1}{n}\sum_{i=1}^{n} AD_i)^2} \quad \text{Eq. [1]}$$

   Thus, EA_s and r_s^2 curves could be constructed, respectively reflecting the estimated amplification and spatial agreement of the amplified displacements to the GTD for each frame of the cardiac cycle.

2. *Between the amplified and ground truth temporal displacement curves.*
   The estimated amplification and goodness of fit obtained from this temporal regression is defined as EA_t and r_t^2, respectively, and available for each voxel within the brain tissue mask. EA_t and r_t^2 maps were constructed through linear regression of the displacement curve of each voxel in the amplified displacement and the GTD maps. In the EA_t and r_t^2 maps, each voxel represented the estimated amplification and agreement of the amplified displacements at that spatial location over the cardiac cycle, relative to the GTD. For each subject, the mean EA_t and r_t^2 within the brain tissue mask was calculated.

3. *Between the average displacement curves calculated from the amplified and ground truth displacement maps*.
   The estimated amplification and goodness of fit obtained from this regression is defined as EA_a and r_a^2, respectively. To calculate EA_a and r_a^2, the average AP and FH displacement within the tissue mask was found for each frame of the cardiac cycle, yielding average AP and FH displacement curves for each subject. Linear regression was then performed between the average displacement curves of the Damp-MRI and GTD, and between those of the aMRI and GTD. From this regression, EA_a and r_a^2 was determined for the AP and FH displacements of each subject.

For all regression analyses, the y-intercept was not forced to zero. The simple percentage error of the Damp-MRI, Dani-aMRI and in-vivo-aMRI amplified displacements relative to the ground truth was also calculated. The percentage error was calculated as $\frac{100*|D_a - D_{gt}|}{|D_{gt}|}$, where D_a and D_{gt} are the amplified and ground truth displacements, respectively.

A similar analysis as above was performed between the amplified strain maps and the ground truth strain to determine the estimated amplification and goodness of fit, thereby evaluating the spatial, temporal and average amplified 2D strain characteristics relative to the ground truth strain.

2.5 Through-plane motion analysis

With the semi-synthetic dataset, the performance of aMRI and the registration algorithm under different scenarios was explored. Specifically, the impact of through-plane brain tissue motion on the performance of aMRI and the registration algorithm was investigated. The influence of contrast on the registration algorithm was also investigated by utilizing 2D T1-weighted (T1w) images as the reference images, which were deformed by the DENSE, creating T1w Dani-MRI and T1w Damp-MRI (see Figure 1). The investigation of through-plane motion provides further insight on the errors observed in the in-vivo analysis.

To investigate the influence of through-plane motion and image contrast on the performance of aMRI and the registration algorithm, semi-synthetic datasets containing T1w contrast were created by first Gaussian smoothing the RL, AP and FH DENSE measurements (kernel = 11 x 11 x 11 voxels, sigma = 1.8), which served as the 3D ground truth displacements (GTD). The smoothed displacements were used to deform the 3D T1w image. 2D slices of the deformed 3D T1w images were then extracted from the same spatial locations as bSSFP acquisitions (section 2.2.2), yielding mid-sagittal 2D DENSE animated MRI (Dani-MRI), which exhibit 3D brain tissue motion over the cardiac cycle. DENSE amplified MRI (Damp-MRI) were created by linearly scaling the 3D GTD by a factor of 10 and then using the scaled GTD to deform the 3D T1w. As with the Dani-MRI, 2D mid-sagittal slices were subsequently extracted. As a reference, the same steps were repeated with the RL displacements set to zero, allowing the influence of through-plane motion to be investigated. The analysis steps detailed in section 2.4 were performed and the results summarized in Table 2 below. Figure 9 contains example images showing influence of amplified RL through-plane motion on the sagittal images.

2.6 Statistics

Student's *t*-tests (paired, 2 tails) were used to assess differences between the estimated amplification and goodness of fit of Damp-MRI and Dani-aMRI derived displacements. Note

that a mismatch between Damp-MRI and GTD selectively reflects errors from the registration only, while Dani-aMRI vs. GTD reflects both registration errors and imperfections of the amplification algorithm used by aMRI. Therefore, differences between the estimated amplification of Damp-MRI and Dani-aMRI highlight imperfections arising solely from the aMRI amplification algorithm.

3. Results

The analysis of Damp-MRI and Dani-aMRI semi-synthetic data, and the in-vivo-aMRI data were successfully completed on all subjects (n=8). Similar tissue amplification patterns were observed between the semi-synthetic and in-vivo datasets.

Example amplified peak displacement maps and curves for the GTD, as well as for the Damp-MRI and Dani-aMRI derived displacements, are shown in Figure 4. This figure shows that the registration extracted similar displacement fields in all cases, but was most limited for the AP displacements of the in-vivo analysis. The percentage errors of the amplified peak displacements relative to the ground truth are displayed in Figure 5.

The group max median percentage errors at peak displacement were (AP, FH, strain): Damp-MRI (44.0%, 44.3%, 81.4%), Dani-aMRI (51.7%, 50.9%, 77.3%), in-vivo-aMRI (145.2 %, 107.2%, 163.9%). Generally, the percentage errors were largest in regions where the ground truth displacements were small.

Figure 6 shows example EA_t and r_t^2 maps reflecting the voxel-wise temporal agreement between amplified displacements and the GTD. For the Damp-MRI, large regions of the tissue showed estimated amplification values close to the correct amplification factor of 10. The estimated amplification in these regions was noticeably lower for the Dani-aMRI. The goodness of fit (r_t^2) between the Damp-MRI and Dani-aMRI was more similar. Figure 6 (c) and (f) show example EA_t and r_t^2 maps from the in-vivo-aMRI analysis.

Figure 7 shows the temporal stability over the cardiac cycle of the EA_s and r_s^2. The results from the Damp-MRI and Dani-aMRI data were similar, with slightly better EA_s and r_s^2 results in the former. This shows that errors introduced by aMRI under ideal conditions are limited.

The results for both are also noticeably worse at the beginning and end of the cardiac cycle, where the brain tissue displacements are lowest. As with the EA_t and r_t^2 analysis, accuracy of the extracted displacements from the in-vivo data was limited. This can be concluded from the lower values and higher inter-subject variability in the r_s^2 in comparison to that revealed in the semi-synthetic analysis.

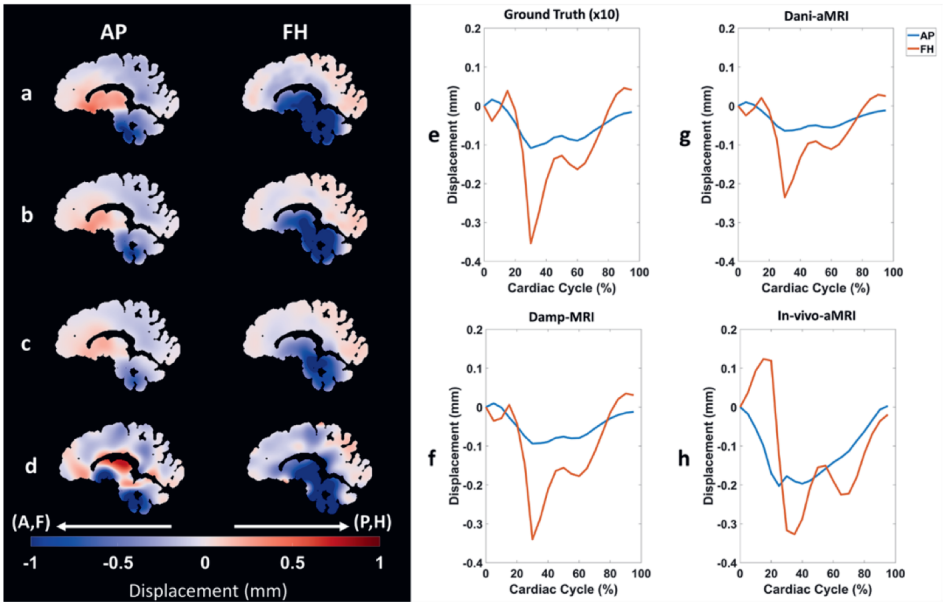

Figure 4. Example AP and FH peak displacement maps derived from Ground Truth (a), Damp-MRI (b), Dani-aMRI (c) and in-vivo-aMRI (d). Ground Truth maps are scaled by 10 to better the fit within the color range of the amplified displacement maps. Maps are shown at the time of peak displacement, relative to triggering at end-diastole. The mean (within the brain tissue) AP and FH displacement over the cardiac cycle for the subject is shown in (e,f,g,h) for Ground Truth (x10), Damp-MRI, Dani-aMRI and in-vivo-aMRI, respectively.

Strain maps and curves calculated from the displacement maps are shown in Figure 8. The amplitude of the peak strain is much lower for the semi-synthetic analysis relative to the ground truth. However, the general shape of the curves were similar. The general trend showing increased divergence during systole, and subsequent relaxation during diastole was also observed in the strain curves derived from the in-vivo-aMRI data. The percentage error of the strain maps relative to the ground truth are also displayed in Figure 5.

Summary results for the group mean estimated amplification and r^2 are listed in Table 1. The estimated amplification of Dani-aMRI was found to be significantly different than those from the Damp-MRI measurements for both AP and FH displacements, as well as the derived 2-D strain ($P \leq 0.05$ in all cases). For the spatial regression analysis, only the FH displacements were not significantly different ($P=0.063$). For the temporal regression analysis, only the strain measurements were not significantly different ($P=0.287$). For the average regression analysis, the AP, FH and strain measurements were found to be not significantly different *(*$P=0.427$, $P=0.146$, $P=0.085$, respectively).

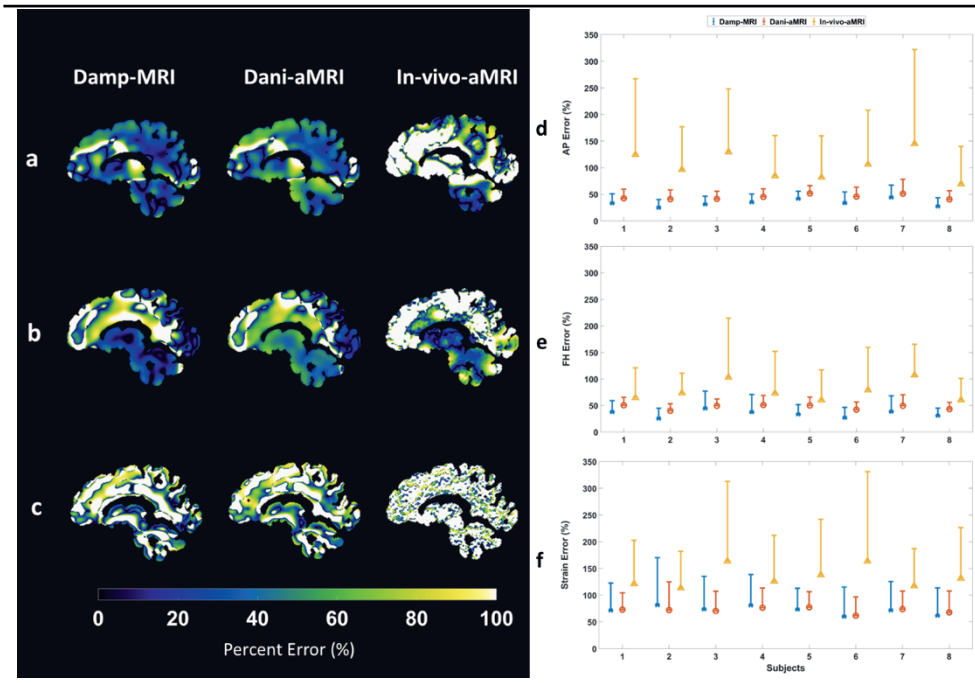

Figure 5 Example AP, FH and strain percentage error maps (a, b, c, respectively) calculated from Damp-MRI, Dani-aMRI and in-vivo-aMRI. Error maps are shown at the moment of peak displacement for the subject. Median percentage error with one-sided interquartile range error bars for AP, FH and strain are plotted for all subjects in d, e, and f, respectively. Percentage error was calculated as $\frac{100*|D_a - D_{gt}|}{|D_{gt}|}$, where D_a and D_{gt} are the amplified and reference displacements, respectively.

		Estimated Amplification (EA)			Goodness of Fit (r^2)		
		AP	FH	Strain	AP	FH	Strain
Damp-MRI	Spatial	6.89±0.62	7.55±0.85	5.77±1.11	0.88±0.03	0.92±0.03	0.52±0.08
	Temporal	6.72±0.46	7.34±0.41	4.84±0.42	0.90±0.02	0.96±0.02	0.58±0.04
	Average	6.89±0.57	7.73±0.48	3.71±1.22	0.97±0.03	0.99±0.01	0.87±0.12
Dani-aMRI	Spatial	4.92±0.29	5.09±0.65	3.30±0.75	0.84±0.04	0.93±0.03	0.49±0.07
	Temporal	5.53±0.29	5.67±0.28	3.56±0.33	0.88±0.02	0.97±0.01	0.57±0.04
	Average	5.44±0.55	5.66±0.36	4.59±0.44	0.96±0.05	0.99±0.00	0.97±0.05
bSSFP-aMRI	Spatial	4.44±1.98	8.54±1.58	0.90±2.06	0.11±0.09	0.59±0.23	0.01±0.02
	Temporal	6.95±2.23	6.43±2.66	0.56±0.84	0.39±0.06	0.50±0.10	0.18±0.03
	Average	5.41±5.51	7.00±3.25	7.21±4.86	0.35±0.28	0.64±0.28	0.56±0.28

Table 1. Group mean estimated amplification (EA) and goodness of fit (r^2) for spatial, temporal and ROI-averaged analyses for the Damp-MRI, Dani-aMRI and in-vivo-aMRI derived displacements/strain. The true amplification relative to the ground truth displacements/strain was 10. Spatial EA and r^2 values are reported at peak displacement (end-systole), which for our measurements corresponds to ~30% of the cardiac cycle.

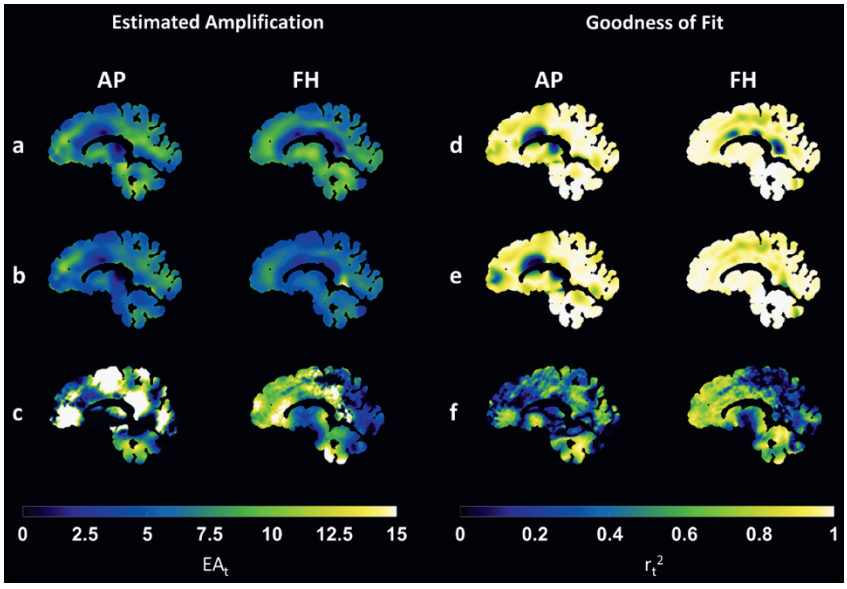

Figure 6. Example Estimated Amplification (EA_t) and Goodness of Fit (r_t^2) maps derived from the temporal analysis of the amplified Damp-MRI (a,d), Dani-aMRI (b,e) and in-vivo-aMRI (c,f) AP and FH displacement maps. In comparison to Dani-aMRI and in-vivo-aMRI, the EA_t maps of Damp-MRI appears generally closer to the expected amplification factor of 10, which is desirable.

		Estimated Amplification (EA)			Goodness of Fit (r^2)		
		AP	FH	Strain	AP	FH	Strain
2D Damp-MRI	Spatial	7.33±0.82	8.34±0.70	4.17±0.84	0.91±0.02	0.91±0.03	0.29±0.07
	Temporal	7.14±0.57	8.16±0.48	3.74±0.82	0.90±0.03	0.96±0.03	0.46±0.07
	Average	7.38±0.44	8.46±0.56	5.18±1.90	0.98±0.01	0.99±0.01	0.96±0.03
3D Damp-MRI	Spatial	6.90±0.94	8.12±0.76	4.05±0.86	0.85±0.08	0.90±0.03	0.28±0.07
	Temporal	7.00±0.91	8.25±0.72	3.65±0.79	0.85±0.04	0.95±0.03	0.45±0.08
	Average	7.45±0.46	8.32±0.54	6.13±2.23	0.97±0.02	0.99±0.00	0.96±0.03
2D Dani-aMRI	Spatial	5.11±0.26	5.18±0.60	2.41±0.53	0.86±0.04	0.90±0.03	0.26±0.06
	Temporal	5.96±0.83	5.06±0.90	2.39±0.73	0.84±0.04	0.81±0.04	0.45±0.08
	Average	5.59±0.53	5.02±1.21	4.38±1.51	0.91±0.03	0.86±0.10	0.96±0.02
3D Dani-aMRI	Spatial	4.99±0.39	5.14±0.66	2.41±0.57	0.82±0.09	0.89±0.04	0.25±0.05
	Temporal	5.90±0.60	5.20±1.21	2.32±0.71	0.80±0.05	0.81±0.04	0.44±0.08
	Average	5.60±0.59	4.98±1.22	4.54±1.49	0.90±0.05	0.86±0.10	0.95±0.02

Table 2. Group mean estimated amplification (EA) and goodness of fit (r^2) for spatial, temporal and ROI-averaged analyses for the Damp-MRI, Dani-aMRI 2D and 3D derived displacements/strain. The true amplification relative to the ground truth displacements/strain was 10. Spatial EA and r^2 values are reported at peak displacement (end-systole), which for our measurements corresponds to ~30% of the cardiac cycle. Please note that the indication of 2D or 3D refers to the motion applied to the synthetic images; the aMRI algorithm is by nature always in 2D, which warrants the analysis of the third, through-plane motion component as performed here.

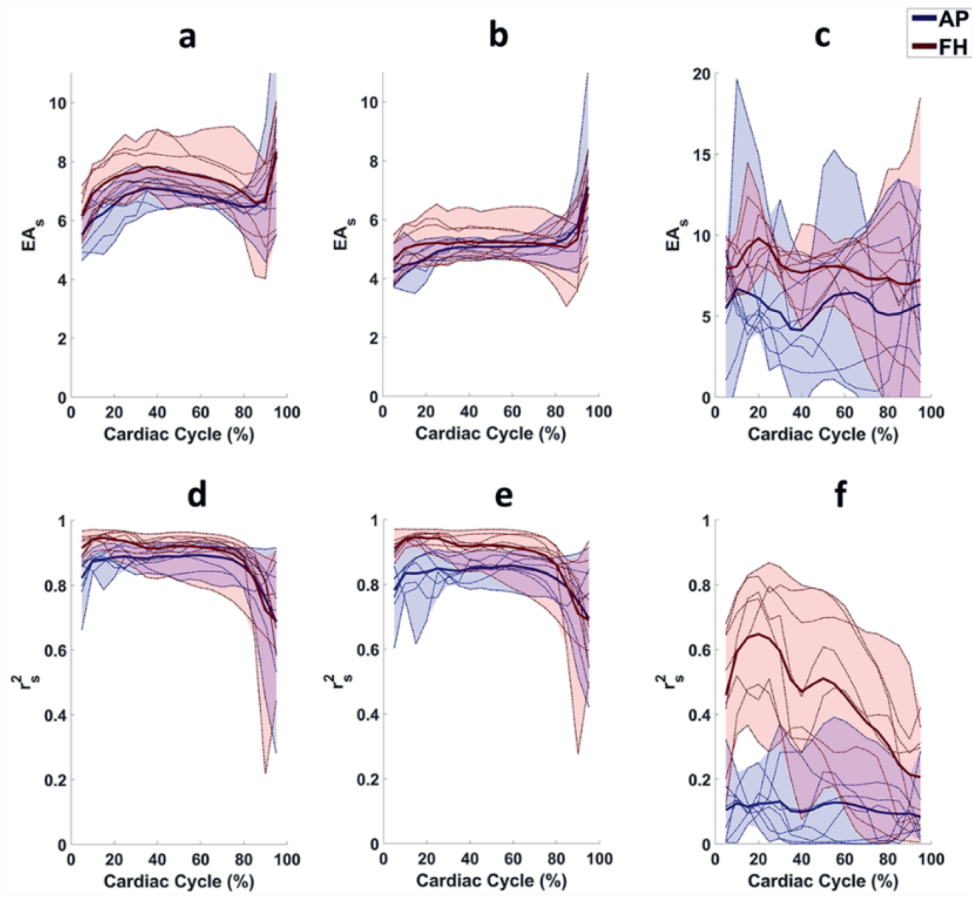

Figure 7. The group mean estimated amplification (EA_s) and goodness of fit (r_s^2) obtained from the spatial analysis for each frame of the cardiac cycle from the Damp-MRI (a,d), Dani-aMRI (b,e), and in-vivo-aMRI (c,f) measurements. The bold red and blue lines represent the group mean value for AP and FH displacements, respectively, whilst the shaded regions reflect inter-subject variability. Displacement offsets resulting from registration were corrected such that the zero displacement coincided with 0% of the cardiac cycle, and is therefore omitted from the plots. The ground truth amplification factor is 10. Note the larger limits used for the y-axis of the in-vivo-aMRI EA_s plots.

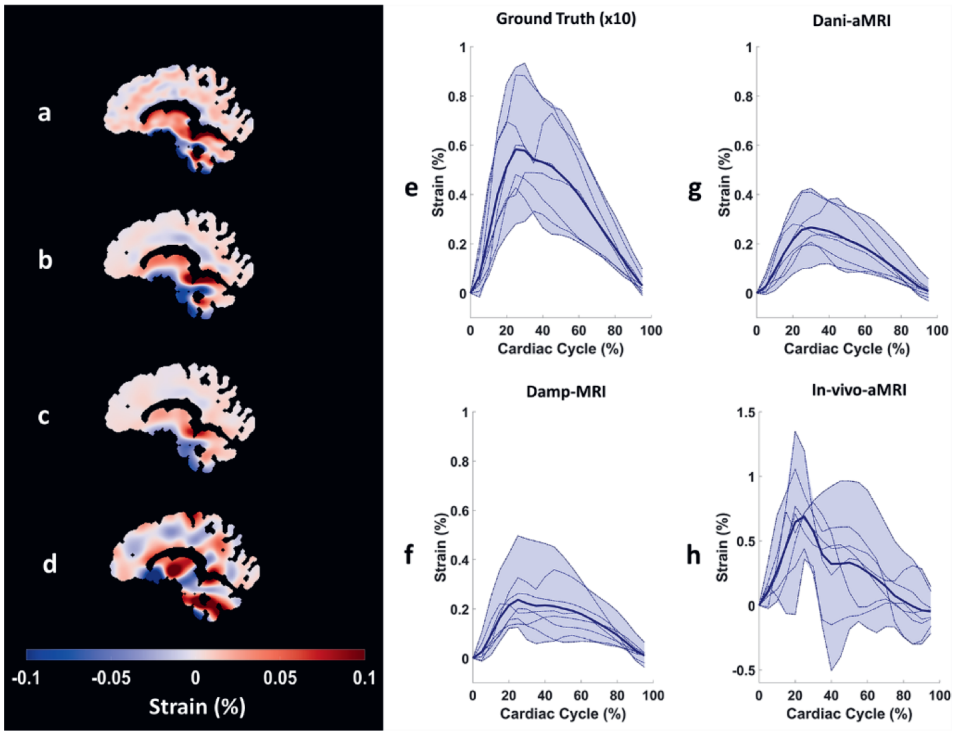

Figure 8. Example peak strain maps derived from Ground Truth (a), Damp-MRI (b), Dani-aMRI (c) and in-vivo-aMRI (d). The Ground Truth map was scaled by 10 to better fit within the color range of the amplified displacement maps. Maps are shown at the time of peak displacement, relative to triggering at end-diastole. The mean (within the brain tissue) strain over the cardiac cycle is shown in (e,f,g,h) for Ground Truth (x10), Damp-MRI, Dani-aMRI and in-vivo-aMRI, respectively. The bold line represents the group mean, and the shaded region the inter-subject variability. Note the larger y-axis limits used for the in-vivo-aMRI strain curves.

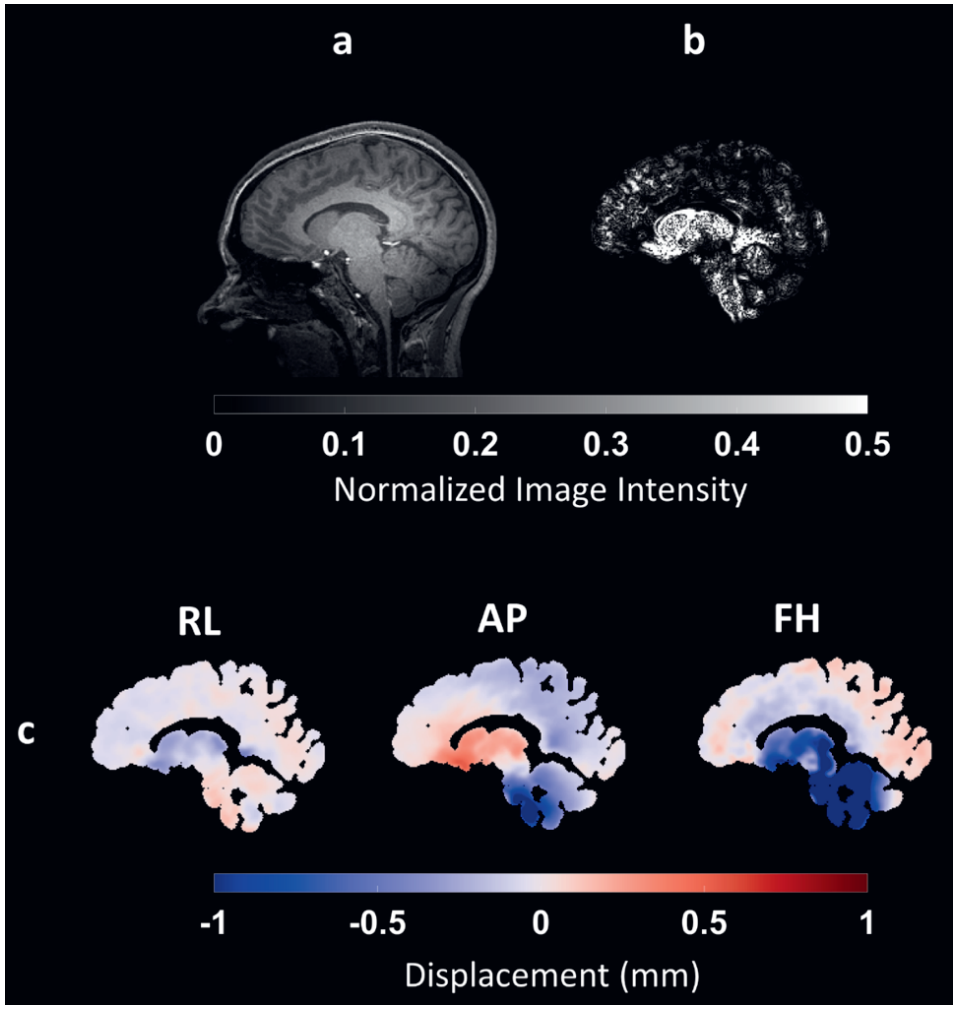

Figure 9. Impact of amplified RL motion on sagittal images. a) Anatomical reference normalized to unity. b) Absolute difference of 3D Damp-MRI and 2D Damp-MRI, normalized to unity. The colormap of b) was scaled by a factor of 10 after normalization to better fit within the color range of a), and thus has an unscaled range of [0 0.05]. c) The RL, AP and FH ground truth displacement maps associated with the slice shown in a). Images in b) and c) are shown at the moment of peak displacement.

4. Discussion

4.1 Summary

We investigated the accuracy of aMRI-derived brain tissue displacements under ideal conditions without image artefacts, using a 2D semi-synthetic dataset with a known amplification factor and known displacements. We found that while the spatial, temporal and average characteristics of brain tissue motion derived from aMRI were very similar to the ground truth, the amplitude was consistently lower than DENSE amplified MRI (Damp-MRI) measurements used for comparison. 2D strain was also computed from the derived displacement fields, where accurate estimation of the amplification factor was found to be more challenging for both Damp-MRI and Dani-aMRI, as reflected by the relatively lower r^2 values achieved for the strain analyses, in comparison to the displacement analyses. Finally, we investigated the accuracy of aMRI-derived displacements under non-ideal conditions, by comparing the aMRI-derived displacements from in-vivo bSSFP acquisitions to DENSE measurements, which showed relatively poor spatial agreement, particularly for the anterior-posterior displacements.

4.2 Agreement

Both Damp-MRI and Dani-aMRI derived displacements showed good agreement to the GTD in the spatial, temporal and ROI-averaged analyses. The performance of Damp-MRI and Dani-aMRI were generally similar, including the inter-subject variation. This shows that deviations from the GTD are mostly related to limitations of the registration algorithm and thus, that the aMRI algorithm performs well under ideal circumstances. These results underscore the importance of the registration algorithm used to extract displacements, and the need for artefact-free images, which could otherwise misguide the registration, as observed in the in-vivo-aMRI experiments. For the strain measurement, r_s^2, r_t^2 and r_a^2 were all lower than those of the AP and FH displacements used in the strain calculation, reflecting the increased uncertainty in the derivation of strain using inaccurate displacements.

4.3 Estimated Amplification

The estimation of the amplification factor (regression slope) from Damp-MRI displacements was found to be significantly more accurate than those from Dani-aMRI. Since the Damp-MRI and Dani-aMRI derived displacements were extracted using the same registration algorithm, the difference in estimated amplification can be attributed to the aMRI algorithm. At the same time, recovery of the expected amplification factor of 10 from the Damp-MRI measurements was not achieved, despite the fairly high r^2 attained in all cases (i.e. $r^2 > 0.88$). This suggests that intrinsic limitations of the registration approach are at least as important as imperfections of the aMRI algorithm for obtaining accurate extraction of brain tissue displacements. To make aMRI truly quantitative, a calibration process that includes the registration imperfections should be established. Establishing such calibration is not

straightforward and might be case-dependent. Nonetheless, even if aMRI is limited to semi-quantitative analyses, there still remains potential for use in cross-sectional or longitudinal clinical research by examining the relative differences in tissue displacements. Independent of the analysis used, the mean estimated amplification factor was generally larger for FH than AP for both Damp-MRI and aMRI measurements. This may be related to the larger displacements typically observed in the FH direction[10], and thus tissue displacement in the FH direction may be more clearly identified by the registration algorithm than that displaced along the AP axis. The estimation of the amplification in the 2D strain analysis was found to be less accurate than that of the amplified displacements used in the strain calculation. Intuitively, this can be understood as resulting from the error in the amplified displacements propagating into the strain calculation. Additionally, the different amplification factors found for the AP and FH displacements would further compound the error in the strain calculation, relative to the ground truth.

4.4 Linear regression analyses

We utilized linear regression analyses to compare the Damp-MRI and aMRI derived displacements to the GTD, separately exploring their spatial, temporal and average characteristics. Alterations in these characteristics may provide biomarkers for brain tissue disorders in clinical settings[3,12]. Therefore, separate investigation of each characteristic yields a more complete picture of the clinical value of the aMRI-derived displacements, as determined in this study. In particular, poor r_s^2 values would indicate that accurate interpretation of the brain tissue strain map on a voxel-wise basis could be challenging since the strain calculation relies on a spatial operation. It should be noted that the percentage errors shown in Figure 5 are a combination of the errors quantified in the spatial amplification and agreement analyses (EA_s and r_s^2). As an example, regions where the percentage error is 50% could arise simply when the EA_s is half of the correct amplification value, even if $r_s^2 = 1$.
Similarly, poor r_t^2 values would suggest that temporal changes (such as the cardiac-induced swelling of microvasculature) may not be accurately represented in the registration-derived displacements. Therefore, given that aMRI scored highest in the r_a^2 analysis, methods involving ROI tissue displacement averaging, such as those utilized by Saindane et al.[3], may provide useful displacement estimates for aMRI.

4.5 In-vivo-aMRI

The in-vivo-aMRI images suffered from the presence of bSSFP banding artefacts, which are known to be worse at higher field strengths[21]. The displacements extracted from the in-vivo-aMRI images compared poorly to the DENSE measurements, highlighting potential pitfalls of this approach for quantifying brain tissue motion. The mismatch between the DENSE and in-vivo-aMRI derived displacements is nonetheless considered to be the summed effect of registration and aMRI errors, image artefacts and also through-plane motion. Extraction of

accurate displacements from in-vivo-aMRI with these (amplified) artefacts is a challenging registration problem. However, the registration was only performed using samples derived from within the brain tissue mask to mitigate the effect of the banding artefacts, which were most noticeable in CSF regions. Additionally, both aMRI and the registration algorithm showed excellent performance in the semi-synthetic analysis, even when alternative contrasts and through-plane motion were investigated. The results of the 2D Damp-MRI/Dani-MRI analyses on images with T1w contrast (which were similar to the results obtained from the semi-synthetic bSSFP analyses) also supports the hypothesis that these two image contrasts are suitable for use with both aMRI and the registration algorithm. Finally, minor differences were observed between the 2D and 3D Damp-MRI/Dani-aMRI analyses, suggesting that the impact of through-plane amplified brain tissue motion for mid-sagittal images is limited (see Table 2). Taken altogether, these insights suggest that the image artefacts are the main confounding contributor to the poor performance seen in the in-vivo-aMRI analyses. Similarly to the semi-synthetic approach, poor estimation of the displacements are propagated to the 2D strain calculation, resulting in the low r_s^2, r_t^2 and r_a^2 values observed in this analysis.

4.6 Clinical Research Value of Brain Tissue Displacement and Strain

The value of brain tissue displacements for clinical research has been demonstrated using integrated PC-MRI velocity measurements[4], motion tracking software[22], ultrasound[23], aMRI[12], tagged MRI[24] and DENSE[3]. For the quantification of cardiac-induced brain tissue displacement, it has been argued that DENSE may be an ideal method due to the sensitivity achieved, which is necessary to measure the minuscule amount of tissue motion[5]. Magnetic Resonance Elastography (MRE) is another promising technique to probe brain tissue displacements and (visco)elastic properties[25–27]. These methods typically have a setup complexity rivalling DENSE; whereas DENSE currently requires implementation of a pulse sequence on the MR scanner, MRE can be used in conjunction with the clinically available phase contrast imaging (provided that velocity encoding below 1 cm/s is permitted in the user interface), but nonetheless requires special hardware. However, phase contrast imaging is not ideal for measuring brain tissue motion. This is because peak cardiac induced brain tissue displacements are ~300 micrometres[5,10], and the time to peak cardiac output is ~300 milliseconds[28], leading to the need for an encoding velocity of ~1 mm/s. This encoding velocity requires impractically large bipolar gradients, and ultimately leads to the use of a suboptimal encoding velocity, resulting in a large loss in the signal to noise ratio. Additionally, the short gradient ramp times, and large bipolar gradients required to encode the low tissue velocities may lead to eddy currents which yield additional erroneous phase terms to the tissue velocity estimation[29]. Moreover, the stepwise integration of the velocity as a way to yield displacement measures may result in additional errors.

In addition to quantitative measurements of tissue displacement directly available through DENSE, we illustrated that similar to aMRI, DENSE can also provide a qualitative assessment of sub-voxel tissue motion through Damp-MRI, which allows an intuitive visualization of brain tissue physiology. Nevertheless, in this study we sought to establish the potential of aMRI for quantifying brain tissue displacements since it has a relatively high feasibility for widespread clinical availability in comparison to DENSE. The Dani-aMRI derived displacements compared favorably to the Damp-MRI derived displacements, and also to the ground truth. However, the derivation of strain (which may prove to be an important marker for brain diseases[7]) noticeably suffers. We therefore recommend that care be taken regarding the quantification of strain from the amplified displacements using methods as described in this study, as it critically requires knowledge of the amplification factor to correct the resulting amplified strain. Moreover, the results of the in-vivo-aMRI analysis suggests that extreme care must be taken with the MR acquisition protocol used for aMRI analysis of brain tissue motion when applied to real MR images.

4.7 Limitations

We explored the performance of aMRI in-vivo using bSSFP cine-images acquired at 7T, where banding artefacts are more severe. Under these non-ideal conditions, the reproducibility of aMRI-derived displacements may also be limited, however this was outside the scope of this study. Additionally, it is conceivable that different slice orientations, positions and thicknesses than that utilized in this study may result in an increased sensitivity to through-plane motion. Therefore, while this work describes the potential and pitfalls of aMRI, future studies should investigate the performance of aMRI algorithms for each particular application, given the illustrated sensitivity to both the image acquisition parameters, as well as the registration methods.

5. Conclusion

aMRI-derived displacements are comparable to DENSE under ideal conditions, strengthening the potential of aMRI as a means for investigating brain tissue displacements in the healthy and diseased brain. However, calibration must be established in order to accurately extract displacement (and therefore strain field) maps, otherwise aMRI will be limited to semi-quantitative analyses. The true bottle neck for clinical applications appears to be the artifacts and noise in the in-vivo images, which warrants careful attention on image quality when performing aMRI. Future work is necessary to investigate the extent to which these limitations hinder practical use of aMRI for studying tissue motion in the healthy and diseased brain.

References

1. Levy LM, Di Chiro G, McCullough DC, Dwyer AJ, Johnson DL, Yang SSL. Fixed spinal cord: Diagnosis with MR imaging. *Radiology*. 1988;169(3):773-778. doi:10.1148/radiology.169.3.3186999
2. Hofmann E, Warmuth-Metz M, Bendszus M, Solymosi L. Phase-contrast MR imaging of the cervical CSF and spinal cord: Volumetric motion analysis in patients with Chiari I malformation. *Am J Neuroradiol*. 2000;21(1):151-158.
3. Saindane AM, Qiu D, Oshinski JN, et al. Noninvasive Assessment of Intracranial Pressure Status in Idiopathic Intracranial Hypertension Using Displacement Encoding with Stimulated Echoes (DENSE) MRI: A Prospective Patient Study with Contemporaneous CSF Pressure Correlation. *Am J Neuroradiol*. 2018;39(2):311-316. doi:10.3174/ajnr.A5486
4. Lawrence BJ, Luciano M, Tew J, et al. Cardiac-Related Spinal Cord Tissue Motion at the Foramen Magnum is Increased in Patients with Type I Chiari Malformation and Decreases Postdecompression Surgery. *World Neurosurg*. 2018;116(5):e298-e307. doi:10.1016/j.wneu.2018.04.191
5. Adams AL, Kuijf HJ, Viergever MA, Luijten PR, Zwanenburg JJM. Quantifying cardiac-induced brain tissue expansion using DENSE. *NMR Biomed*. 2019;32(2):e4050. doi:10.1002/nbm.4050
6. Adams AL, Viergever MA, Luijten PR, Zwanenburg JJM. Validating faster DENSE measurements of cardiac-induced brain tissue expansion as a potential tool for investigating cerebral microvascular pulsations. *Neuroimage*. 2020;208(December 2019):116466. doi:10.1016/j.neuroimage.2019.116466
7. Champagne AA, Peponoulas E, Terem I, et al. Novel strain analysis informs about injury susceptibility of the corpus callosum to repeated impacts. *Brain Commun*. 2019;1(1):1-14. doi:10.1093/braincomms/fcz021
8. Sweetman B, Linninger AA. Cerebrospinal fluid flow dynamics in the central nervous system. *Ann Biomed Eng*. 2011;39(1):484-496. doi:10.1007/s10439-010-0141-0
9. Aletras AH, Ding S, Balaban RS, Wen H. DENSE: Displacement Encoding with Stimulated Echoes in Cardiac Functional MRI. *J Magn Reson*. 1999;137(1):247-252. doi:10.1006/jmre.1998.1676
10. Soellinger M, Rutz AK, Kozerke S, Boesiger P. 3D cine displacement-encoded MRI of pulsatile brain motion. *Magn Reson Med*. 2009;61(1):153-162. doi:10.1002/mrm.21802
11. Holdsworth SJ, Rahimi MS, Ni WW, Zaharchuk G, Moseley ME. Amplified magnetic resonance imaging (aMRI). *Magn Reson Med*. 2016;75(6):2245-2254. doi:10.1002/mrm.26142
12. Terem I, Ni WW, Goubran M, et al. Revealing sub-voxel motions of brain tissue using phase-based amplified MRI (aMRI). *Magn Reson Med*. 2018;80(6):2549-2559. doi:10.1002/mrm.27236
13. Klein S, Staring M, Murphy K, Viergever MA, Pluim J. elastix: A Toolbox for Intensity-Based Medical Image Registration. *IEEE Trans Med Imaging*. 2010;29(1):196-205. doi:10.1109/TMI.2009.2035616
14. Chan DD, Toribio D, Neu CP. Displacement smoothing for the precise MRI-based measurement of strain in soft biological tissues. *Comput Methods Biomech Biomed Engin*. 2013;16(8):852-860. doi:10.1080/10255842.2011.641178
15. Wadhwa N, Rubinstein M, Durand F, Freeman WT. Phase-based video motion processing. *ACM Trans Graph*. 2013;32(4):1-10. doi:10.1145/2461912.2461966
16. Sotiras A, Davatzikos C, Paragios N. Deformable Medical Image Registration: A Survey. *IEEE Trans Med Imaging*. 2013;32(7):1153-1190. doi:10.1109/TMI.2013.2265603
17. Metz CT, Klein S, Schaap M, van Walsum T, Niessen WJ. Nonrigid registration of dynamic medical imaging data using nD+t B-splines and a groupwise optimization approach. *Med Image Anal*. 2011;15(2):238-249. doi:10.1016/j.media.2010.10.003
18. Ledesma-Carbayo MJ, Kybic J, Desco M, et al. Spatio-temporal nonrigid registration for ultrasound cardiac motion estimation. *IEEE Trans Med Imaging*. 2005;24(9):1113-1126. doi:10.1109/TMI.2005.852050
19. Seghers D, D'Agostino E, Maes F, Vandermeulen D, Suetens P. Construction of a brain template from MR images using state-of-the-art registration and segmentation techniques. *Lect Notes Comput Sci*.

2004;3216(PART 1):696-703. doi:10.1007/978-3-540-30135-6_85

20. Geng X, Christensen GE, Gu H, Ross TJ, Yang Y. Implicit reference-based group-wise image registration and its application to structural and functional MRI. *Neuroimage*. 2009;47(4):1341-1351. doi:10.1016/j.neuroimage.2009.04.024
21. Miraux S, Massot P, Ribot EJ, Franconi JM, Thiaudiere E. 3D TrueFISP imaging of mouse brain at 4.7T and 9.4T. *J Magn Reson Imaging*. 2008;28(2):497-503. doi:10.1002/jmri.21449
22. Dawes BH, Lloyd RA, Rogers JM, Magnussen JS, Bilston LE, Stoodley MA. Cerebellar Tissue Strain in Chiari Malformation with Headache. *World Neurosurg*. 2019;130:e74-e81. doi:10.1016/j.wneu.2019.05.211
23. Ternifi R, Cazals X, Desmidt T, et al. Ultrasound measurements of brain tissue pulsatility correlate with the volume of MRI white-matter hyperintensity. *J Cereb Blood Flow Metab Off J Int Soc Cereb Blood Flow Metab*. 2014;34(6):942-944. doi:10.1038/jcbfm.2014.58
24. Soellinger M, Ryf S, Boesiger P, Kozerke S. Assessment of human brain motion using CSPAMM. *J Magn Reson Imaging*. 2007;25(4):709-714. doi:10.1002/jmri.20882
25. Hiscox L V, Johnson CL, Barnhill E, et al. Magnetic resonance elastography (MRE) of the human brain: technique, findings and clinical applications. *Phys Med Biol*. 2016;61(24):R401-R437. doi:10.1088/0031-9155/61/24/R401
26. Johnson CL, Holtrop JL, McGarry MDJ, et al. 3D multislab, multishot acquisition for fast, whole-brain MR elastography with high signal-to-noise efficiency. *Magn Reson Med*. 2014;71(2):477-485. doi:10.1002/mrm.25065
27. Schrank F, Warmuth C, Tzschätzsch H, et al. Cardiac-gated steady-state multifrequency magnetic resonance elastography of the brain: Effect of cerebral arterial pulsation on brain viscoelasticity. *J Cereb Blood Flow Metab*. 2020;40(5):991-1001. doi:10.1177/0271678X19850936
28. Harrild DM, Han Y, Geva T, Zhou J, Marcus E, Powell AJ. Comparison of cardiac MRI tissue tracking and myocardial tagging for assessment of regional ventricular strain. *Int J Cardiovasc Imaging*. 2012;28(8):2009-2018. doi:10.1007/s10554-012-0035-3
29. Krishnamurthy LC, Mao D, King KS, Lu H. Correction and optimization of a T2-based approach to map blood oxygenation in small cerebral veins. *Magn Reson Med*. 2016;75(3):1100-1109. doi:10.1002/mrm.25686

Chapter 6

Summary and General Discussion

Summary

The overarching ambition guiding this project was the development of an MRI-based technique through which the damage to the brain tissue microvasculature as a consequence of cerebral small vessel disease (cSVD) may be investigated. Cardiac-induced brain tissue volumetric strain, a metric derived from displacement measurements of the brain tissue is the end product of that effort. Due to the inherent challenges involved in directly imaging the microvasculature in-vivo, the displacement encoding with stimulated echoes (DENSE) method utilised in this body of work instead relies on assessing the local impact of microvasculature pulsations on the surrounding tissue bed. As such, brain tissue volumetric strain provides an indirect window through which the status/condition of the cerebral microvasculature can be assessed. It quantifies local changes in the cerebral tissue blood volume that arises from cardiac activity, and therefore represents a metric of microvasculature physiology.

A successful implementation of the DENSE MRI technique at both 3T and 7T field strengths is described in **Chapter 2.** The method can assess brain tissue pulsations with full spatial and temporal coverage of the brain and cardiac cycle. Measurements taken at both field strengths were found to be similar, however the higher signal-to-noise ratio (SNR) at 7T proved to be more useful due to the propagation of noise and uncertainty when calculating the spatial derivatives necessary to quantify the tissue volumetric strain. Additionally, differences were detected between grey and white matter tissue volumetric strain, suggesting that volumetric strain can be used to detect regional differences in brain tissue pulsations. The estimation of brain tissue volume change was comparable to the literature values of cerebrospinal fluid (CSF) volume displaced to the spinal canal. Together, these three points strengthen the argument for the use of DENSE MRI in the exploration of brain tissue pulsations. However, it was noted that the SNR limitations of DENSE-derived measurements needed improvement to improve the volumetric strain results.

A reduction in acquisition time was also desirable. To address the SNR and acquisition shortcomings identified in chapter 2, a retrospectively-gated implementation of DENSE was developed for measuring brain tissue pulsations at 7T. This approach involved retrospectively sorting through acquired data to select specific cardiac phases for analysis, yielding faster acquisition times and an improved SNR without loss of spatial coverage. In **Chapter 3,** the brain tissue volumetric strain obtained from the retrospectively-gated DENSE approach was shown to be a reproducible measurement in healthy subjects. Furthermore, changes in the brain tissue volume were found to be correlated with CSF expelled from the intracranial cavity, providing an internal validation of the technique. Additionally, a temporal delay between peak volume change in grey and white matter was observed, which is likely reflective of the vascularization differences between the two tissue types. These results confirmed the technical feasibility, and highlighted the potential of retrospectively-gated

DENSE as a tool for characterizing regional differences in the physiology of the brain tissue microvasculature, and possibly also pathological changes. Overall, the use of retrospectively-gated DENSE MRI at 7T was found to permit fast and accurate measurements of brain tissue volumetric strain.

Chapters 2 and **3** laid the important groundwork to demonstrate the utility of volumetric strain measurements for investigating the microvasculature. However, as those studies only used healthy subjects, the capacity of volumetric strain to discern differences in patients with vascular disease was explored in **Chapter 4** as a proof of concept. The study specifically focused on white matter lesions, and regions at risk to the development of white matter lesions. The results of the study indicated that volumetric strain could illuminate differences in the pulsatile characteristics of cardiac-induced brain tissue motion between patients with vascular disease and healthy controls. Additionally, the observed altered strain patterns in the patient group was suggestive of a stiffer vasculature in that cohort. The findings of the study are thought to be in line with the current consensus that the increased pulsatile energy delivered from stiffer vessels can cause damage to the cerebral microvasculature. Thus, this chapter provided the proof of principle that volumetric strain can identify differences in brain tissue pulsations between patients with vascular disease and healthy controls. This is an important first step[1] towards developing volumetric strain as a valuable tool for studying neurovascular disorders such as cerebral small vessel disease (cSVD).

Amplified MRI (aMRI) technique is a non-invasive method that utilizes image processing algorithms to enhance the visualization of small tissue displacements in MR images. It has been proposed as a tool to assess brain tissue motion, which is crucial for understanding brain physiology. As a software tool, the barrier for clinical use is relatively small, thus aMRI seemed well placed to permit evaluation of the microvasculature in a clinical setting. The study described in **Chapter 5** investigated its readiness for this purpose. The aMRI algorithm was evaluated using semi-synthetic data derived from DENSE displacements. It was found that quantitative interpretation of aMRI data is reliant on image registration, which introduces errors, particularly in the presence of artifacts. Accurate strain quantification is also not possible in larger regions with limited contrast, such as the white matter on conventional anatomical images. Thus, while aMRI has potential as a qualitative tool, its quantitative capabilities should be utilized with caution.

General Discussion

Investigating the cerebral microvasculature with MRI

The current consensus is that cSVD is a multifaceted, neurological condition that involves an array of structural and functional alterations in the cerebral vessels and tissue, including blood flow, vessel morphology and vessel integrity. It is characterized by widespread small vessel damage throughout the brain, which can lead to a variety of clinical symptoms

including cognitive impairment, stroke, gait disturbance and mood disorders. Many pertinent questions concerning the disease remain unanswered, for example the relationship between the microvasculature damage and other neuroimaging markers of the disease, such as white matter hyperintensities, enlarged perivascular spaces and lacunes. The underlying reason for the comorbidity of cSVD to other neurological disorders, such as stroke and dementia also remain to be explained.

Therefore, given the complexity of cSVD, a reasonable approach to fully explore its underlying pathophysiological mechanisms is to employ a diverse assortment of measurement tools through which different aspects of the disease can be assessed. MRI can be viewed as a powerful technology platform that affords multiple measurement strategies, permitting observations of different aspects of the cerebral microvasculature[2,3]. Consequently, an MR-based tool that could provide new or improved insights into changes to microvascular physiology is valuable, particularly if the tool produces high quality data.
To be precise, I define data quality here as the relevance, informativeness, or usefulness of the data obtained from the MR tool for answering clinical research questions. In this case, the desired clinical outcome is some marker representing the physiological health of the brain tissue microvasculature for the investigation of cSVD. Besides providing relevant information regarding the brain tissue microvasculature (including normal changes or abnormalities), the data provided by the MR tool should preferably be quantitative, allowing for direct comparison and analysis. Even further, due to the spatial heterogeneity of cSVD, whole brain coverage is required.

Additionally, several crucial steps along the development path of a biomarker for cSVD[1] have been achieved with DENSE/volumetric strain measurements. Proof of concept of the technique is established in **Chapter 3** through observations of volumetric strain differences in grey and white matter, and also internal consistency of the measurements with CSF stroke volume. Technical validation is also demonstrated in that chapter through the repeatability measurements. Furthermore, proof of principle is achieved in **Chapter 4** through discrimination of disease relative to controls. Thus, with regards to the quality of data provided and its potential to provide a biomarker of cSVD, the DENSE/volumetric strain measurements achieved in this work can be viewed as a valuable tool for exploring the microvasculature. What remains to be discussed is the novelty of the information provided by the method.

At present day, we are fortunate to find in our current arsenal several other MR-based approaches which achieve the aforementioned data quality guidelines and are also capable of investigating microvascular physiology. Some methods such as Arterial Spin Labelling (ASL) and Diffusion Tensor Imaging (DTI) are commercial products, while others are still in the research stage. Nonetheless, they have all demonstrated proof of principle that they can detect changes caused by disease. Blood flow and perfusion, which reflects the amount

and rate of blood delivered to the brain tissue can be measured by techniques such as Dynamic Contrast Enhanced and Dynamic Susceptibility Contrast Enhanced (DSC) MRI methods[4]. However, as the latter names imply, these techniques use exogenous contrast agents to infer microvasculature properties. Similar endogenous information can be extracted using ASL, in which endogenous contrast is generated by labelling the blood via an inversion RF pulse[5]. Also, Intravoxel Incoherent Motion (IVIM), which is a technique that uses diffusion-weighted imaging to separate perfusion and diffusion effects in the brain tissue, can in principle assess blood volume fraction in addition to blood flow[6]. While IVIM has limited performance when compared to more established techniques like DSC[7], it remains the subject of active research for investigating neurological and cerebrovascular disorders[8]. Phase-Contrast MRI (PCMRI) is also capable of measuring the blood flow velocity of the small vessels, although it is currently limited to 2D slices if one targets the small perforating arteries (in the order of 100 μm diameter) within the brain tissue[9]. The highest resolution 4D PCMRI methods today, can target relatively small arteries (around 1 mm diameter), which are the distal, cortical branches of the cerebral arterial tree[10]. Cerebral blood volume measurements can be obtained using DSC, IVIM methods, and also the Vascular Space Occupancy, which additionally provides neuronal activation and vascular reactivity information[11]. Measurements of microvascular blood oxygenation levels using techniques such as Steady-State Susceptibility Contrast (SSC) and Quantitative Blood-Oxygenation-Level-Dependent (qBOLD) have been used to identify the amount of oxygen carried by haemoglobin in the blood. SSC and qBOLD are further useful for the extraction of parameters specifically related to the venous fraction of the microvasculature[12,13]. Differentiation of the arteriole and venule fractions of the microvasculature is also feasible using susceptibility imaging approaches[14] and other techniques like Vessel Architectural Imaging[15] where metrics such as average vessel size and density can additionally be obtained. Diffusion Tensor Imaging provides information on the microstructural changes in the integrity of white matter tracts, which has use in exploring the cognitive decline associated with cSVD that is thought to arise from impaired neuronal connections caused by microvascular damage. It is clear that these measures individually provide some overlapping but nonetheless complimentary information about microvasculature performance. The information extracted from these assessments are altogether necessary to provide a holistic view of the microvascular damage associated with cSVD.

The main information novelty presented by the DENSE/volumetric strain measurements obtained in this work are the (endogenous) insights into cardiac-induced changes to the microvascular blood volume. PCMRI is a pre-existing tool which can also be used to quantify the brain tissue displacements (and, thus volumetric strain) reflecting microvascular pulsations[16,17], however as discussed in **Chapter 2** there are inherent limitations of using PCMRI to obtain the low velocity tissue motion fields that are associated with cardiac pulsations. The higher sensitivity to minute tissue motion which is achievable with DENSE allows us to more accurately probe tissue pulsations at smaller amplitudes. Similarly, as

shown in **Chapter 5,** aMRI can provide information on tissue motion and strain, however it faces data quality shortcomings due to being a semi-quantitative method. From this perspective, DENSE is a clear improvement to the PCMRI and aMRI based approaches for investigating brain tissue blood volume pulsations.

The way in which DENSE measures brain tissue motion fields is similar to the methods used in MR Elastography (MRE), however important distinctions exist here as well which indicate that the approach used in this body of work reflects a substantially different tool to explore the cerebral small vessels. Typical MRE analyses use motion fields generated at high frequencies with an external actuator to calculate shear deformations and derive metrics reflecting tissue stiffness. There is growing evidence that these tissue stiffness metrics may have clinical value[18–20], however they primarily reflect brain tissue biomechanical properties at frequencies to which the brain is not typically exposed. As a result, there is an increased interest to use natural cardiac pulsations as a source for the motion fields, a method known in elastography as intrinsic activation[21–23]. At cardiac frequencies, reconstruction of tissue stiffness remains challenging, primarily as MRE captures the tissue motion using similar motion encoding gradients as PCMRI[23,24], and thus face the aforementioned difficulties of accurate quantification. However, this limitation may be alleviated given the recent success of elastography methods that also employ DENSE to measure the motion fields[25], although it remains to be seen whether this approach can be adapted to the lower frequencies needed to measure intrinsic activation. Additional challenges include modifications to the wave propagation models used in MRE for intrinsic activation[21], which must be updated to reflect non-sinusoidal waves (since the arterial pulsations are themselves not purely sinusoidal), and to reflect distributed sources within the parenchyma (as extrinsic MRE is modelled using waves generated from synchronised sources directed centripetally from the surface of the parenchyma). Finally, studies investigating intrinsic activation brain remains primarily focused on analyses of the shear waves[21,26], although in principle volumetric strain can also be derived[23,27]. Given that the displacement fields are the primary input for the non-linear inversion algorithms used in MRE, it is foreseeable that tissue stiffness metrics may be derived directly through DENSE measurements, although the aforementioned challenges related to the assumptions described by the tissue model must be further investigated to maximize the potential for clinical research. Such joint analyses may permit inference of both local brain tissue volume and stiffness changes associated with cardiac pulsations, which could lead to vital insights on small vessel damage along with the subsequent impact this damage has on the tissue itself. The measurements obtained with DENSE in this work reveal the feasibility and utility of volumetric strain to capture cardiac-induced local blood volume changes in brain tissue, and thus strengthens/supports the future development of volumetric strain analyses with MRE at physiological frequencies. With the additional feasibility of deriving tissue stiffness characteristics akin to those achieved with MR Elastography, DENSE/volumetric strain measurements could form the basis for a tool with potential application to clinical research in the field of cSVD and other brain diseases.

Potential applications

In **Chapter 4,** the observation of altered volumetric strain patterns in patients with cSVD in comparison to healthy controls supports the arguments for tissue volumetric strain as a promising avenue for understanding the pathophysiology of cSVD. The altered strain is hypothesized to be related to an increase in stiffness of the walls of the cerebral microvasculature or surrounding tissue bed. Specifically, an increase in arterial wall stiffness reduces its ability to dampen pulsatile energy as the pulse wave propagates deeper into the arterial tree, leading to altered strain patterns. This is also the biophysical mechanism proposed under the pulse wave encephalopathy hypothesis to model the stiffer vasculature and microvasculature damage observed in cSVD cases[28]. The idea is further supported by the Bramwell-Hill equation[29], which captures the interplay between the pulse wave velocity and the vascular compliance in its volume per unit length. Since compliance is a measure of the change in arterial blood volume induced by a change in arterial pressure, the Bramwell-Hill equation can also be expressed in terms of volumetric strain. Because vascular compliance is inversely proportional to its stiffness, brain tissue volumetric strain measurements hold potential to allow researchers to investigate clinical questions related to vascular stiffness in cSVD.

$$PWV = \sqrt{\frac{1}{C}\frac{V}{\rho}} = \sqrt{\frac{\Delta P}{\Delta V}\frac{V}{\rho}} = \sqrt{\frac{1}{\epsilon_v}\frac{\Delta P}{\rho}} \qquad [1]$$

Eqn 1. The Bramwell-Hill equation used to infer arterial compliance through measurements of the pulse wave velocity[29]. PWV = pulse wave velocity, ρ = density of blood, C = vascular compliance, P = blood pressure, V = volume per unit length, ϵ_v= volumetric strain.

An immediate observation from Eqn. 1 is that the pulse wave velocity is inversely proportional to the volumetric strain for a given change in arterial pressure. However, whether the Bramwell-Hill equation can be applied to the cerebral microvasculature remains uncertain, due to some underlying assumptions in the equation such as wall thickness vs radius which may not be appropriate for the microvasculature. The measurements obtained for tissue volumetric strain are derived from tissue deformations, and as such may additionally encode the stiffness of the surrounding tissue and not only the vessel walls themselves. As tissue stiffness may play a role in the observed strains, it may be challenging to disentangle whether changes in tissue strain with age or disease arises from vessel stiffness, tissue stiffness, or both. To address this challenge, joint MR elastography analyses such as that performed by Perriñez et al.[30] may be useful in determining the contributions of tissue and vessel stiffness to the measured cardiac-induced tissue strains.

Brain tissue volumetric strain reflects cardiac-induced blood volume changes in the tissue. This implies that the measurements could also contain important information on venous physiology, which might provide another avenue to understand the pathophysiology of

cSVD. The cerebral veins are flexible conduits that adjust to fluctuations in blood pressure and flow from the cardiac cycle. Venous collagenosis is a pathological process that thickens the collagen fibers in the vein walls, reducing their compliance and elasticity and increasing resistance to blood flow[31,32]. This can impede blood drainage from the brain, leading to ischemia, inflammation, and white matter damage. Although venous collagenosis is recognized as one of the mechanisms linking vascular risk factors to cSVD development and progression[33], its precise role as a primary cause, secondary consequence, or modulating factor in cSVD remains unknown. Volumetric strain measurements could feasibly be used to shed light on the role of venous collagenosis in cSVD. Given that collagenized veins have stiffer walls than healthy veins, they should exhibit less expansion or contraction per cardiac cycle, resulting in an altered volumetric strain. Alternatively, such collagenosis might be a reactive effect of the veins in response to prolonged exposer to excessively large volumetric strains. Achieving successful volumetric strain measurements of the venous fraction of the microvasculature may require different acquisition approaches to specifically target the tissue pulsations that occur due to blood volume changes in the venous fraction. Alternatively, postprocessing approaches that rely on the relative timing of cardiac-induced volume changes in the microvasculature may yet prove fruitful, assuming that the venous fraction exhibits delayed strain activity relative to the arterial fraction. **Chapter 4** presents some initial evidence suggesting that there are pulsatile compressive strain energies within the parenchyma. These could arise in part from the venous compartment of the microvasculature which is thought to collapse as the pressure decreases during venous outflow, similar to the systolic compression of the coronary arteries in the heart muscle. However, additional research is still needed to determine the relationship between venous collagenosis and cSVD, and further the extent to which volumetric strain can be used to investigate the venous fraction of the microvasculature.

The lack of established normal ranges for volumetric strain in both healthy controls and cSVD subjects however represents a significant challenge in interpreting and comparing the results of volumetric strain measurements. Therefore, future studies should prioritize establishing normal ranges of volumetric strain in diverse populations, including healthy individuals and those with cSVD. Establishment of normal volumetric strain ranges in healthy individuals should permit a better understanding of the natural variability of cardiac induced volumetric strain in the absence of disease. This baseline information is crucial for accurately interpreting the altered volumetric strain measurements in individuals with cSVD. Furthermore, studying volumetric strain in healthy individuals could provide valuable information about the impact of lifestyle factors, such as exercise and diet, on cerebrovascular function. Similarly, studying volumetric strain in individuals with cSVD could potentially add value in understanding the impact of cerebrovascular function on disease severity or location. Moreover, comparing volumetric strain measurements between healthy controls and individuals with cSVD may help identify novel markers and potential therapeutic targets for the disease.

Volumetric strain measurements may also be useful for studying other cerebral diseases such as hydrocephalus. Hydrocephalus is a condition characterized by an abnormal accumulation of cerebrospinal fluid within the ventricles of the brain, leading to increased intracranial pressure and potentially resulting in brain damage[34]. The current diagnosis and management of hydrocephalus relies heavily on imaging studies such as MRI, but there remains a need for more sensitive and specific non-invasive tools to detect alterations in the brain tissue and cerebrospinal fluid dynamics. Brain tissue volumetric strain may have the potential to provide valuable insights into the underlying pathophysiology of hydrocephalus[27], particularly if the complex interplay between CSF dynamics, intracranial pressure and a fixed intracranial volume leads to changes in brain tissue pulsations[35]. Volumetric strain measurements may further be useful to quantify changes in the brain tissue mechanics in response to shunt placement or other surgical interventions, which could help clinicians optimize their treatment plans for individual patients. Overall, volumetric strain may serve as an important tool for advancing our understanding of hydrocephalus, potentially leading to improved treatment strategies and outcomes for patients.

Even for non-vascular brain diseases, such as brain tumors, brain tissue volumetric strain may find clinical value. This may be particularly useful for the diagnosis of tumor pseudoprogression, which is a treatment-induced lesion enhancement that mimics tumor progression[36]. It is essential to distinguish between these pseudoprogression and true tumor growth, as further treatment for true tumor progression may be necessary, whereas treatment for pseudoprogression may cause unnecessary side effects and complications. Conventional anatomical MR imaging is not always adequate to differentiate tumor pseudoprogression from true progression. Advanced MRI methods, such as perfusion MRI, MR spectroscopy and diffusion-weighted imaging can provide hemodynamic, metabolic, and diffusion parameters, which can be altered in cases of tumor pseudoprogression relative to viable tumor tissue. Volumetric strain and feasibly also octahedral shear strain analyses[37] could be used to quantify the tumor deformation induced by cardiac motion and could complement existing imaging techniques for tumor pseudoprogression diagnosis.

In summary, brain tissue volumetric strain has potential application to the clinical research of cerebral diseases such as cSVD, gliomas and hydrocephalus. Further research is however needed to fully explore the research value of this tool and to address the associated challenges. Some of these challenges may be addressed in future developments to the technique and related fields, which is subsequently discussed.

Future developments and opportunities

The continuous advancement of science and technology offers inspiration and expectations for future research, on which I want to reflect in this section. At the hardware level, research efforts are focused on enhancing the probes and sensors which lie at the core of MR technology. The Netherlands is currently seen as a pioneer in ultrahigh field MRI research. To keep their edge, plans are currently in place for the construction of a 14 Tesla MR scanner[38]. If successful, the machine would provide a significant boost to the achievable MR

signal that is available for imaging. It would represent a triumph to human engineering and collaboration as the technological challenges of designing a stable, homogenic magnetic field that is ultimately safe for human use are addressed. Considering the transmit and receive RF coils which are used to create and detect the signals of interest, future improvements lie in optimising the shape and size of the coils[39], combining surface loops with dipole antennas[40,41], reductions in coil noise through novel/exotic material properties[42], and designing adaptive coil arrays which improve sensitivity to the anatomical region of interest by enabling a closer fit[43]. These improvements are in addition to the trend of increasing the number of coils to accelerate image acquisition[44,45]. The continued use and improvement of cameras and other sensors which monitor the patient is foreseeable, as through these sensors an assortment of rich physiological information can be obtained which augments the acquired imaging data or be used to perform motion detection and correction[46]. Additionally, MR gradient hardware continues to mature. Recent developments towards fast and silent gradient systems for brain imaging are exciting[47], as these improvements are well-poised to provide SNR and resolution gains without peripheral nerve stimulation penalties, paving the way towards vastly improved subject comfort and compliance.

On the software side, exciting times are upon us at the moment of writing, as it would appear artificial intelligence and associated machine learning principles could form the basis of a technological revolution which could greatly impact medical imaging and research as well. The measurement of brain tissue pulsations covering the entire brain and cardiac cycle requires three orthogonal 4D displacement measurements. These are acquired twice with opposing gradient polarities to remove the background phase and improve SNR through averaging. Altogether, this means that 6-dimensional measurements are necessary for the calculation of brain tissue volumetric strain, which provides a rich reservoir of data that can be exploited using machine learning techniques. AI algorithms applied to the image acquisition and reconstruction processing stages can leverage data attributes to reduce the amount of k-space that must be acquired to yield high quality images[48]. Furthermore, the expected spatial and temporal smoothness of the acquired displacement data could be used to fit the data to a suitable spline model. This would further provide smooth differentiable functions with exact solutions. Alternatively, there are a number of numerical approaches to differentiating noisy data that greatly reduces the propagated uncertainty[49,50]. These could also be employed to improve image quality in the calculated volumetric strain maps. Data denoising before performing numerical differentiation could also yield accurate and high-quality strain maps. However, denoising should be performed carefully to avoid removing features of interest from the data. This could feasibly be achieved using techniques such as Total Variation and other regularization methods, as these methods provide user tuneable parameters that can be used to ensure the reconstructed noise-free image does not differ substantially from the original image[51]. The rapid developments in AI, including denoising methods, makes it conceivable that DENSE measurements with sufficient SNR to obtain

voxel-wise volumetric strain maps can be implemented successfully on MRI scanners with clinical field strengths as well.

Beyond the hardware and software developments, alternative acquisition strategies could provide rich opportunities to be explored using the displacement or strain measurements achieved through DENSE. While characterising microvascular pulsations over the entire cardiac cycle provides a complete picture of the pulsatile nature of the small vessels, ultimately only the moment of peak pulsation may be useful for analysis. An electrocardiogram triggered snapshot acquisition style could feasibly be tuned to capture only the peak impact of the cardiac output. This strategy would allow all available SNR to be spent on acquiring a single frame that is representative of peak microvascular pulsation. Evidence is building that pulsation of the microvasculature also occurs at frequencies below the cardiac frequency[52–55]. These low frequency pulsations arise from respiratory, vasomotion and sleep-related physiological activity. While the subtle brain deformations in the brain induced by respiration can in principle be measured with DENSE[56], it remains to be seen whether DENSE can be used to investigate the lower frequency pulsations from vasomotion and sleep as well. However, alterations to the acquisition strategy may permit these types of pulsatile data to be extracted from strain measurements. Additionally, as these low frequency measurements would require even longer acquisition times, patient comfort, immobilisation and/or motion correction strategies become increasingly important. Finally, as previously mentioned this work proposes that an indirect window to the microvasculature exists, namely through examination of parenchymal pulsations. At the full range of aforementioned pulse frequencies, further tweaks to the acquisition scheme could allow for another indirect window to the microvasculature that does not utilise displacement of parenchymal tissue. Rather, this alternative, indirect window to the microvasculature could be achieved by considering how the pulsating microvasculature drives flow in the perivascular spaces[57,58]. Such assessments would be feasible with DENSE by the addition of a T2-preparation module, allowing DENSE to be sensitized to CSF motion and flow. Consequently, this would allow targeting of the glymphatic system with DENSE, potentially yielding answers pertaining to the role of microvascular pulsations to cerebral waste product clearance.

In general, these developments are expected to yield either an increase in available signal and/or noise reduction. The issue of SNR is a core problem for the exploration of cerebral blood volumes using the volumetric strain data obtained in this work. This is primarily due to the DENSE sequence using a stimulated echo, which results in the loss of half of the signal[59], in conjunction with the propagation of noise from the displacement measurements during the calculation of strain. The promise of increased signal at higher field strengths is thus an attractive one, and may directly lead to improved clinical research with the technique. Furthermore, at higher field strengths the longer T1 relaxation time may prove to be

additionally advantageous since the stimulated echo decays at a slower rate, thereby improving signal availability for acquisition of later cardiac phases[60].

A portion of the boosted SNR could be additionally traded for an increase in image resolution, which would address some important limitations of this work, and allow for further interesting analyses. In this work, relatively large voxel sizes were imposed to increase the SNR per voxel at the cost of localization, and increased partial volume effects. Altogether, these factors contribute to the appearance of noisy strain maps, which may have limited clinical research value beyond averaging over large ROIs. At higher image resolutions, avoiding, or indeed directly examining the PVS might be achievable. This would permit removal or confirmation of suspected PVS contributions to the strain that was mentioned in **Chapter 4,** and could further allow the investigation of the glymphatic system, which would help us better understand the clearance of cerebral waste. Furthermore, at higher image resolutions the postprocessing steps used in this work to reduce the influence of partial volume effects may no longer be necessary. This would be particularly useful in the case of the grey mater (GM), since the postprocessing steps to alleviate the partial-volume effects leads to significant erosion in that region of interest (ROI). As a result of this step, one is left with what can effectively be seen as semi-random sample of the total available GM voxels, which limits analyses of strain in that ROI.

Taken altogether, it is my opinion that the aforementioned developments will lead to the holy grail of brain tissue volumetric strain imaging, videlicet smaller ROI sizes for analysis, and eventually voxel-wise analyses at high resolutions. Considering the noise propagation analysis described in Chapter **2,** an approximate factor of 10 improvement in the SNR of the strain map is necessary for voxel-wise analyses at the image resolutions used in this work. At higher image resolutions the required SNR to achieve voxel-wise analyses also increases. The combined increase in SNR that could be achieved through the aforementioned hardware and software developments, alongside a more pragmatic acquisition strategy such as a triggered snapshot acquisition, certainly leads the way towards more accurate strain analyses and an overall improved MRI tool for clinical cerebral microvascular research.

Conclusion

Science can be viewed as a ‘candle in the dark’[61], the light thereof providing a means to explore and understand the world we find ourselves in. Within the scope of scientific advancements, this body of work then figuratively details the kindling of an additional flame, one that adds to a torch which illuminates the cerebral microvasculature and its disorders.

In this work the DENSE MRI technique was adapted and refined to capture brain tissue motion and reveal the cardiac-induced blood volume changes in the microvascular network. My findings suggest that DENSE is a powerful tool for investigating the microvasculature as it can potentially provide information on the deformation, compliance, and pulsatility of the microvasculature and surrounding tissue bed. Volumetric strain is a pulsatility metric

derived through the DENSE measurements which can be used to detect subtle changes to the microvasculature arising from cerebrovascular disease. The method thus has great potential as a research tool for exploring the normal and abnormal biomechanics of the cerebral microvasculature, and compliments other MR techniques which also explore microvascular physiology.

It is anticipated that future developments in related fields will make it possible to overcome some of the challenges and limitations of DENSE by increasing the available SNR, reducing the acquisition time, and simplifying the post-processing steps. These improvements will make DENSE an even more effective and reliable technique for studying the cerebral microvasculature in health and disease. My hope is that this work will inspire further research on the use of DENSE as a means to better understand the biomechanics of the cerebral microvasculature.

References

1. Smith EE, Biessels GJ, De Guio F, et al. Harmonizing brain magnetic resonance imaging methods for vascular contributions to neurodegeneration. *Alzheimer's and Dementia: Diagnosis, Assessment and Disease Monitoring*. 2019;11:191-204. doi:10.1016/j.dadm.2019.01.002
2. Callewaert B, Jones EA V., Himmelreich U, Gsell W. Non-Invasive Evaluation of Cerebral Microvasculature Using Pre-Clinical MRI: Principles, Advantages and Limitations. *Diagnostics*. 2021;11(6):926. doi:10.3390/diagnostics11060926
3. Zwanenburg JJM, van Osch MJP. Targeting Cerebral Small Vessel Disease With MRI. *Stroke*. 2017;48(11):3175-3182. doi:10.1161/STROKEAHA.117.016996
4. Zakariaee SS, Oghabian MA, Firouznia K, Sharifi G, Arbabi F, Samiei F. Assessment of the Agreement between Cerebral Hemodynamic Indices Quantified Using Dynamic Susceptibility Contrast and Dynamic Contrast-enhanced Perfusion Magnetic Resonance Imagings. *J Clin Imaging Sci*. 2018;8(1):2. doi:10.4103/jcis.JCIS_74_17
5. Hernandez-Garcia L, Aramendía-Vidaurreta V, Bolar DS, et al. Recent Technical Developments in ASL: A Review of the State of the Art. *Magn Reson Med*. 2022;88(5):2021-2042. doi:10.1002/mrm.29381
6. Zhu G, Heit JJ, Martin BW, Marcellus DG, Federau C, Wintermark M. Optimized Combination of b-values for IVIM Perfusion Imaging in Acute Ischemic Stroke Patients. *Clin Neuroradiol*. 2020;30(3):535-544. doi:10.1007/s00062-019-00817-w
7. Wirestam R, Borg M, Brockstedt S, Lindgren A, Holtås S, Ståhlberg F. Perfusion-related parameters in intravoxel incoherent motion MR imaging compared with CBV and CBF measured by dynamic susceptibility-contrast MR technique. *Acta Radiol*. 2001;42(2):123-128. http://www.ncbi.nlm.nih.gov/pubmed/11281143
8. Paschoal AM, Leoni RF, dos Santos AC, Paiva FF. Intravoxel incoherent motion MRI in neurological and cerebrovascular diseases. *Neuroimage Clin*. 2018;20:705-714. doi:10.1016/j.nicl.2018.08.030
9. Geurts LJ, Zwanenburg JJM, Klijn CJM, Luijten PR, Biessels GJ. Higher Pulsatility in Cerebral Perforating Arteries in Patients with Small Vessel Disease Related Stroke, a 7T MRI Study. *Stroke*. 2019;50(1):62-68. doi:10.1161/STROKEAHA.118.022516
10. Vikner T, Nyberg L, Holmgren M, Malm J, Eklund A, Wåhlin A. Characterizing pulsatility in distal cerebral arteries using 4D flow MRI. *Journal of Cerebral Blood Flow and Metabolism*. 2020;40(12):2429-2440. doi:10.1177/0271678X19886667
11. Huber L (Renzo), Poser BA, Kaas AL, et al. Validating layer-specific VASO across species. *Neuroimage*. 2021;237. doi:10.1016/j.neuroimage.2021.118195
12. Liu S, Buch S, Chen Y, et al. Susceptibility-weighted imaging: current status and future directions. *NMR Biomed*. 2017;30(4). doi:10.1002/nbm.3552
13. Domsch S, Mie MB, Wenz F, Schad LR. Non-invasive multiparametric qBOLD approach for robust mapping of the oxygen extraction fraction. *Z Med Phys*. 2014;24(3):231-242. doi:10.1016/j.zemedi.2014.03.009
14. An H, Lin W. Cerebral venous and arterial blood volumes can be estimated separately in humans using magnetic resonance imaging. *Magn Reson Med*. 2002;48(4):583-588. doi:10.1002/mrm.10257
15. Kim M, Park JE, Emblem K, Bjørnerud A, Kim HS. Vessel type determined by vessel architectural imaging improves differentiation between early tumor progression and pseudoprogression in glioblastoma. *American Journal of Neuroradiology*. 2021;42(4):663-670. doi:10.3174/AJNR.A6984
16. Greitz D, Franck A, Nordell B. On the Pulsatile Nature of Intracranial and Spinal CSF-Circulation Demonstrated by MR Imaging. *Acta radiol*. 1993;34(4):321-328. doi:10.1080/02841859309173251
17. Feinberg DA, Mark AS. Human brain motion and cerebrospinal fluid circulation demonstrated with MR velocity imaging. *Radiology*. 1987;163(3):793-799. doi:10.1148/radiology.163.3.3575734
18. Bunevicius A, Schregel K, Sinkus R, Golby A, Patz S. REVIEW: MR elastography of brain tumors. *Neuroimage Clin*. 2020;25:102109. doi:10.1016/j.nicl.2019.102109
19. Murphy MC, Huston J, Ehman RL. MR elastography of the brain and its application in neurological diseases. *Neuroimage*. 2019;187:176-183. doi:10.1016/j.neuroimage.2017.10.008

20. Yin Z, Romano AJ, Manduca A, Ehman RL, Huston J. Stiffness and beyond: What MR elastography can tell us about brain structure and function under physiologic and pathologic conditions. *Topics in Magnetic Resonance Imaging*. 2018;27(5):305-318. doi:10.1097/RMR.0000000000000178
21. Weaver JB, Pattison AJ, McGarry MD, et al. Brain mechanical property measurement using MRE with intrinsic activation. *Phys Med Biol*. 2012;57(22):7275-7287. doi:10.1088/0031-9155/57/22/7275
22. Zorgani A, Souchon R, Dinh AH, et al. Brain palpation from physiological vibrations using MRI. *Proceedings of the National Academy of Sciences*. 2015;112(42):12917-12921. doi:10.1073/pnas.1509895112
23. Hirsch S, Klatt D, Freimann F, Scheel M, Braun J, Sack I. In vivo measurement of volumetric strain in the human brain induced by arterial pulsation and harmonic waves. *Magn Reson Med*. 2013;70(3):671-683. doi:10.1002/mrm.24499
24. Herthum H, Dempsey SCH, Samani A, et al. Superviscous properties of the in vivo brain at large scales. *Acta Biomater*. 2021;121:393-404. doi:10.1016/j.actbio.2020.12.027
25. Strasser J, Haindl MT, Stollberger R, Fazekas F, Ropele S. Magnetic resonance elastography of the human brain using a multiphase DENSE acquisition. *Magn Reson Med*. 2019;(November 2018):1-10. doi:10.1002/mrm.27672
26. McGarry M, Van Houten E, Solamen L, Gordon-Wylie S, Weaver J, Paulsen K. Uniqueness of poroelastic and viscoelastic nonlinear inversion MR elastography at low frequencies. *Phys Med Biol*. 2019;64(7). doi:10.1088/1361-6560/ab0a7d
27. Mousavi SR, Fehlner A, Streitberger KJ, Braun J, Samani A, Sack I. Measurement of in vivo cerebral volumetric strain induced by the Valsalva maneuver. *J Biomech*. 2014;47(7):1652-1657. doi:10.1016/j.jbiomech.2014.02.038
28. Bateman GA. Pulse-wave encephalopathy: A comparative study of the hydrodynamics of leukoaraiosis and normal-pressure hydrocephalus. *Neuroradiology*. 2002;44(9):740-748. doi:10.1007/s00234-002-0812-0
29. C Bramwell MJ, Hill A V, Crighton B ram ell BJ, H ill A V. The velocity of pulse wave in man. *Proceedings of the Royal Society of London Series B, Containing Papers of a Biological Character*. 1922;93(652):298-306. doi:10.1098/rspb.1922.0022
30. Perriñez PR, Kennedy FE, Houten EEWV, Weaver JB, Paulsen KD. Modeling of soft poroelastic tissue in time-harmonic MR elastography. *IEEE Trans Biomed Eng*. 2009;56(3):598-608. doi:10.1109/TBME.2008.2009928
31. Moody DM, Brown WR, Challa VR, Anderson RL. Periventricular venous collagenosis: association with leukoaraiosis. *Radiology*. 1995;194(2):469-476. doi:10.1148/radiology.194.2.7824728
32. Keith J, Gao FQ, Noor R, et al. Collagenosis of the deep medullary veins: An underrecognized pathologic correlate of white matter hyperintensities and periventricular infarction? *J Neuropathol Exp Neurol*. 2017;76(4):299-312. doi:10.1093/jnen/nlx009
33. Lahna D, Schwartz DL, Woltjer R, et al. Venous Collagenosis as Pathogenesis of White Matter Hyperintensity. *Ann Neurol*. Published online December 1, 2022. doi:10.1002/ana.26487
34. Greitz D. Radiological Assessment of Hydrocephalus: New Theories and Implications for Therapy. *Neuroradiol J*. 2006;19(4):475-495. doi:10.1177/197140090601900407
35. Penn RD, Linninger A. The physics of hydrocephalus. *Pediatr Neurosurg*. 2009;45(3):161-174. doi:10.1159/000218198
36. Thust SC, van den Bent MJ, Smits M. Pseudoprogression of brain tumors. *Journal of Magnetic Resonance Imaging*. 2018;48(3):571-589. doi:10.1002/jmri.26171
37. Yin Z, Hughes JD, Glaser KJ, et al. Slip interface imaging based on MR-elastography preoperatively predicts meningioma–brain adhesion. *Journal of Magnetic Resonance Imaging*. 2017;46(4):1007-1016. doi:10.1002/jmri.25623
38. Norris D. Strongest MRI scanner in the world will be built in the Netherlands. Donders Institute for Brain, Cognition and Behaviour. Published 2023. Accessed February 20, 2023. https://www.ru.nl/en/research/research-news/strongest-mri-scanner-in-the-world-will-be-built-in-the-netherlands
39. Mathieu W, Popovic M, Farivar R. Towards Brain MRI Adaptable to Head Size: Bowing RF Coil Phased Arrays. *IEEE J Electromagn RF Microw Med Biol*. 2022;6(3):305-310. doi:10.1109/JERM.2021.3136090

40. Avdievich NI, Solomakha G, Ruhm L, Scheffler K, Henning A. Evaluation of short folded dipole antennas as receive elements of ultra-high-field human head array. *Magn Reson Med*. 2019;82(2):811-824. doi:10.1002/mrm.27754
41. Avdievich NI, Nikulin A V., Ruhm L, et al. A 32-element loop/dipole hybrid array for human head imaging at 7 T. *Magn Reson Med*. 2022;88(4):1912-1926. doi:10.1002/mrm.29347
42. Chen H, Guo L, Li M, et al. Metamaterial-Inspired Radiofrequency (RF) Shield with Reduced Specific Absorption Rate (SAR) and Improved Transmit Efficiency for UHF MRI. *IEEE Trans Biomed Eng*. 2021;68(4):1178-1189. doi:10.1109/TBME.2020.3022884
43. Cogswell PM, Trzasko JD, Gray EM, et al. Application of adaptive image receive coil technology for whole-brain imaging. *American Journal of Roentgenology*. 2021;216(2):552-559. doi:10.2214/AJR.20.22812
44. Wald LL. Parallel Imaging Update: How Many Elements Do We Need? In: *Proceedings of the International Society for Magnetic Resonance in Medicine*. ; 2006:202.
45. Hamilton J, Franson D, Seiberlich N. Recent advances in parallel imaging for MRI. *Prog Nucl Magn Reson Spectrosc*. 2017;101:71-95. doi:10.1016/j.pnmrs.2017.04.002
46. Kyme AZ, Aksoy M, Henry DL, Bammer R, Maclaren J. Marker-free optical stereo motion tracking for in-bore MRI and PET-MRI application. *Med Phys*. 2020;47(8):3321-3331. doi:10.1002/mp.14199
47. Versteeg E, Klomp DWJ, Siero JCW. Accelerating Brain Imaging Using a Silent Spatial Encoding Axis. *Magn Reson Med*. 2022;88(4):1785-1793. doi:10.1002/mrm.29350
48. Lin DJ, Johnson PM, Knoll F, Lui YW. Artificial Intelligence for MR Image Reconstruction: An Overview for Clinicians. *Journal of Magnetic Resonance Imaging*. 2021;53(4):1015-1028. doi:10.1002/jmri.27078
49. Chartrand R. Numerical Differentiation of Noisy, Nonsmooth Data. *ISRN Applied Mathematics*. 2011;2011:1-11. doi:10.5402/2011/164564
50. Farid H, Simoncelli EP. Differentiation of Discrete Multidimensional Signals. *IEEE Transactions on Image Processing*. 2004;13(4):496-508. doi:10.1109/TIP.2004.823819
51. Lu W, Duan J, Qiu Z, Pan Z, Liu RW, Bai L. Implementation of high-order variational models made easy for image processing. *Math Methods Appl Sci*. 2016;39(14):4208-4233. doi:10.1002/mma.3858
52. van Veluw SJ, Hou SS, Calvo-Rodriguez M, et al. Vasomotion as a Driving Force for Paravascular Clearance in the Awake Mouse Brain. *Neuron*. 2020;105(3):549-561.e5. doi:10.1016/j.neuron.2019.10.033
53. Järvelä M, Kananen J, Korhonen V, Huotari N, Ansakorpi H, Kiviniemi V. Increased very low frequency pulsations and decreased cardiorespiratory pulsations suggest altered brain clearance in narcolepsy. *Communications Medicine*. 2022;2(1). doi:10.1038/s43856-022-00187-4
54. Kiviniemi V, Wang X, Korhonen V, et al. Ultra-fast magnetic resonance encephalography of physiological brain activity-Glymphatic pulsation mechanisms? *Journal of Cerebral Blood Flow and Metabolism*. 2016;36(6):1033-1045. doi:10.1177/0271678X15622047
55. Fultz NE, Bonmassar G, Setsompop K, et al. Coupled electrophysiological, hemodynamic, and cerebrospinal fluid oscillations in human sleep. *Science (1979)*. 2019;366(6465):628-631. doi:10.1126/science.aax5440
56. Sloots JJ, Biessels GJ, Zwanenburg JJM. Cardiac and respiration-induced brain deformations in humans quantified with high-field MRI. *Neuroimage*. 2020;210:116581. doi:10.1016/j.neuroimage.2020.116581
57. Daversin-Catty C, Vinje V, Mardal KA, Rognes ME. The mechanisms behind perivascular fluid flow. *PLoS One*. 2020;15(12 December). doi:10.1371/journal.pone.0244442
58. Hirschler L, Runderkamp BA, Franklin SL, et al. The driving force of glymphatics: influence of the cardiac cycle on CSF-mobility in perivascular spaces in humans. In: *Proceedings of the International Society for Magnetic Resonance in Medicine*. ; 2020:643.
59. Kim D, Epstein FH, Gilson WD, Axel L. Increasing the signal-to-noise ratio in DENSE MRI by combining displacement-encoded echoes. *Magn Reson Med*. 2004;52(1):188-192. doi:10.1002/mrm.20109
60. Sigfridsson A, Haraldsson H, Ebbers T, Knutsson H, Sakuma H. In vivo SNR in DENSE MRI; temporal and regional effects of field strength, receiver coil sensitivity and flip angle strategies. *Magn Reson Imaging*. 2011;29(2):202-208. doi:10.1016/j.mri.2010.08.016
61. Sagan C. *The Demon-Haunted World: Science As a Candle in the Dark*. Ballantine Books; 1997.

Appendices

Nederlandse Samenvatting (Dutch Summary)
Acknowledgements (Dankwoord)
Biography
List of publications and presentations

Nederlandse Samenvatting (Dutch Summary)

De microvasculatuur van de hersenen is een complex netwerk van kleine bloedvaten. Deze vaten pulseren als gevolg van een tijdelijke toename van het intracraniale bloedvolume tijdens de hartcyclus, waardoor lokale weefselverplaatsing ontstaat. Cerebrale kleine vaatziekte (cSVD) is een aandoening die deze kleine bloedvaten aantast, wat leidt tot schade in de diepe witte stof van de hersenen. Loopstoornis, cognitieve achteruitgang, dementie en stemmingsstoornissen behoren tot de symptomen van cSVD, die variëren in overeenstemming met de ernst van de ziekte.

Displacement Encoding with Stimulated Echoes (DENSE) is een krachtige MRI-methode die oorspronkelijk is ontworpen voor het meten van de beweging van het hart. Het doel van het werk in dit proefschrift is de ontwikkeling, implementatie en evaluatie van DENSE als een MRI-methode waarmee de conditie van de microvasculatuur in het hersenweefsel onderzocht kan worden. DENSE kan submillimeter verplaatsingen kwantificeren die verband houden met beweging van hersenweefsel, waardoor nauwkeurige metingen van beweging en vervorming (waaronder de relatieve volume verandering, ook aangeduid als volumetrische rek) van hersenweefsel worden verkregen. Deze techniek heeft verschillende voordelen ten opzichte van andere methoden voor het bestuderen van de beweging van hersenweefsel, waaronder het vermogen om door het hart veroorzaakte verplaatsingen te schatten die ordes van grootte kleiner zijn dan de voxelgrootte van de onderliggende afbeeldingen, en deze voor het hele brein in kaart te brengen.

Door hersenweefselpulsaties te meten met behulp van DENSE, kunnen veranderingen in het microvasculaire bloedvolume tijdens de hartcyclus indirect worden onderzocht. Volumetrische rek kan worden berekend uit de beweging van het hersenweefsel, die de zwelling van de microvasculatuur die in het weefsel is ingebed weerspiegelt. In dit werk werd vastgesteld dat DENSE de door het hart geïnduceerde beweging en vervorming van hersenweefsel nauwkeurig kan meten. Er werd ook aangetoond dat DENSE kan worden gebruikt om weefselspecifieke verschillen in volumetrische rek aan het licht te brengen. Verder werd in een exploratieve studie in patiënten andere gedrag van de volumetrische rek gezien in laesies in de witte stof. Dit suggereert dat volumetrische rek metingen nuttig kunnen zijn voor het onderzoeken van cerebrovasculaire aandoeningen.

Dit werk toont aan dat DENSE een krachtig hulpmiddel is voor het meten van door het hart geïnduceerde volumetrische rek in het menselijk brein, en levert daarmee een belangrijke bijdrage aan het vakgebied. Het legt de basis voor een onderzoekstool die in staat is om de biomechanica van de microvasculaire functie te onderzoeken en mogelijk ook de visco-elastische eigenschappen van het hersenweefsel, wat samen kan leiden tot waardevolle inzichten in hersenaandoeningen zoals cSVD. Door de mechanismen van

hersenweefselpulsaties te begrijpen, kunnen we mogelijk nieuwe methoden ontwikkelen voor vroege detectie en behandeling van deze aandoening.

Na een algemene inleiding op het onderwerp in hoofdstuk 1, is dit proefschrift als volgt ingedeeld:

In Hoofdstuk 2 ligt de focus op de implementatie en voorlopige validatie van de DENSE-techniek voor MRI scanners met een veldsterkte van 3T en 7T voor het meten van door het hart geïnduceerde volumetrische rek in het menselijk brein. Het hoofdstuk beschrijft prospectief getriggerde metingen van de verplaatsingsvelden van het hersenweefsel, die de gehele hartcyclus bestrijken. In gezonde proefpersonen wordt de volumetrische rek berekend als middel om de microvasculaire functie af te leiden, zowel bij 3T als bij 7T. Het hoofdstuk toont de haalbaarheid van DENSE om hersenweefselpulsaties nauwkeurig te meten bij hoge veldsterktes, maar bevestigt ook de noodzaak van een hoge signaal-ruisverhouding (SNR) om de volumetrische rek van het hersenweefsel betrouwbaar te meten. Daarnaast laat het hoofdstuk zien dat verschillen in volumetrische rek tussen verschillende weefsel types gemeten kan worden met DENSE, en dat dit potentie heeft voor het bestuderen van bloedvolumepulsaties in de hersenen in verschillende condities (gezond, verouderend, en ziek).

In Hoofdstuk 3 wordt de DENSE-techniek verder ontwikkeld door een *retrospectively-gated* methode te introduceren, die twee keer zo snelle is, en een verbeterde SNR oplevert. Dit hoofdstuk onderzoekt de intracraniale volumedynamiek en meet de cerebrale volumetrische rek bij gezonde proefpersonen. Het hoofdstuk laat zien dat de gemeten piekvolumetrische rek tussen scansessies heel vergelijkbaar is, en dat er significante verschillen kunnen worden gevonden in de maximale volumetrische rek in grijze en witte stof. Het in dit hoofdstuk beschreven werk valideert de techniek verder met gepaarde metingen van CSF-flow op C2-C3 cervicaal niveau, in overeenstemming met de Monro-Kellie-doctrine, die stelt dat elke toename van hersenweefselvolume moet worden gecompenseerd door een vergelijkbare afname van de volumes van het intracraniale vloeistofcompartiment. Het hoofdstuk bevestigt het nut van DENSE voor het onderzoeken van cerebrale microvasculaire pulsaties en het bestuderen van intracraniale volumedynamiek.

De technieken en ervaringen die zijn opgedaan in de hoofdstukken 2 en 3 bieden een solide raamwerk voor het systematisch kwantificeren van hersenweefselpulsaties bij gezonde proefpersonen. Met deze basis begint hoofdstuk 4 aan een verkenning van volumetrische rek bij patiënten met een vernauwing van de halsslagaders, en tekenen van hersenschade die geassocieerd is met cSVD. De door het hart geïnduceerde cerebrale volumetrische rek werd met DENSE gemeten in zowel patiënten- als controlegroepen. De resultaten lieten significant andere volumetrische rekpatronen zien in de patiënten, wat voorlopig bewijs levert dat volumetrische rek een nuttig hulpmiddel kan zijn bij het identificeren en monitoren van

microvasculaire disfunctie bij cSVD-patiënten. De bevindingen komen overeen met de hypothese dat hersenschade kan worden veroorzaakt door vaatwandverstijving. Hiermee wordt het potentieel aangetoond van volumetrische rekmetingen als een hulpmiddel om veranderingen in de microvasculatuur van de hersenen ten gevolge van veroudering of ziekte te bestuderen.

Ondanks het aangetoonde nut van DENSE, erkent hoofdstuk 5 de uitdagingen die inherent zijn aan het implementeren, testen en valideren van een nieuwe techniek, die de klinische bruikbaarheid ervan kunnen beperken. Daarom onderzoekt dit hoofdstuk *Amplified Magnetic Resonance Imaging (aMRI)*, een nabewerkingstechniek om kleine bewegingen in video's te versterken, als een alternatief hulpmiddel om de microvasculatuur te bestuderen. Het doel was om te evalueren of aMRI zou kunnen dienen als een meer klinisch toegankelijk hulpmiddel voor het kwantificeren van hersenweefselpulsaties. Op basis van gefilterde DENSE 7T MRI metingen werd een gouden standaard voor de beweging van hersenweefsel gemaakt, die vervolgens werd toegepast op een statisch sagittaal anatomisch MRI beeld, resulterend in een zogeheten DENSE-geanimeerde MRI-serie. aMRI werd vervolgens op deze reeks toegepast en de versterkte verplaatsingen werden gekwantificeerd met behulp van beeldregistratie en vergeleken met gouden standaard waarden. Daarnaast werd een DENSE-versterkte MRI-serie gemaakt, waarin de gouden standaard beweging versterkt met een factor x werd toegepast op het statische anatomische MRI beeld, wat resulteerde in een zogeheten DENSE-versterkte MRI-serie. Hoewel aMRI-afgeleide verplaatsingen consequent een lagere geschatte amplificatie vertoonden dan DENSE-versterkte MRI-metingen, bleken de ruimtelijke, temporele en gemiddelde kenmerken van hersenweefselbeweging afgeleid van aMRI vergelijkbaar te zijn met de gouden standaard. De conclusie van dit werk is dat verder onderzoek nodig is om te bepalen of aMRI kan dienen als een betrouwbaar hulpmiddel voor het kwantificeren van hersenweefselpulsaties.

In Hoofdstuk 6 wordt een algemene discussie gegeven over hoe DENSE kan worden gebruikt om de microvasculatuur te bestuderen. Het behandelt ook andere MR-technieken die aanvullende informatie kunnen geven voor het bestuderen van de microvasculatuur. Verder wordt de mogelijkheid verkend om volumetrische rekmetingen van hersenweefsel te gebruiken voor het onderzoeken van andere hersenziekten. DENSE is een gevestigde techniek voor toepassing in het hart, maar de toepassing ervan op de microvasculatuur van hersenweefsel is nog nieuw. Daarom eindigt hoofdstuk 6 met een toekomstperspectief op hoe deze techniek, in combinatie met andere verwachte verbeteringen in het veld, indirect zicht op de kleine vaten kan bieden, en hoe dit ons kan helpen om meer inzicht te krijgen in de microvasculaire functiein de hersenen, bij gezondheid, veroudering en ziekte.

Acknowledgements (Dankwoord)

I would like to express my sincere gratitude to the many individuals who have supported me throughout this research journey. The role of my family unit as a whole must first be acknowledged, as the various ways that they have nurtured my growth, both big and small, has certainly contributed to my ongoing success.

To my beloved **mother** who has always been my greatest fan and advocate, I offer my heartfelt thanks. You taught me kindness, patience and perseverance since I was a young child sitting on your knee. Those lessons allowed me to blossom into a compassionate, resilient and successful person, capable of facing adversity with grace and determination. Despite the oceans that separate us, your unconditional maternal love has always been a constant source of comfort and strength. You have rejoiced in my triumphs, encouraged me through my struggles, and reminded me often that I am loved and valued. Your steadfast belief in me has given me the courage to chase my dreams, and for that, I am eternally grateful. Thank you for being my rock and my guiding light.

To my **father,** I know that all of your paternal advice over the years came from a place of deep care and pride in my achievements. Though often unsolicited, your counsel provided me with self-reliance and steady footing when navigating life far from home. Thank you for the support and encouragement to take this leap. I am grateful for the numerous sacrifices you and Mom have made for me throughout the years.

Dele and **Adjaye**, you guys are more than just siblings; you are the architects of my character. It was within the playground of our shared childhood that I learned to balance diligence with a spark of humor.

To my extended family in the US, UK, and SVG - **Auntie Sonia**, you have played the role of a second mother seamlessly, illuminating the meaning of familial support. Your quiet hopes for another doctor in the family didn't go unnoticed, and although I veered down a different path, your influence remains imprinted on my journey. **Aunt Cheryl**, **Uncles Edwin**, **Errol** and **Marcus** - spending time with you has shown me the importance of finding joy in life's little moments, regardless of age. **Auntie Pat**, you sparked a sense of curiosity and wonder from a young age by gifting me book after book.

Kim, **Kareem** and **Keith/Terrie**, your infectious enthusiasm and zest for living, laughing, and celebrating each other has often reminded me to keep pressing forward with a smile. **Fabian**, you helped me find my place and establish my footing on my eventual return to the UK. You have my sincere thanks for helping me transition from a shy, naive kid to the boffin

I am today. **Juliette**, I appreciated the periodic check-ins along the way - throughout this journey I was certainly tempted to follow your example and pursue a career in finance!

Uncles Godric, **Earl** and **Wendell**, thank you for your many words of encouragement and reminders to stay grounded to the positive vibrations, peace and serenity of the island life. **Auntie Luvene**, you always inquired about my progress and well-being, thank you for showing genuine interest and care for me. I know that you are very happy for me to have accomplished this milestone.

Aunty Brenda, **Aunty Wendy**, **Auntie Una**, **Uncle Jerry** - gone but not forgotten - I wish you were here to see this achievement. You have been a part of my life in different ways, and you have all left a lasting impression on me.

To all the other cousins and members of the extensive family tree - the **Nicholls'**, **Searle's**, **Reeder's**, **Lawrence's**, **Browne's** and the list goes on - you have my gratitude for instilling the values, discipline and resilience necessary to endure this challenging journey.

The important role played by my supervisors in this achievement cannot be overstated. **Jaco**, I am deeply grateful that you recognized my potential as an academic. Thank you for providing invaluable mentorship throughout my PhD journey. Your many Dutch proverbs lightened the mood and provided local wisdoms that helped to reframe obstacles. Your willingness to entertain my sometimes wild research ideas gave me courage to pursue my academic aspirations. You challenged me to grow as an independent researcher, patiently shaping my chaotic concepts into coherent projects. The countless hours you devoted to consultation and discussion, ever willing to provide iterations on manuscripts and make yourself available, mean more than I can express. I am sincerely grateful for your mentoring despite the infinite competing demands on your time. I feel privileged to have learned under your guidance. **Max** and **Peter**, your timely and discerning feedback on my manuscripts and thesis was critical in refining the content and clarity of my work. Your experienced perspectives provided invaluable theoretical and practical grounding for my analyses. I sincerely appreciate the time you both took to provide thoughtful critiques and reviews. Your feedback strengthened the methodological approach, enriched the analysis, and improved the clarity and quality of my results and discussion. This thesis would not be what it is without your skilled inputs and commitments.

Some amazing people brightened this journey with their presence. They were not just passing strangers: they are my friends and I am truly honored to name them that. **Cyril**, your friendship is a treasured gift that will stay with me forever. Thank you for the chill drinks throughout the city, and for being my eyes on so many entertaining nights out over the years (cassage de nuque!). I'm grateful you indulged my cheesy French pop music fixations, and that I got to see my favorite artists play live so many times together - it was a special blast to

see them perform on that Marseille rooftop. Our adventures have taken us on voyages across the Netherlands, France, Bali, Singapore, Hawaii and hopefully many more to come. I appreciate you welcoming me into your life in Marseille, letting me experience the captivating highlights of your charming hometown. The breathtaking Calanques, and the view while clinging in terror to the climbing walls will be lifelong memories. I hope to someday return the favor by showing you the beauty of my home islands. Thank you for routinely pushing me to find my inner super saiyan, by completing this thesis it feels like I've finally joined you in achieving it.

Isabell, your lively energy and radiant smile never failed to lift my spirits. I always left our time together with sore cheeks caused by all the laughter. Some of your dance moves at the Stathe are still permanently burnt into my mind! Our festival camping trip remains one of my treasured memories, those moments of happiness with wonderful friends like you were a refreshing pause during the long journey. Moreover, the resilience and perseverance that you demonstrated as you followed your dreams motivated me immensely. I am overjoyed to see you enjoying the fruits of your labour that you worked hard for and truly deserve. Your positive spirit and supportive attitude naturally draw people to you; I am grateful to be among those you welcomed and chose to share both bright and dark moments with over the years.

Suzanne, your unwavering kindness and care has touched me profoundly. All the heartwarming home cooked meals and cozy hospitality that you provided made me feel super welcomed. Also, my first terrifying yet exhilarating tandem biking experience was all thanks to you! The opportunity to see you achieve so many of your major life milestones is something I deeply cherish - from completing your PhD after years of diligent work, to committing yourself to your life partner in a wedding filled with love, to embracing parenthood with your beautiful baby Liz, and finally obtaining the new home where your family will flourish. I look forward to seeing your family continue to grow and hit more milestones together.

Kristen, my dear long-time friend, we've shared so much over the years - countless conversations exploring life's richness, new adventures discovered together, ups and downs witnessed side-by-side. From fun trips to fabulous festivals, nights out to dinners in, you've made this long journey not just bearable but profoundly enjoyable. I can't begin to thank you enough for all the wonderful moments we've spent together. You've had my back every step of the way. I'm also grateful to you for introducing me to so many other lovely people, like **Vera**, **Ingeborg**, **Lieke**, and more whose names slip my mind but whose smiles and times we shared will stay in my heart. Though I cannot express it all here in brief, know that you are deeply treasured. **Martijn**, I rest easier knowing that my buddy Kristen has you as a copilot. Thank you for being her unwavering pillar of support, fountain of wisdom, and trusted explorer of inner truths.

Lan, I simply cannot envision my life here without you in it. Thank you for broadening my previously narrow perspectives on so many domains of life. Growing up on a tiny island has sheltered me from much so I am truly grateful for all the possibilities you showed me. Your willingness to listen to my concerns and offer sage advice has been invaluable, I always felt safe talking to you about anything. You have given me so very much, but the greatest gift has been your treasured friendship. **Mathijs**, our time together has led to profound self-discovery and growth. Seeing aspects of myself reflected in you has taught me a great deal. Thank you so much for all the times you reached out, and all our gatherings that you initiated. I was and still am always happy to see you. Your generosity and kind words are so appreciated and really helped with my confidence. You and Lan are both truly wonderful people. I am sincerely glad we were brought together and for the opportunity to learn from such a phenomenal couple.

Vineet, our late-night high-level tête-à-têtes traversing the mysteries of existence—from the minute atoms to massive galaxies—were truly educational, engaging and entertaining. Despite our divergent upbringings, it's remarkable how parallel our journeys have been, leading us to this shared moment. You often lent an ear as I shared my perspectives on the absurdity of life and patterns of human behaviour (particularly during the pandemic). I'm especially grateful for our discussions wrestling with the imposing familial expectations on us as emigrants and the challenges of adapting to unfamiliar cultural settings.

To my dear friends in the ‘Asn persuasion’ group: **Nga**, **Shannon**, **Laura**, and **Vivien** - you made the difficult COVID days not just bearable, but filled with treasured memories. Our magical late nights brimming with terrible karaoke, deep heart-to-hearts, and side-splitting laughs (I'll never forget our Key & Peele marathons) created bonds beyond measure. Nga and Shannon - thank you for welcoming me into the glamorous VIP Amsterdam lifestyle. Nga, not many people are as lucky as I to find and experience the world’s best neighbour. Your audacious, adventurous spirit was a marvel to see at so many unforgettable boat and house parties. Thank you for all the great music that you shared, listening to them would always take me back to the great moments we spent together. Shannon, thank you for showing me that sometimes beauty comes in hilariously strange packages. Your slower pace brought much-needed balance and harmony to our group. Our endless debates searching for that elusive film we both enjoy may someday come to an end. Laura, thank you for the journey we took together, and for leaving many footprints of kindness wherever you walked. You offered so many nuggets of wisdom revealing where happiness could be found. I learnt so much from you; Ich bereue es nicht - I hope we can always laugh together about that. And Vivien, my radiant warrior princess, few connections in this world make me feel as profoundly understood as the one we share. Though oceans may separate us now, our souls remain forever intertwined. Your rare gift of making me feel wholly accepted is one I'll forever treasure. Through our many conversations I have come to learn that your mind is truly an exquisite masterpiece - I will forever be impressed by how you link concepts and

bridge ideas. Thank you for sharing *everything*, caring for me *everywhere*, and being such an accepting person *all at once*. I want us to be friends in every version of the universe.

Inge, I am profoundly grateful for your efforts in guiding me down a path of vulnerability. Beyond that, our shared connection has been invaluable to me. We both wrestle with having dazzling minds that sometimes go into overdrive, a beautiful rose with many thorns. Your experience and shared perspectives have shown me that there is a way of living in harmony with this restless tendency. I sincerely thank you for all the mindset shifts that you have imparted to me.

The rigors of a PhD program can certainly make one feel old before their time! **Fenna**, thank you for your role in keeping me youthful by inviting me into your world. Even though life handed you so many terrible lemons, your kind, forgiving nature never changed, and you continued to blossom and forge ahead with a smile in spite of the obstacles. Your strength of character is truly admirable and I am thankful to have seen it up close.

Amparo, your support during my most challenging year will always be remembered. Thank you for your seemingly endless reserves of patience and understanding as I worked to overcome my difficulties. Our companionship has truly enriched my life. I'm really happy for the moments where we could walk side by side, learning from each other as we basked in the warmth of the sun, even as we watched the shadows stretch out from the approaching sunset.

Ana, you have been an incredible source of inspiration and support throughout my journey. I wish so much that I could mirror the relentless energy you possessed even on the days where you had little sleep. I will never forget the macumba parties we attended together, where you patiently put up with my attempts to sing reggaeton songs, despite me not knowing any of the words. Your knowledge and passion for the beers and breweries of the Netherlands is so impressive, you really gave me a new understanding and appreciation of this wonderful country. Thank you for being such a wonderful friend and guide, I am certain every one of your many friends feels lucky and blessed to have you in their lives. Given your demanding social and PhD life I am grateful for the moments we could share together.

To my bouldering crew - **Carlo**, **Joao**, **Casper**, **Laura V**, **Elena**, **Luisa**, **Martina** and others: Thank you for the countless nights filled with casual banter as we pushed each other to scale new heights, both literally and figuratively. You welcomed me into the warm bouldering community and showed me the true meaning of "Sterk!". I have really fond memories of our adventures in Fontainebleau, nacho feasts, inhaling camembert and pizza after training. Our friendships have taken me to great heights I never could have reached alone. **Alessia**, I remain sincerely grateful for your help getting established when I first arrived in the Netherlands. I still remember that day you took me to IKEA for my first real furniture - who knew biking

there would be such a treacherous journey! Since then, we have shared many wonderful memories, and I am truly thankful for your friendship. Thank you for being there for me and for making my transition to a new country so much smoother.

To my dear pride babies, **Catherine** and **An**: You guys hold a special place in my heart along this journey. The vibe that we share, whether it's around delicious meals or on the dancefloor, is truly something special. I treasure the memories we've made together and I'm super grateful for the bond that we share. Thank you for being such wonderful friends and for bringing so much happiness into my life.

To my dear friends in Amsterdam - **Lindsey**, **Alison**, **Tony**, **Kim**, **Coen**, **Joelle** (and many others!!) - thank you for the wonderful nights spent in your company where the hours seemed to fly by in a flash. Your humor and positivity brought so much light and laughter into my life when I needed it most. Spending time with you helped clear the clutter in my mind and lift the weight on my heart. The world is undoubtedly a brighter place with each of you in it, and I feel so fortunate our paths crossed. To the Berlin power duo, **Mike** and **Rachel**: Your amazing energy, kindness, encouraging words, and inspiration have truly left their mark on me. I feel so fortunate to have met two of the coolest, most genuine people around. You both exemplify the delicate balance between strength and gentleness that I aspire to cultivate within myself. Thank you for showing me it is possible.

Alex, thank you for taking me under your wing and introducing me to the fun side of PhD life here in Utrecht. From beers to burgers, to beautiful people on bicycles, you showed me how to really experience this vibrant city. I loved patrolling around town together, taking in the sights and sounds. Our adventures sampling brews and bites created such amusing memories.

Quincy, Mr. Handsome Guy! Thank you for the many hours we spent working diligently back-to-back, MATLABing together to get through the grind. I will always remember the fun we had, enduring (and even participating!) in my weird songs, and adding to the fun at the office with your awesome personality, energy, and puns. We must have annoyed the others in the office, but as they say, you can't have great science without rubbing shoulders, right? I still remember the time we carted the bed from IKEA to your house - I'm pretty sure we hold some kind of record as the only people who have ever transported a bed that way! Thank you for sharing your struggles with me. I was glad that you felt comfortable enough to do so, and even more grateful that I could learn from them as I eventually hit the same stumbling blocks later in this journey. To my office mates - **Lennert**, **Edwin**, **Kees** - thanks for putting up with all my eccentricities and creating a supportive environment!

I owe a debt of gratitude to so many others who helped make this PhD journey fun and manageable. **Julia**, **Sandra**, **Lieke**, **Francisco**, **Ellen**, **Alberto**, **Stefano**, **Beatrice**, **Lisa**,

Bruno, **Erwin**, **Arjen**, **Arjan**, **Janot**, **Jolanda**, **Sander**, **Oscar**, **Tine**, **Jeroen**, **Matteo**, **Martijn**, **Tijl**, **Catalina** and everyone else in the Q2 department - thank you for sharing this adventure with me. Though too numerous to name individually, please know that each conversation, word of advice or moments of laughter helped me push through. I could not have done this without such an amazing network of colleagues.

My academic journey thus far has been an unusual adventure, as before completing my PhD I happened to take a detour to pursue a postdoc position. Regarding the latter, **Jan-Jakob**, thank you for welcoming me so warmly into your research group at the NKI and creating such a positive and stimulating work environment. Your trust in my abilities enabled me to gain confidence as an emerging scholar. I am grateful that you always treated me as a valued member of the team and gave me opportunities to develop my academic skills. Your mentorship and encouragement were instrumental in helping me find my voice.

Hedda, thank you for all the days where you were my partner in crime! So many good moments, learning to accept our flawed selves as a base for growth. I am deeply appreciative of you for the many thoughtful words and acts of kindness exchanged. You are a great supportive friend. You and **Theo** were instrumental in helping me find my place at NKI. I'm happy we had so many chances to deepen our connection outside the workplace. Theo, you've taught me well that the fruits are always sweeter. From your epic bike toss and all the other incredible escapades these last four years, you're a legend in my eyes and Amsterdam isn't the same without you. To my other friends at the NKI: **Amber**, **Jeroen**, **Noelle**, **Itske** and **Roel** - our times chilling at the park and borrels were always quite a show! Being with you all was invariably entertaining.

Thyrza, I'm so grateful to have had you as my office mate. Your witty, sarcastic, dry humor kept me on my toes and reminded me not to take life too seriously. Our banter and jokes provided such welcome comedic relief during stressful times. Beyond the laughs, your caring periodic check-ins on my wellbeing meant a lot, thank you.

Barbara, **Ruben**, **Chavelli** - thank you all for humbling me on the dancefloor with your incredible skills. I have so much yet to learn from each of you! To my other friends in the D2 department – **Anneliz**, **Celia**, **Rouke**, **Saskia**, and all the rest: Our shared lunches, borrels after work, and casual coffee chats offered pleasant company during office hours. It was really a treat working alongside you all, I always enjoyed our time together and got many laughs. I look forward to cheering each of you on as you achieve your own PhD milestone, but you are all already champions in my eyes. Thank you for making the workplace more fun and helping the days go by quicker.

To **Annick**, **Jiske**, **Muriel**, and everyone else in our circle: the final steps in creating this book would not have been possible without your support. Thank you for the many hours

spent lending an ear, offering encouragement, and providing thoughtful reminders to nurture my inner garden. Our discussions planted seeds that continue to bloom. I appreciate you welcoming me into this space of safety, reflection and growth.

To my dear friends from home – **Raianna**, **Keisean**, **Javal**, **La'Ron**, **Sizz-L**, **Justine**, **Kamal**: I cannot imagine rising to this level without having you all at my roots. Your impressive drive and intellectual ambitions were infectious, even from a young age. While our island was small, your eyes were always focused on the endless possibilities beyond the horizon. Thank you for turning my sights to bigger dreams as well. I feel incredibly fortunate to have been included in your aspirational circle. You set me on this journey long before I ever left our shores. No matter where our paths lead, I will carry your encouragement and inspiration with me always.

Whether specifically named or unmentioned, I would like to express my gratitude to everyone who has been a part of my journey to this accomplishment. You have all been instrumental in my achievement, and I'm deeply touched by your generosity, wisdom, enthusiasm, and camaraderie. How fortunate I am to have been supported by you all, and to have shared this enjoyable and meaningful adventure with such amazing people. At the same time, I must also acknowledge my own faults and shortcomings as a friend and family member during this process. In my laser focus on this work, my attention often wandered from those closest to me. I was less available than I aspired to be, terrible in my memory, sparse in my communications, and often lacking the energy to be social. Yet even through my faults, I never stopped feeling the outpour of unconditional love, acceptance, and willingness to reconnect from all of you. As I work towards being more present for those I care about, I want to thank each of you from the bottom of my heart for standing by me through this journey and beyond. Your patience and compassion as I struggled to find balance humbles me. I could not have attained this incredible achievement without your unwavering support.

The work was humdrum, it dragged on and on sluggishly, and all of a sudden it developed into an interesting result and was finished. All the beating around suddenly made sense, and I matured in my own eyes.

— Sergei Winogradsky

Biography

Ayodeji Leigh Adams was born in 1990 in Liverpool, UK, but soon relocated to St. Vincent, where he spent his childhood. His fascination with computers and learning was triggered after interacting with a CD-ROM encyclopedia on his first computer in the late 90s. The knowledge contained therein captivated him with its richness and variety, leaving him keen to discover more. He excelled in his studies and earned a local scholarship to pursue a double-major bachelor's degree in Computer Science and Mathematics at the University of the West Indies, Barbados. After finishing his degree, he spent one year lecturing Information Technology at a local community college in St. Vincent. He then decided to apply his programming and mathematical skills to solve clinical problems in the medical field, and enrolled in a Master's degree in Biomedical Engineering at Surrey University, UK. His first major research project involved working with amputees and studying their gait on different terrains using gyroscopes attached to a lower-limb prosthesis. He gained valuable experience and insight into the challenges faced by the physically impaired. After a year of working as a clinical technician at the London South Bank University, he fulfilled his lifelong passion for learning by pursuing a PhD position at the UMCU concerning the 'development of innovative MRI techniques that yield non-invasive markers of small vessel (dys)function in the human brain'. This led to his research on measuring brain tissue motion driven by pulsations of the cerebral microvasculature, which is described in this thesis. Since leaving the UMCU, he has been working as a post-doctoral researcher at the NKI, where his research goals are primarily linked to finding clinical solutions to managing motion during MR-guided radiotherapy of the liver.

His current interests lie in advancing artificial intelligence research to create powerful and safe tools that can be applied to diverse fields such as education, psychology, medical and basic research. He believes that artificial and human intelligence can complement and improve each other, narrowing the gap between the physical and digital worlds. In his spare time he also enjoys challenging himself with bouldering and running activities.

List of publications and presentations

Peer-reviewed publications

Adams, A. L., Kuijf, H. J., Viergever, M. A., Luijten, P. R., & Zwanenburg, J. J. M. (*2019*). *Quantifying cardiac-induced brain tissue expansion using DENSE*. NMR Biomed, *32*, e4050.

Adams, A. L., Viergever, M. A., Luijten, P. R., & Zwanenburg, J. J. M. (*2020*). *Validating faster DENSE measurements of cardiac-induced brain tissue expansion as a potential tool for investigating cerebral microvascular pulsations*. Neuroimage, *208*, 116466.

Submitted manuscript

Adams, A. L., Terem, I., Champagne, A., Holdsworth, S. J., & Zwanenburg, J. J. M. (*2023*). *Quantitative comparison between aMRI and DENSE for the assessment of brain tissue motion*. bioRxiv, 2023.01.24.525340.

In preparation

Adams, A. L., Rots, M., de Borst, G. J., & Zwanenburg, J. J. M. (*2023*). *Measurements of Cardiac-Induced Brain Tissue Pulsations in Patients with White Matter Lesions*.

Conference proceedings

Adams, A. L., Terem, I., Champagne, A. A., Holdsworth, S. J., & Zwanenburg, J. J. M. (2020). *Comparing aMRI to DENSE for the assessment of brain tissue motion*.

Digital Poster presented at the ISMRM 28th Annual Meeting, Virtual.

Traditional Poster presented at the ISMRM Benelux 12th Annual Meeting, Arnhem, Netherlands.

Adams, A. L., Sloots, J.-J., Luijten, P. R., & Zwanenburg, J. J. M. (2018). *SNR analysis of retrospectively gated DENSE at 7T for the measurement of brain tissue pulsatility*.

Traditional Poster presented at the ISMRM 26th Annual Meeting, Paris, France.

Adams, A. L., Sloots, J.-J., Luijten, P. R., & Zwanenburg, J. J. M. (2018). *Repeatability of measuring pulsatile brain tissue motion and volumetric strain with retrospectively-gated DENSE at 7T*.

Oral Power Pitch presented at the ISMRM 26th Annual Meeting, Paris, France. **Magna Cum Laude Merit Award**

Oral Presentation at the ISMRM Benelux 10th Annual Meeting, Antwerp, Belgium.

Sloots, J. J., **Adams, A. L.**, Luijten, P. R., Biessels, G. J., & Zwanenburg, J. J. M. (2018). *Unraveling Cardiac and Respiratory Contributions to Brain Tissue Motion using Single Shot 2D DENSE at 7T MRI*.

Oral Presentation at the ISMRM 26th Annual Meeting, Paris, France.

Adams, A. L., Luijten, P. R., & Zwanenburg, J. J. M. (2017). *Measurements of cardiac related pulsatile volumetric strain in grey and white matter brain tissue with high-resolution DENSE at 7T*.

Oral Presentation at the ISMRM Benelux 9th Annual Meeting, Tilburg, Netherlands.

Oral Presentation at the ISMRM 25th Annual Meeting, Hawaii, USA.

Adams, A. L., Luijten, P. R., & Zwanenburg, J. J. M. (2016). *Brain tissue pulsatility measured at 7T with high resolution and whole brain coverage*.

E-Poster presented at the ISMRM 24th Annual Meeting, Singapore.

Oral Presentation at the ISMRM Benelux 8th Annual Meeting, Eindhoven, Netherlands.